Quantum dynamics of heavy-ion collisions at Coulomb energies using the time-dependent coupled-channel wave-packet method

Terence Vockerodt
University Registration No.: 6264273
Thesis submitted for the degree of doctor of philosophy

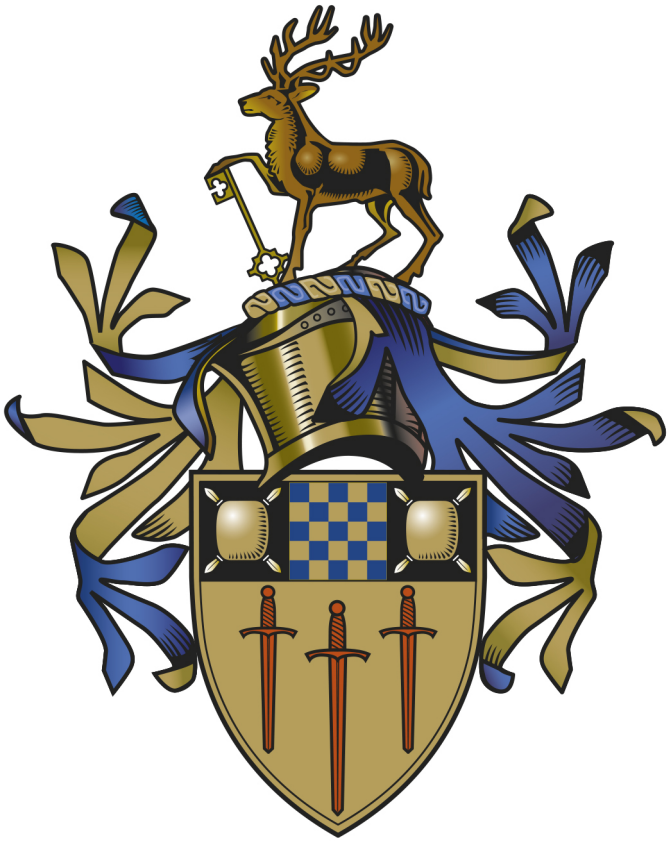

Supervisors:

Dr Alexis Diaz-Torres
Dr Arnau Rios Huguet
Department of Physics, University of Surrey

February 25th 2021

Declaration of originality

This thesis and the work to which it refers are the results of my own efforts. Any ideas, data, images or text resulting from the work of others (whether published or unpublished) are fully identified as such within the work and attributed to their originator in the text, bibliography or in footnotes. This thesis has not been submitted in whole or in part for any other academic degree or professional qualification. I agree that the University has the right to submit my work to the plagiarism detection service TurnitinUK for originality checks. Whether or not drafts have been so-assessed, the University reserves the right to require an electronic version of the final document (as submitted) for assessment as above.

Acknowledgements

If I were given the chance, I would write another thesis that sings the praise of all the various people that have helped me along the way, but in the interests of time I will simply provide commentary on some of the most important people that helped.

Firstly, I would like to thank my main supervisor Dr Alexis Diaz-Torres for his contributions and advice. Alexis was able to tactically leverage my experience with coding and mathematics in order to push me to achieve a relatively early publication, whilst also educating me on the detailed lore of the nuclear physics world to supplement my learning. Whilst the first few drafts of this thesis looked more like a computational or mathematical physics thesis, through Alexis' help it looks much more like a work that pays homage to the exciting legacy of nuclear physics.

The next praise belongs to the administrative/support team for the department of physics. In particular, without the administrative work of people like Joanna Moore, Natasha Ney and Natasha Partt, the research would probably not be possible. Also, Kay Pearson has provided a monumental amount of support through her organisation and advertising of careers workshops. She has helped me to broaden my skill set, as well as given me a clearer vision of where I want to be in the future.

To my family, who supported me during the scariest of times and enabled me to have a quick recovery to what could have been a major setback to my life and livelihood. I will keep caring about my mental health with the vigilance you have demonstrated to protect it. And finally, I would like to acknowledge Sophia Laura Sahara Harberd, for being an incredible friend and supporter. I cherish you and the time we have spent together when I needed a friend the most. I can only hope that I have had as much of a positive impact on you and your personal development and journey as you have had on mine, and I look forward to many more adventures in the wonderful forests of the world with you.

Abstract

Superheavy elements (SHE) are defined as elements with proton number $Z \geq 104$, and were predicted to exist as early as 1966 using the nuclear shell model. One of the most effective experimental techniques for producing SHE is via the cold fusion of heavy ions. Currently, there is no fully quantum mechanical description that addresses scattering and fusion phenomena involved in the formation of SHE in the cold and hot fusion scenarios. From our literature review, we have determined that a few body quantum dynamical method is a sensible approach to describing collisions that lead to the formation of SHE, in particular for the ability of these methods to incorporate dynamical effects, such as nuclear friction, and quantum effects such as tunnelling.

Our goal is to develop a quantum dynamical method that includes quantum tunnelling, and can be expanded upon in the future to describe nuclear friction and multi-nucleon transfer phenomena. In order to build and test our dynamical model, we model a simpler nuclear collision which will allow us to properly explore the strengths and weaknesses of our approach. In this feasibility study, we benchmark the time-dependent coupled-channel wave-packet (TDCCWP) method results for ^{16}O + ^{152,154}Sm collisions, to those from solving the time-independent Schrödinger equation (TISE) using the iso-centrifugal approximation. Comparisons to experimental data are also present. We generate the transmission coefficients, S-matrix elements, inelastic transition probabilities and differential cross sections for the elastic 0^+, and inelastic 2^+ and 4^+ states in the ground state rotational band of the ^{152,154}Sm targets.

We find that the TDCCWP results reproduce the TISE results for a wide range of energies (including many below the Coulomb barrier) and angular momenta. However, the TDCCWP method has technical limitations when trying to explain results deep (> 5 MeV) below barrier, and results at high angular momenta, which are needed to describe the scattering differential cross sections. We address the former by using a simple yet justified extrapolation method into deep below barrier energies. For the ^{16}O + ^{152}Sm inelastic scattering differential cross sections at 59 MeV, the nearly converged TDCCWP method results are a significant underestimate of the experimental data, but are qualitatively similar to the TISE results. This can be improved by relaxing the iso-centrifugal approximation. Overall, we find that the TDCCWP method is a robust method that can be expanded upon to address more complicated problems such as SHE formation and heavy-ion collisions in general.

Contents

Chapter 1

Introduction to heavy ion collisions and superheavy element formation

1.1 The prediction of superheavy elements

Superheavy elements (SHE) are defined as elements with proton number $Z \geq 104$, and were predicted to exist using the nuclear shell model as early as 1966 [1,2]. The nuclear shell model successfully explained the concept of 'magic numbers', which are a set of specific numbers of either protons or neutrons. A magic nucleus is a nucleus with a magic number of either protons of neutrons, and these magic nuclei were observed to have enhanced stability compared to neighbouring nuclei [3]. This extra stability is characterised by a higher total binding energy, a higher nucleon separation energy, higher energy for the low lying excited states, and a large number of isotopes or isotones with the same magic number [3]. A doubly magic nucleus has a magic number of both protons and neutrons, and the shell model, using a Woods-Saxon potential well, predicted that there was a doubly magic superheavy nucleus at 114 protons and 184 neutrons [1,2]. Later in 1967, the Strutinsky model for nuclear fission was introduced (see section 1.2 for a definition of nuclear fission), which was able to calculate the fission barrier using shell effects for the first time [1]. The Strutinsky model found that, for several superheavy nuclei (SHN), additional structure in the fission barrier due to shell effects contributed to fission hindrance, which enhanced the stability of the nuclei from spontaneous fission decay [1,3].

With a lot of favourable theoretical evidence for the existence of SHE, experimentalists worldwide began upgrading facilities to begin the hunt for SHE. In order to create SHN, experimentalists perform hot and cold fusion reactions, with heavy targets such as lead, bismuth, and actinide isotopes [1]. Nuclear fusion is a reaction where two nuclei coalesce to form an excited compound nucleus [4]. In nuclear physics, the reaction cross sections are a measure of the cross sectional area of overlap between the two reacting nuclei, which is used in calculating the likelihood of a particular reaction occurring [4]. The higher the cross section is, the more likely

a reaction is to occur. Cross sections are measured in a unit called barns, and 1 barn = 10^{-28} m^2 = 100 fm^2.

Whilst ambitions for discovering new SHE are high, the fusion reaction cross sections are not - they are of the order of picobarns or less [1]. This is due to the large Coulomb repulsion of the target and projectile during fusion. Currently, the optimal reaction parameters needed to maximise the yield of SHN via fusion are not well understood, and it is not likely that a systematic experimental study of optimal reaction parameters for the production of SHE will be feasible in the coming years. By yield of SHN/SHE, we mean the number of desired SHN/SHE produced by the nuclear fusion reaction. This is a perfect opportunity for reaction theory to develop and try to explain the reaction process for the production of SHE. In this chapter, we will explore the current state of nuclear reaction theory, in order to propose a novel method for calculating nuclear reaction observables. Before we look into nuclear reaction theory, we will motivate the problem in a little more detail in both the perspective of theorists and experimentalists.

1.1.1 Why should we study new nuclei and further reaction theory?

Currently, the nature of the nuclear force is not concretely understood for all nuclei. Whilst current models reasonably explain nuclei close to the stability line, the further from stability one goes the worse the understanding is [5]. This means that the production and subsequent studying of SHE can provide new inputs into models and increase our understanding of the nuclear force and other nuclear physics phenomena. For example, the rapid neutron capture process (r-process) path in astrophysical sites lacks understanding, so much that the natural origin of elements from iron to uranium is one of the eleven greatest unanswered questions in physics today [5]. Moving onto the frontiers of modern chemistry, currently we do not know what is the heaviest possible element to exist, nor its chemical or physical properties [6].

To investigate these problems, we require a consistent production of SHE. This is why we are motivated to provide a powerful reaction theory, that is able to provide experimentalists with optimal reaction parameters necessary to increase the yield of SHE produced in reactions. The reaction theory can also provide great theoretical insight into the production of SHE that cannot be performed in the lab, such as in the astrophysical r-process, which can only be performed in 'catastrophic astrophysical events' [7]. In this situation, the use of theory is mandatory, from which the r-process abundances of nuclei can be generated and compared to real world astrophysical observational data. Nuclear reaction theory provides the rates of reactions that contribute to the formation of the r-process elements, which can be integrated over to find the abundance of a particular element.

1.1.2 The discovery of nihonium and the practical uses for applying theory to experiments

So far, we have discussed the numerous benefits that the production and study of SHE have to nuclear, chemical and astrophysical theory. I want to recount the story of the discovery of element 113, a.k.a.: nihonium, and use it to illustrate some of the experimentally practical benefits of having access to accurate theoretical predictions of reactions that produce SHE. The details for this recount below can be found in reference [8].

In September 2003, a group of scientists at RIKEN lead by Kōsuke Morita began searching for the fabled element 113, via the fusion of bismuth and zinc nuclei. Despite the cross section being very low, the team were able to see an event on the 23$^{\text{rd}}$ July 2004, where a fused element 113 decayed via four alpha decays into dubnium-262, which then underwent spontaneous fission. They saw this exact decay again on the 2$^{\text{nd}}$ April 2005, less than a year from the first. However, these events were not deemed to be conclusive evidence for the production of element 113 (according to the Joint Working Party's 2011 report).

Despite this, the team continued, and performed supplementary experiments to improve the characterisation of the decay chains involving dubnium-262, so that they could provide more insight into their previous observations. Following the improved characterisation, if they observed dubnium-262 decay via alpha decay rather than spontaneous fission, then this would decisively demonstrate that the dubnium-262 was produced by element 113. With this goal in mind, the team pressed on with their efforts to observe element 113.

Sadly, the incredible luck involved for their previous two observations had run out. Weeks turned to months, months turned to years, and still the final event had not been observed. It was only until much later, on the 12$^{\text{th}}$ August 2012, that they observed the final event - the alpha decay of dubnium-262. This marks the end of the near decade long hunt for element 113. Morita et al. named the new element nihonium - after the country of Japan (Nihon is Japanese for Japan).

Whilst this discovery is heralded as a great and proud success, it did not come without a price. The abnormal duration of the experiment meant that the GARIS e3 beamtime was monopolised for almost a decade (reference [9] shows that the GARIS e3 beam was solely scheduled for the nihonium experiment from September 2003 to October 2012), which meant that other projects at RIKEN that required that beam could not be scheduled. This means that future projects for SHE can be viewed as very risky and may be less likely to be funded by non-dedicated superheavy facilities, making research of SHE less accessible worldwide. Hypothetically, if one has a reasonably accurate theoretical model that can at least predict the positions of resonances in the cross sections, then the yields of SHE formation can be made more optimal compared to performing the experiment without aid of theory. In nuclear physics, a resonance is an enhancement of the reaction cross section, which occurs at

collision energies that match the energy values of quasi-stationary quantum states of the compound nucleus [4].

The availability of a theoretical model will provide good leverage for grant applications, since there can be some estimation of the timescale of the experiment prior to the experiment being performed. Even in the case where institutions avoid this problem of scheduling conflicts by opening dedicated facilities for research of SHE (such as the SHE factory at JINR in Dubna, Russia [10]), increasing the yield of SHE via the use of accurate theory is still of immense benefit due to providing better statistics for the experiment. A powerful theory is of great practical benefit for those performing experiments, and it can give us a more realistic picture of the expected yield of the production of SHE.

1.2 Background of nuclear collisions and heavy-ion collisions

Now that we have motivated the problem, we will explore the world of nuclear reaction theory in order to find a solution. Consider a nuclear fusion reaction between a projectile and target nucleus with atomic (nucleon) numbers Z_{P} (A_{P}) and Z_{T} (A_{T}) respectively. The fusion process can be described in three steps [11]:

1. Capture: the projectile nucleus A_{P} approaches the target nucleus A_{T}.
2. Formation: the two nuclei react and form a compound nucleus of the set $\{C\}$.
3. Decay: the compound nucleus C cools and decays into nucleus B.

This is expressed with the reaction equation $A_{\mathrm{P}} + A_{\mathrm{T}} \rightarrow C \rightarrow B + \{p, n, \alpha, \gamma\}$, where B are known as evaporation residues, and $\{p, n, \alpha, \gamma\}$ are a set of by-products (proton, neutron, alpha particle and gamma ray respectively) that depend on the formed nucleus B (in principle this set of by-products can contain more elements). The two major decay processes are known as evaporation and fission. Evaporation involves the emission of light particles such as those in the set $\{p, n, \alpha, \gamma\}$, whereas fission involves the splitting of the compound nucleus into roughly two equally sized nuclei known as fission fragments [12].

The primary SHE created by this process are elements of the set of compound nuclei $\{C\}$, which are detected by experimentalists by detecting the decay products of the reaction, that is, B and $\{p, n, \alpha, \gamma\}$. Note that the evaporation residues B might not be stable and can decay further, in fact B can contain secondary SHE which can be detected by their decay. The capture and formation steps of the reaction operate on the timescale of 10^{-21}s (known as the zeptosecond timescale), but the decay phase occurs several orders of magnitude later between $10^{-19} - 10^{-16}$s [12],

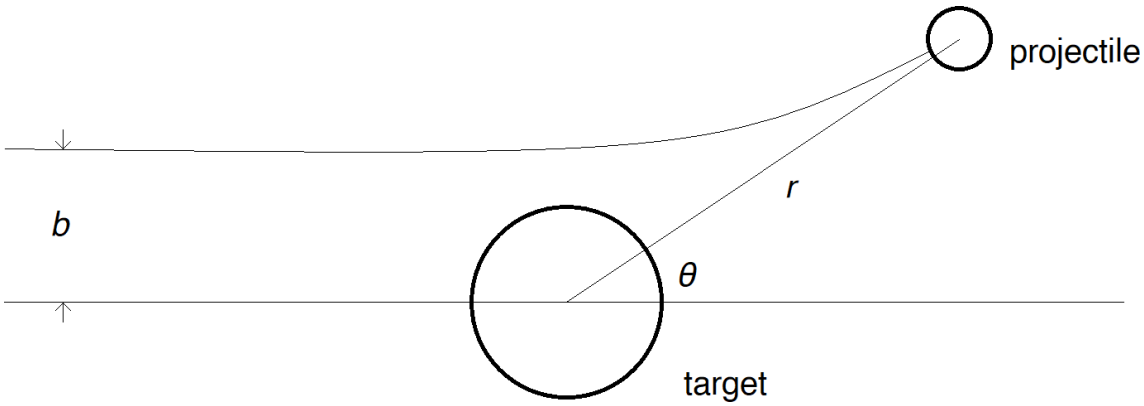

Figure 1.1: Diagram illustrating the basic geometrical definitions in nuclear collisions. Here, r is known as the inter-nuclear distance, θ is the polar/scattering angle, and b is the impact parameter.

which justifies the use of at least two models to model the reaction (one for the capture + formation, another for the decay).

In general, nuclear reactions are involved and complicated processes, that can have vastly differing physical phenomena involved depending on the reaction parameters. One such parameter is known as the impact parameter - which is the extent of grazing between the two nuclei as they collide [12,13], such that the smallest impact parameter indicates a head on collision between the two nuclei. This is shown in Fig. 1.1. For high impact parameters, the two nuclei do not touch and nuclear reactions do not occur. The only force to act at that range is the Coulomb force, which leads to phenomena such as elastic scattering and Coulomb excitation of the internal nuclear states [12–14]. As we decrease the impact parameter, inelastic scattering processes become prevalent [12–14]. Further decreasing of the impact parameter leads to deep inelastic collisions, which are reactions where the projectile and target are mostly unchanged apart from the transfer of a few nucleons, with low outgoing kinetic energies that are transferred to internal excited states of the nuclei, and high angular momentum transfer from the relative motion of the nuclei into internal excited states [12]. Another reaction that occurs at these impact parameters is quasi-fission, which are reactions where large quantities of nucleons are transferred before the two nuclei separate, which forms a distribution of product nuclei similar to the fission process [15]. Quasi-fission is distinct from fusion followed by fission, because the latter occurs on a longer timescale [12] and the former occurs on the zeptosecond timescale [15]. Finally, direct fusion occurs at low impact parameters [12–14]. Direct fusion, deep inelastic collisions, and quasi-fission involve the transfer of nucleons, and thus are the main mechanisms that contribute to or compete with the compound nucleus formation process that we describe above.

The capture stage involves surmounting the Coulomb barrier, which is a barrier generated from the addition of the repulsive Coulomb potential and the attractive nuclear potential. In the work by V. I. Zagrebaev *et al.* [11], it is demonstrated that the capture process that we have described above is well understood, with excel-

lent agreement between the calculated and the experimental capture cross sections. The experimental capture cross sections are determined by counting all the products produced in the decay stage (the fissile material and evaporation residues) that differ from the starting nuclei [11, 12]. However, the authors mention that the disagreement in the total cross sections (which involve the combination of the capture, formation and decay processes described above) are in part due to the lack of a complete quantitative model to describe the formation of the compound nucleus. They mention that the state of the art models to determine compound nucleus formation cross sections assume a single, dominant mechanism, when it is possible that more than one of these mechanisms can be active at the same time.

1.3 Compound nucleus formation mechanisms

This section is a dedicated literature review on the mechanisms and phenomena associated with the formation of the compound nucleus. These mechanisms act as a checklist that will help motivate the kinds of models and techniques that we need to consider when modelling the formation of SHE.

1.3.1 Macroscopic dynamical models and the di-nuclear system

There are two main mechanisms that have been proposed for the compound nucleus formation. The first mechanism assumes that fusion occurs along the radial coordinate of the collective motion, due to the resulting liquid drop shape of the two nuclei after the initial impact [16, 17]. Typical attempts at this mechanism include a liquid drop model to describe the overall shape of the nuclei, as well as corrections due to the nuclear structure [16, 17]. These models assume that the evolution of the neck of the liquid drop is the driving factor for fusion to occur, and no nucleons are transferred from one nucleus to another (in fact, the models assume there is no way to discern the two nuclear identities that started the reaction, i.e.: there are no nuclei A_{P} or A_{T}, but they are combined into one structure) [16, 17]. These models are known as the macroscopic dynamical models (MDM).

The second mechanism involves the nuclei in a touching configuration, where only the transfer of nucleons between one nucleus and another drives the dynamics of the system [16, 17]. For two nucleons in a dynamical fusion reaction with mass numbers $A_{\mathrm{P}}(t)$ and $A_{\mathrm{T}}(t)$ respectively, where t is time, the mass asymmetry is given by $\eta(t) = (A_{\mathrm{P}}(t) - A_{\mathrm{T}}(t))/A$, where $A = A_{\mathrm{P}}(t) + A_{\mathrm{T}}(t)$ is the total number of nucleons in the system and is constant throughout the reaction [16, 17]. $\eta = 0$ denotes the symmetric configuration ($A_{\mathrm{P}}(t) = A_{\mathrm{T}}(t)$), and $\eta = \pm 1$ are the completely fused scenarios where one nucleus completely engulfs the other. In this picture, the discrete values of η are used as a collective coordinate for fusion, without any substantial change in elongation [16, 17]. These models are known as the di-nuclear system

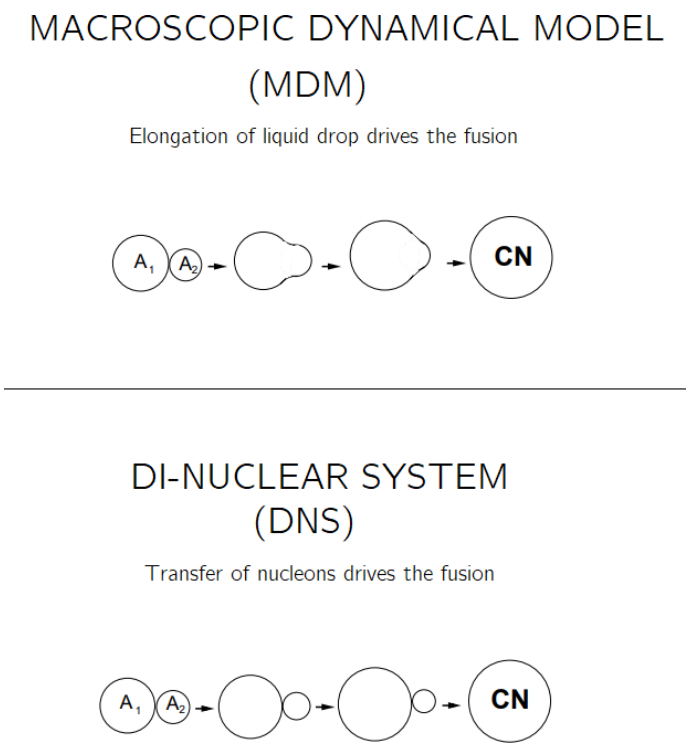

Figure 1.2: Schematic showing and summarising the MDM and DNS mechanisms. Adapted from [18]

(DNS) models. The two different mechanisms are shown schematically in Figure 1.2. The evolution along the elongation and mass asymmetry coordinates are used to represent the physical phenomena of multi-nucleon transfer (such as direct fusion, deep inelastic collisions and quasi-fission [5]).

1.3.2 Effectiveness of MDM and DNS

There have been several studies that have been conducted to investigate the relative contributions of these two mechanisms. For example, in a study by G. G. Adamian *et al.* [16], they compared a MDM using time dependent potentials to experimental results, in order to determine if this mechanism was significant. They used an adiabatic potential, composed of a liquid drop potential with corrections to the shell and pairing energy of the nucleons from the two-center shell model (TCSM). The TCSM is used in the context of the famed Strutinsky macroscopic-microscopic method that we discussed earlier, and can better account for nuclear shapes in fission and fusion reactions [3].

They carried out calculations for several collisions, including ^{100}Mo + ^{100}Mo, ^{100}Mo + ^{110}Pd, and ^{110}Pd + ^{110}Pd. The calculated compound nucleus formation cross sections/probabilities were an overestimate of the experimental results by several orders of magnitude, which led to the conclusion that the description of fusion by elongation using an adiabatic potential was incorrect. They also noted that this

Reaction	$\mathbb{P}_{\lambda}^{(1)}$	$\mathbb{P}_{\lambda}^{(2)}$	$\mathbb{P}_{\eta}$	$\mathbb{P}_{\text{exp}}$
$^{90}\text{Zr} + ^{90}\text{Zr} \rightarrow {}^{180}\text{Hg}$	$2{\cdot}10^{-4}$	$2{\cdot}10^{-2}$	$2{\cdot}10^{-1}$	10^{-1}
$^{100}\text{Mo} + ^{100}\text{Mo} \rightarrow {}^{200}\text{Po}$	$9{\cdot}10^{-6}$	$3{\cdot}10^{-3}$	$2{\cdot}10^{-2}$	$5{\cdot}10^{-2}$
$^{110}\text{Pd} + ^{110}\text{Pd} \rightarrow {}^{220}\text{U}$	$7{\cdot}10^{-15}$	$4{\cdot}10^{-7}$	$3{\cdot}10^{-4}$	10^{-4}
$^{76}\text{Ge} + ^{170}\text{Er} \rightarrow {}^{246}\text{Fm}$	$9{\cdot}10^{-22}$	$3{\cdot}10^{-12}$	$6{\cdot}10^{-4}$	$8{\cdot}10^{-4}$
$^{86}\text{Kr} + ^{160}\text{Gd} \rightarrow {}^{246}\text{Fm}$	$4{\cdot}10^{-26}$	$2{\cdot}10^{-16}$	$7{\cdot}10^{-5}$	$5{\cdot}10^{-5}$

Table 1.1: Comparison of compound nucleus formation probabilities of an MDM and DNS model. λ-channel represents the elongation/MDM channel, where the asymmetry parameter is constant, and η channel represents the asymmetry/DNS channel, where the elongation parameter is constant. (1) and (2) denote calculations using two different parameters. See section 1.5.1 for information on the definition of channels. Adapted from [17]

adiabatic description had a lot of inertia in the necking parameter, as it did not deviate significantly from the initial parameter across the duration of the reaction. This inertia is due to the crossing of single particle levels (the energy levels for different particles become equal), which leads to large microscopical mass parameters which hinder development of the neck [16]. This means that the neck length could be assumed to be constant, like in the DNS description.

In order to address the level crossings, they updated the potential with a diabatic term to account for the Pauli exclusion principle [16, 17], which is used to simulate the extent of inertia in the necking parameter. The initially diabatic potential eventually relaxes into an adiabatic one, which in turn relaxes this inertia in the necking parameter. They noted that for higher mass asymmetries the structural forbiddenness in the necking parameter is less, due to smaller Coulomb barriers. This suggests that, in order for elongation to contribute, the reaction must be engaged by the transfer into higher mass asymmetry states, and only then can the elongation parameter vary and contribute to the fusion cross sections (by migrating to lower elongation states, since lower elongation implies the nuclei are closer together). The transition between an initially diabatic elongation potential to an adiabatic one to simulate this scenario was investigated and compared to a DNS model.

They found a strong agreement between the calculated compound nucleus formation probabilities from the DNS description and the experimental results, for a wide variety of systems, recorded in Table 1.1. However, the contribution to the cross sections from the MDM was consistently lower. Specifically for heavier systems, it is lower by up to twenty-one orders of magnitude, suggesting that the contribution due to this effect is small and can be neglected when considering the production of SHE. Whilst other independent studies have attempted to use an MDM to explain the cross sections, none have been unequivocally successful thus far [19–23]. Since the DNS can describe some compound nucleus formation probabilities more accurately than MDM models (i.e: those in Table 1.1), we advise that an implementation of the formation mechanism should include the DNS description at least.

1.4 The role of friction in heavy ion fusion

Another consideration one has to make for fusion is the idea of nuclear friction. Nuclear friction is the dissipation of the incident centre of mass frame kinetic energy between the target and projectile. Experimental evidence shows that whilst the cross sections of heavy ion collisions are high for compound nuclei close to $A = A_{\mathrm{P}} + A_{\mathrm{T}}$, the cross section peaks were shifted down significantly from the incident centre of mass energy [24]. We have already explored the idea of how the impact parameter can drastically affect the phenomena that occur during the reaction, and the same is true for the inter-nuclear distance r. Dissipation of kinetic energy of the centre of mass motion can both enhance and inhibit fusion, which will be explained in detail below.

1.4.1 Fusion hindrance

Fusion hindrance is an idea that originates from the dissipation of the incident collision energy after the Coulomb barrier has been penetrated, which prevents the overcoming of further barriers in the system and thus decreases the amount of material fused [25]. Typical efforts to include dissipation involve solving the Langevin equation - a classical dynamical model [26]. The Langevin equation has been employed in several models, and whilst some models can calculate observables that are close to the experimental results for energies above barriers, they do not accurately predict the sub-barrier values [27]. Classical and semi-classical models generally fail to describe below barrier phenomena, which is often explained more accurately using quantum mechanics. The Langevin equation has been attempted to describe the radial dynamics of systems with mass asymmetries equal to those of the saddle point of the TCSM potential, but the calculated fusion and 1n (single neutron) residue cross sections differ from the experimental data by several orders of magnitude [28]. A similar implementation of a DNS with nuclear deformations and the Langevin equation has been attempted [29]. Whilst some of the cross sections and mass distributions were reasonably close to the experimental data, there is possibility of improvement by using a quantum mechanical model. In particular, the cross sections for the formation of fission fragments were close to the experimental data for several collision energies, but the capture cross sections were not.

Several authors cite a lack of concrete parameters for the systems they are studying as a likely reason for discrepancy [28, 29]. Whilst the classical dynamics may not be a limiting factor in the calculation yet, a quantum dynamical model can model the conversion of kinetic to potential energy without the use of the Langevin (or equivalent) equation, as well as incorporate more accurate dynamical dissipation for when the two nuclei penetrate the Coulomb barrier. In a classical model, any discrepancy can either be due to the classical motion, or due to other errors. A quantum dynamical model can be used to probe these questionable parameters at the very least without this ambiguity.

1.4.2 Fusion absorption

Like fusion hindrance, nuclear fusion itself can also be explained using dissipation. After nuclei collide, if there were absolutely no dissipation of the collective radial motion of the nuclei, then we would expect to see scattered material due to the strongly repulsive Coulomb force at close distances. This excess scattering does not occur in heavy-ion collisions, because the collective radial motion of the nuclei is dissipated into non-elastic processes [12], such as the motion of individual nucleons within the compound nuclear system.

1.5 Current models

We will now explore some of the contemporary models used to describe heavy-ion fusion, and highlight some of their strengths and weaknesses in their ability to describe the formation of SHE. This will be used to structure and reinforce our quantum dynamical approach to the problem.

1.5.1 Time-independent coupled-channels

The time-independent coupled-channels (TICC) method is a few-body method which aims to describe the the extent of excitation of nuclei after the fusion reaction has occurred [30–32]. By a channel, we mean a particular nuclear configuration and a particular set of quantum numbers for the collective system of the target and projectile [12]. The TICC Hamiltonian couples the target and projectile together, allowing one to influence the excitation of the other. For example, with an inert projectile and an excitable target, the projectile excites the target when they approach closely to one another. This excitation can be mediated by both the strong nuclear force and the Coulomb force. The eigenstates of the CC Hamiltonian are found by solving the time-independent Schrödinger equation using asymptotic boundary conditions.

This method is appealing since it is relatively fast at generating results for a small number of excitations and reaction channels. Time-independent calculations forego the time propagation, which computationally is the greatest time-investment of the time-dependent methods. However, it is not suitable for describing all of the dynamical phenomena that we have listed above since time is not explicitly treated. Specifically, TICC can account for absorption phenomena via static absorption potentials, but this is less systematic than using a dissipative method, which requires time dependence.

Crucially, the time-independent methods do not allow one to fully understand the reaction mechanism. This may seem less important for those interested in a final calculation, such as the yield of the fusion reaction, but it is incredibly important for intelligent model selection. For instance, recall when we discussed earlier in section

1.3.2 that the elongation channels were able to contribute to fusion only in high asymmetry configurations. By an elongation channel, we mean a particular nuclear configuration and a particular set of quantum numbers (including elongation) for the collective system of the target and projectile. Using this information, if we find that there are some reactions that can occupy these high asymmetry configurations during the reaction, then we ought to use a model that incorporates elongation channels into the calculation. In this example, we would not be able to select an appropriate model if we did not know the mechanism beforehand. The extra information provided by the time evolution of these intermediate states can also allow us to make more predictions for the system.

1.5.2 Time-dependent Hartree Fock

Time-dependent Hartree Fock (TDHF) models are many-body models, which involve solving the TDHF equation [33,34]. The TDHF equation arises from the Schrödinger equation after restricting the basis to be single Slater determinant states only [33,34]. A Slater determinant is a wave-function that describes a system of many fermions (such as nucleons) that obey the Pauli exclusion principle [35]. Single Slater determinants form the basis of a fermionic system in the many-body picture [35], and therefore any state in general can be formed with a correlation of single Slater determinants. Restricting the basis to single Slater determinants is a necessary assumption, since it is too time consuming to propagate any general state using the time-dependent Schrödinger equation for many systems. There are a wide variety of different many-body interaction potentials that have been implemented and explored within this framework [33].

Being a dynamical model, TDHF has the advantage of being able to incorporate necessary dynamical terms such as friction. The many-body nature of the model allows one to clearly see phenomena such as necking/elongation without having to explicitly incorporate elongation parameters/assumptions in the basis states [33,34], which allows these models to probe the nature of the strong nuclear force as opposed to the nature of the collective motion only. It can also show the mechanism at the level of individual nucleons, which can be used to better understand the nature of the nuclear force.

These reasons make it a very appealing choice for these kinds of problems, except that the restrictions on the basis prevent quantum tunnelling along the internuclear distance r from being incorporated into the calculations [34]. This means that the trajectory along the collective motion is classical, and since some of the formation of SHE is achieved with cold fusion, ultimately this makes TDHF models less suitable than ones that incorporate tunnelling. Whilst the TDHF methods can explain high energy phenomena reasonably well, as energy decreases the results can be extremely model dependent [33]. This model dependency combined with a lack of quantum tunnelling makes these models unsuitable for the task at hand, since it will be very difficult to interpret results without ambiguity.

1.5.3 Time-dependent density matrix

Time propagations of the density matrix are powerful methods that have been used before in nuclear physics [36–38]. These methods involve the time propagation of the density operator $\hat{\rho}(t)$, which is expressed as [39]

$$\hat{\rho}(t) = |\Psi(t)\rangle \langle\Psi(t)|, \tag{1.1}$$

where $|\Psi(t)\rangle$ is the time-dependent state of the system. One can find $\hat{\rho}(t)$ by solving what is known as the quantum master equation. The most basic form of the quantum master equation looks like [39]

$$\frac{\partial\hat{\rho}}{\partial t} = \frac{1}{\mathrm{i}\hbar}[\hat{H}, \hat{\rho}], \tag{1.2}$$

where $[\hat{A}, \hat{B}]$ denotes the commutator of operators $\hat{A}$ and $\hat{B}$, and $\hat{H}$ is the Hamiltonian of the system. In order to include dissipation effects such as fusion hindrance, a second term is often introduced to the right hand side of equation (1.2), which involves a folding over the dissipator/bath degrees of freedom, and, depending on the class of assumption used, it can be an integral over the reaction time.

The strong publication history behind these models for applications of open quantum systems (systems with dissipation and/or fluctuation) makes them very appealing to use for this problem. However, they are very computationally expensive in both the testing stage and in results generation, since they involve the construction and propagation of the density matrix which has dimensions $N \times N$, where N is the dimension of the wave-function. In order to explain all of the nuclear phenomena that we have described before simultaneously, the size of the basis we desire is reasonably large.

There are methods that involve propagating the wave-function of the system only, which can replicate the results generated by these time-dependent density matrix methods. We explore some of these methods in the future work section, since their complexity is beyond the scope of this thesis, but they are of the utmost relevance for including accurate dissipation/fluctuation phenomena.

1.6 Our novel method

From this analysis, in order to model the fusion of heavy ions one ought to use a DNS model, combined with an accurate quantum dynamical method that can account for dissipation phenomena like fusion hindrance and fusion absorption. It must also be able to reproduce phenomena such as Coulomb excitation and elastic

scattering for larger impact parameter collisions, and must be able to facilitate quantum tunnelling.

The aim of this project is to develop a novel quantum dynamical framework that propagates the wave-function over time, which can be structured and built upon to address the problem of heavy-ion fusion and scattering simultaneously. This work will focus on developing a quantum dynamical method that describes two colliding nuclei, and is known as the time-dependent coupled-channel wave-packet (TDCCWP) method. This work will not address DNS/MDM dynamics due to time constraints, but it is definitely possible to achieve as future work by expanding the quantum basis, and including relevant MNT terms in the Hamiltonian. The methodology we will use to achieve the time propagation will be very general, and can be applied to increasingly complicated Hamiltonians in order to describe a richer variety of phenomena. The models studied in this thesis will have applicability to very asymmetric target-projectile reactions, as well as light and medium mass systems, since the multi-nucleon transfer cross sections for these reactions are much lower than the fusion cross sections [5], and thus we can neglect MNT.

All results in this thesis will use the coupled-channels Hamiltonian used in TICC methods, since it has a sufficient depth of complexity to explain some collision systems, and we can benchmark some of our results with those from the time-independent method. Our model will allow us to describe the capture and formation stages of these reactions, and explore phenomena such as elastic and inelastic scattering, Coulomb and nuclear excitation, and fusion; all simultaneously. Currently, there is no fully quantum dynamical model that both describes the capture and formation stages and their observables, making a project in this area novel.

1.6.1 State of the art of dynamical models

We would like to highlight some ways in which our work is different to other bodies of work addressing this problem. Currently, time-dependent methods are being used to determine the absorption cross sections for nuclear collisions. Typically in these approaches, an energy distribution of an initial and final wave-function are calculated using a time-dependent form of the Green's operator. These energy distributions are then used to determine the penetrability of the collision. The time-dependent Green's operator has been evaluated using fourth order Runge-Kutta methods [40–42].

Instead, we use a modified Chebyshev polynomial propagator (see appendix A.4 for details) to propagate the wave-function over time, since we are interested in looking at the dynamics of the wave-function for small times steps in order to better visualise the mechanisms for nuclear fusion. Compared to other finite elements methods such as the generalised Crank-Nicholson method (which is a finite element method similar to Runge-Kutta), the Chebyshev polynomial propagator is more numerically efficient if one wishes to visualise the wave-function over time as we do [43]. This is because

the Chebyshev propagator has lower computation times for time steps lower than the natural time step of the system. Also, for the small time steps where the Chebyshev propagator is efficient, one can approximate the time integral in the propagator for time-dependent Hamiltonians using finite element methods in time.

Whilst visualising the wave-function may seem redundant if one is solely interested in final results, it does open up very exciting possibilities for future endeavours. Currently, nuclear collisions are achieved by merely bombarding the nuclei together in a very brute force way. This is different to other fields of physics that are able to manipulate the quantum state with use of perturbative fields such as a laser field, which can be used to promote the excitation of targeted states one wishes to study. As of writing this thesis, there are facilities that are dedicated to producing zeptosecond laser pulses, that can be implemented to excite nuclei on the zeptosecond timescale which we are modelling [44]. Then, what becomes important is knowing where to aim said laser, and when to fire it. A quantum dynamical method has the advantage of showing the wave-function position over time, which can be used handily to find the optimal position and timing of the laser firing. For example, if one wishes to study a particular excited state, and they find that the wave-function gets trapped at a particular region for a relatively long period of time, then it would be wise to fire the laser at that region for optimal excitation into the targeted state. Laser fields are time-dependent fields and require information about the entire propagation in order to be utilised optimally, which supports the use of time-dependent methods that propagate using short time steps. Rather excitingly, with zeptosecond and attosecond laser pulses one can provide competition to the nuclear decay processes for every stage of the reaction mentioned in section 1.2.

1.7 Thesis structure

Chapter 2 will detail the theory behind the coupled-channels Hamiltonian that we use. Chapters 3 and 4 will explain the window operator method and showcase our published (and some unpublished) results from said method respectively. Chapters 5, 6 and 7 will explain and showcase results in a similar way, but instead for a Green's operator method involved in the calculation of differential cross sections. Chapter 8 will present the conclusions of the work in the thesis, as well as outline future work that can be undertaken. There are three appendices dedicated to extra details and derivations. In particular, appendices A and C detail the numerical quantum mechanical time propagation techniques that we have used, which are very general and can apply to many different Hamiltonians.

Chapter 2

Simple theoretical treatments of radial nuclear dynamics and the coupled-channels Hamiltonian

This chapter will look into the physics behind the treatment of the radial motion of the two colliding nuclei, as well as highlighting some methods to address the nuclear physics phenomena discussed in the previous chapter. Whilst the angular motion is important as well, it is not covered here explicitly since the nuclear potentials are not dependent on angles (or rather, they are assumed to be spherically symmetrical [3]). The details on how the angular states are accounted for in calculations are given in chapter 5 where they are relevant. Then, we derive the Hamiltonian that we use for calculations with our TDCCWP method.

2.1 Nuclear potentials

Some of the key forces involved in the radial dynamics of nuclear collisions are the repulsive Coulomb force (since both nuclei are positively charged) and the strong nuclear force, which is attractive over short distances of a few fermi [3]. The Coulomb potential for the situation where the nuclei are outside of one another is given by the standard form derived from shell theorem, i.e.:

$$U_{\mathrm{C}}(r) = \frac{Z_{\mathrm{P}} Z_{\mathrm{T}} e^2}{4\pi\epsilon_0 r}, \tag{2.1}$$

where r is the radial distance between the target and projectile nuclei, and Z_{P} and Z_{T} are the atomic numbers of the projectile and target respectively. In this work, we do not consider the dynamics of when the two nuclei overlap (which will be explained in more detail below at the end of section 2.1.1). In the case where

the dynamics of overlapped nuclei are important, then one can derive overlapped Coulomb potentials using the double-folding method, which considers the effects of the nuclear charge distributions in an overlapped configuration [45]. The overall effect of the strong nuclear force can be described by the Woods-Saxon potential [3]. The Woods-Saxon potential is a mean field (i.e.: averaged over all of the nucleons) potential, which is historically ubiquitous in the treatment of nuclear scattering problems. This potential has the form

$$U_{\mathrm{N}}(r) = -\frac{V_{\mathrm{WS}}}{1+\exp((r-r_{\mathrm{WS}})/a_{\mathrm{WS}})}, \tag{2.2}$$

where V_{WS} is the strength of the potential, $r_{\mathrm{WS}} = r_{\mathrm{WS0}}(A_{\mathrm{P}}^{1/3} + A_{\mathrm{T}}^{1/3})$ is the range of the Woods-Saxon potential, A_{P} and A_{T} are the nucleon numbers of the projectile and target respectively, r_{WS0} is a constant radius parameter, and a_{WS} is the diffuseness parameter. Both of these forces are active at the same time, and so the total, angular momentum independent interaction potential is given by the sum of these potentials

$$U(r) = U_{\mathrm{C}}(r) + U_{\mathrm{N}}(r). \tag{2.3}$$

The total interaction potential has some characteristic features that are shown in Fig. 2.1. Here, we can see that the total nuclear potential tends to infinity as the inter-nuclear distance r tends to zero, courtesy of the dominant Coulomb potential at these distances. The attractive Woods-Saxon potential deforms this Coulomb potential, leading to the formation of the fusion pocket, which is 'guarded' by what is known as the Coulomb barrier.

Any flux that penetrates the Coulomb barrier will go on to fuse and form the compound nucleus. In other words, when the projectile penetrates the Coulomb barrier, it is extremely unlikely that the two nuclei (in the zeptosecond timescale) will be able to separate back into their original structures by leaving the fusion pocket (this is known as the never-come-back approximation). This is due to a large dissipation of the collective radial motion (which governs how separated the nuclei are), via the transfer of radial kinetic energy to internal energy of the constituent nucleons of the newly formed compound nucleus. This presents a problem - if we use merely a Coulomb and Woods-Saxon potential to describe the collision like in Fig. 2.1, then any flux that penetrates the Coulomb barrier with radial kinetic energy above the barrier will be reflected by the Coulomb potential close to $r = 0$ and out of the pocket. This means that after a long time propagation no fusion would occur. The Woods-Saxon and Coulomb potentials alone cannot account for fusion, but it can be effectively modelled by preventing any flux from inside the fusion pocket from escaping. Fortunately, there are many methods that have been implemented or developed that can address this effect, such as absorption potentials, incoming wave boundary conditions, and dynamical dissipation to name a few.

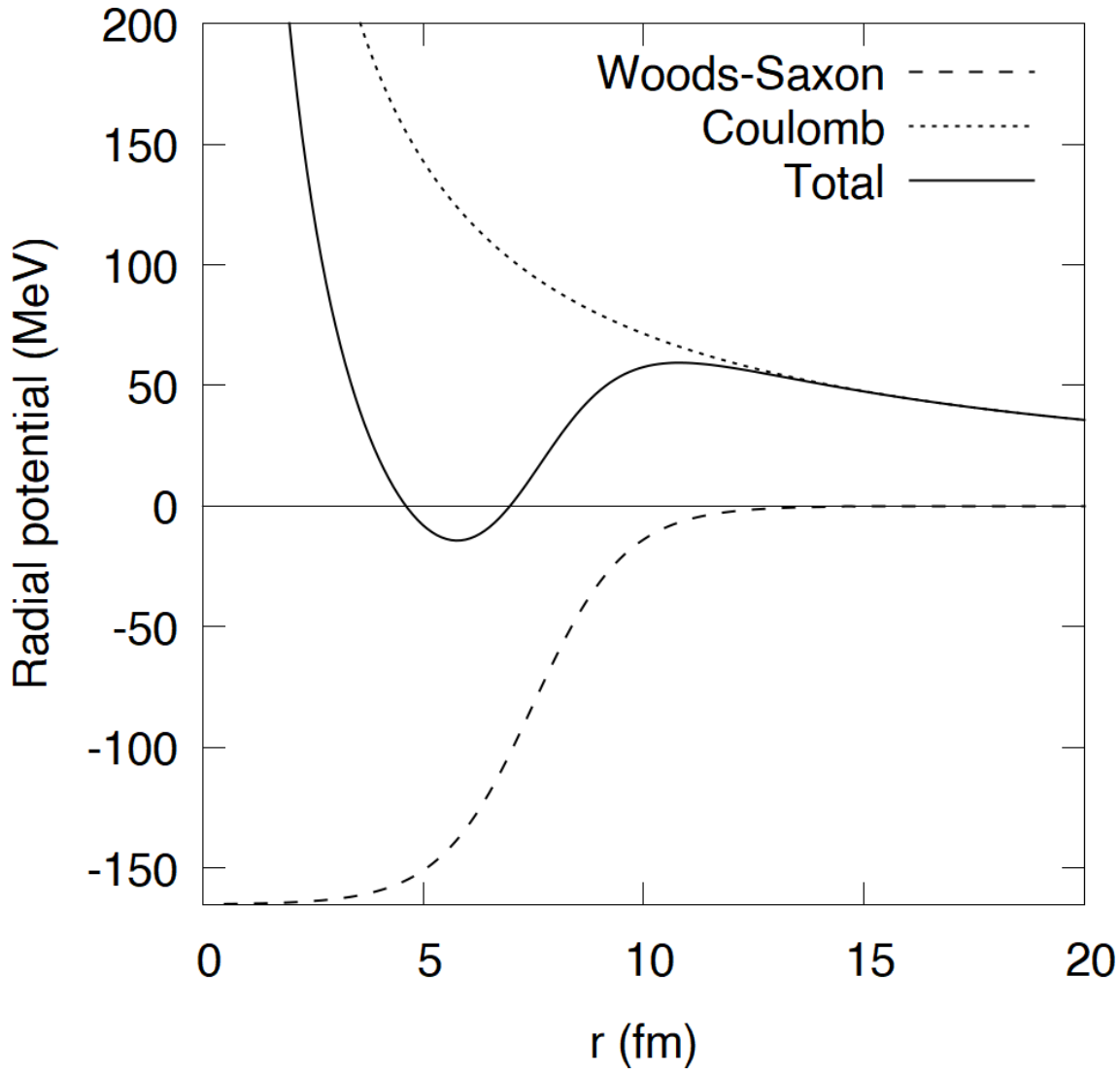

Figure 2.1: Plot showing the radial nuclear potential for the ^{16}O and ^{154}Sm system colliding head-on (orbital angular momentum $L = 0$), as well as its constituent Woods-Saxon and Coulomb potentials. The barrier radius is equal to 10.81 fm, and the barrier height is equal to 59.41 MeV. The fusion pocket is located between $r = 0$ and this barrier radius. The parameters used to generate the Woods-Saxon well are provided in Table 4.2.

2.1.1 Absorption potentials

Absorption potentials are purely imaginary potentials, and are a simple but effective way of introducing absorption into a system. Consider a one dimensional system with Hamiltonian $\hat{H} = \hat{H}_0 + \mathrm{i}\hat{W}$, where $\hat{H}_0 = \hat{K} + \hat{V}$ and $\langle r|\, \hat{W}\, |r\rangle = W(r)$ where $W(r) \in \mathbb{R}$. After rearranging the time-dependent Schrödinger equation, we find that

$$\frac{\partial\psi(r,t)}{\partial t} = \frac{1}{\mathrm{i}\hbar}\langle r|\, \hat{H}_0\, |\psi\rangle + \frac{W(r)\psi(r,t)}{\hbar}, \tag{2.4}$$

where we have chosen not to evaluate $\langle r|\, \hat{H}_0\, |\psi\rangle$ because it is not necessary to demonstrate our point. Now, if we stipulate that $W(r') < 0$ for all $r' \in [r_{\mathrm{absmin}}, r_{\mathrm{absmax}}]$, equation (2.4) shows that the term $\frac{W(r')\psi(r',t)}{\hbar}$ will work to bring $\psi(r',t)$ to zero over time. If the wave-function $\psi(r',t)$ reaches zero from this effect, then the $\frac{W(r')\psi(r',t)}{\hbar}$ term will become zero as well, and thus the term will cease to contribute further to the time evolution. This out-flux of the wave-function is what we define as absorption.

This is what has been used before to explain fusion absorption [46]. An imaginary Woods-Saxon potential (see equation (2.10) for more details) is constructed that has a negative values of $W(r)$ inside the fusion pocket, and values that tend to zero outside of it. This imaginary Woods-Saxon well is then added to the nuclear potential $U(r)$. After a long time propagation, the flux that reflects off of the Coulomb barrier has an unimpeded time propagation, whilst the flux inside the barrier is completely absorbed after continuous accumulative decay after every intermediate time step.

In this work, we use an absorption potential to account for the never-come-back approximation. The absorption potential will remove any and all flux that penetrates the Coulomb barrier, which is situated further out from the point of touching for the colliding nuclei that we are considering, which means that using the form of the Coulomb interaction in equation (2.1) is reasonable.

2.1.2 Incoming wave boundary condition

Absorption potential methods produce very similar results to methods that use the incoming wave boundary condition (IWB) [47]. Simply put, IWB aims to selectively remove incoming (towards $r = 0$) waves from inside the pocket, whilst not removing the incoming wave from outside the pocket. A difference between using this method over an absorption potential is that, depending on the choice of the operator $\hat{W}$, some flux outside of the Coulomb barrier may be absorbed, whereas IWB does not absorb said flux. This is typical for Woods-Saxon forms of $W(r)$, as they do not immediately attenuate to zero for radii outside the Coulomb barrier radius. Invariably, some amount of flux that does not penetrate the Coulomb barrier will be

absorbed with an absorption potential of this form. Results from time-independent IWB methods will play a role in this thesis; as benchmarks for our time-dependent calculations.

2.2 Coupled-channels Hamiltonian without spin-orbit coupling

The coupled-channels method is a way of treating excitations of colliding nuclei [32]. The definition of a channel is given in section 1.5.1. As the projectile approaches the target, there is an interplay of Coulomb repulsion and nuclear attraction, that can excite roto-vibrational states in the target, projectile, or both. Roto-vibrational states refer to the internal collective motion states of the nuclei, which are modelled as collective rotations and/or vibrations [3]. Attempting to explain these excitations is essential for simulating nuclear reactions. Even at high impact parameters, excitations play a role due to the long range of the Coulomb force, which are known as Coulomb excitations.

We will now derive the coupled-channels Hamiltonian that we will use in calculations. Consider a projectile nucleus of mass M_{P} incident on a deformed target nucleus of mass M_{T}. Assuming that the projectile is both spherical and inert (has no internal states of its own), and the target is in the ground state with spin 0, the Hamiltonian for the relative motion of this system is given by

$$\hat{H} = \frac{-\hbar^2}{2\mu}\hat{\nabla}^2 + \frac{\hat{I}^2}{2\mathcal{I}} + \hat{V} + \hat{V}_{\mathrm{coup}}, \tag{2.5}$$

where $\mu = \frac{M_{\mathrm{P}}M_{\mathrm{T}}}{M_{\mathrm{P}}+M_{\mathrm{T}}}$ is the reduced mass of the projectile-target system, $\hat{I}$ is the target spin, $\mathcal{I}$ is the target moment of inertia, $\hat{V}$ is the nuclear radial potential, $\hat{V}_{\mathrm{coup}}$ is the potential which couples the target spin to the radial motion, and $\hat{\nabla}^2$ is the Laplacian given by

$$\hat{\nabla}^2 = \frac{1}{\hat{r}^2}\frac{\partial}{\partial r}\hat{r}^2\frac{\partial}{\partial r} - \frac{1}{\hbar^2}\frac{\hat{L}^2}{\hat{r}^2}, \tag{2.6}$$

where $\hat{L}$ is the orbital angular momentum. Since the potentials from operators $\hat{V}$ and $\hat{V}_{\mathrm{coup}}$ are not dependent on the angles of the relative motion θ and ϕ, and since there is no spin-orbit coupling, we can express any eigenstate of this Hamiltonian as a product of a radial state and an angular state [4], i.e.

$$\Psi^{m_L}_{n,L}(r,\theta,\phi) = R_{n,L}(r)Y^{m_L}_{L}(\theta,\phi). \tag{2.7}$$

where $R_{n,L}(r) \equiv \langle r|R_{n,L}\rangle$ is the radial state of channel n with spin I_n and orbital angular momentum L, and $Y_L^{m_L}(\theta,\phi)$ are spherical harmonic functions which are eigenstates of $\hat{L}$. In the iso-centrifugal approximation, the spin of the target I_n is uncoupled with the orbital angular momentum of the system L. In this case, the total angular momentum J of both nuclei is simply equal to the orbital angular momentum L. Henceforth, we replace any instance of L with J in order to be consistent with published convention. The validity/applicability of this assumption is discussed later in this chapter. The reason R is a function of both the radial coordinate and spin is due to the effect of the coupling $\hat{V}_{\text{coup}}$.

The remainder of the derivation is covered in appendix B as it is somewhat involved. The derivation involves the substitution $\psi_{n,J}(r) = rR_{n,J}(r)$, and derives the Hamiltonian for the evolution of $\psi_{n,J}(r)$. This collective radial motion Hamiltonian is given by

$$\hat{H}_{\text{CRM}} = \frac{\hbar^2\hat{k}^2_{\text{CRM}}}{2\mu} + \frac{J(J+1)\hbar^2}{2\mu\hat{r}^2} + \frac{\hat{I}^2}{2\mathcal{I}} + \hat{V} + \hat{V}_{\text{coup}}. \tag{2.8}$$

where $\hat{k}_{\text{CRM}} = \mathrm{i}\frac{\partial}{\partial r}$. Finally, we can express the time-dependent Schrödinger equation for the wave-function $\psi_{n,J}(r)$ as

$$\begin{aligned}\mathrm{i}\hbar\frac{\partial\psi_{n,J}(r,t)}{\partial t} = &\left(\frac{-\hbar^2}{2\mu}\frac{d^2}{dr^2} + \frac{J(J+1)\hbar^2}{2\mu r^2} + V(r) + \epsilon_n\right)\psi_{n,J}(r,t) \\ &+ \sum_{n'} V_{nn'}(r)\psi_{n',J}(r,t),\end{aligned} \tag{2.9}$$

where $V_{nn'}(r) = \langle r, I_n|\,\hat{V}_{\text{coup}}\,|r, I_{n'}\rangle$ and $\epsilon_n = \frac{I_n(I_n+1)\hbar^2}{2\mathcal{I}}$ from the rigid rotor model [3]. Solving equation (2.9) can enable us to find several key observables, whilst also allowing us to include time-dependent effects in our description for fusion if we desire.

Note that with the inclusion of the centrifugal potential to our calculation, we will no longer use the term Coulomb barrier in this work. Any description involving a barrier from now on will refer to the potential barrier created by the Woods-Saxon, Coulomb and centrifugal potentials.

2.2.1 Potentials

This section gives the form of the potentials $V(r)$ and $V_{nn'}(r)$. We begin by expressing $V(r) = U(r) + \mathrm{i}W(r)$, i.e.: the sum of the real nuclear potential $U(r)$ from equation (2.3) and a short range absorption potential $W(r)$, the latter of which has the form

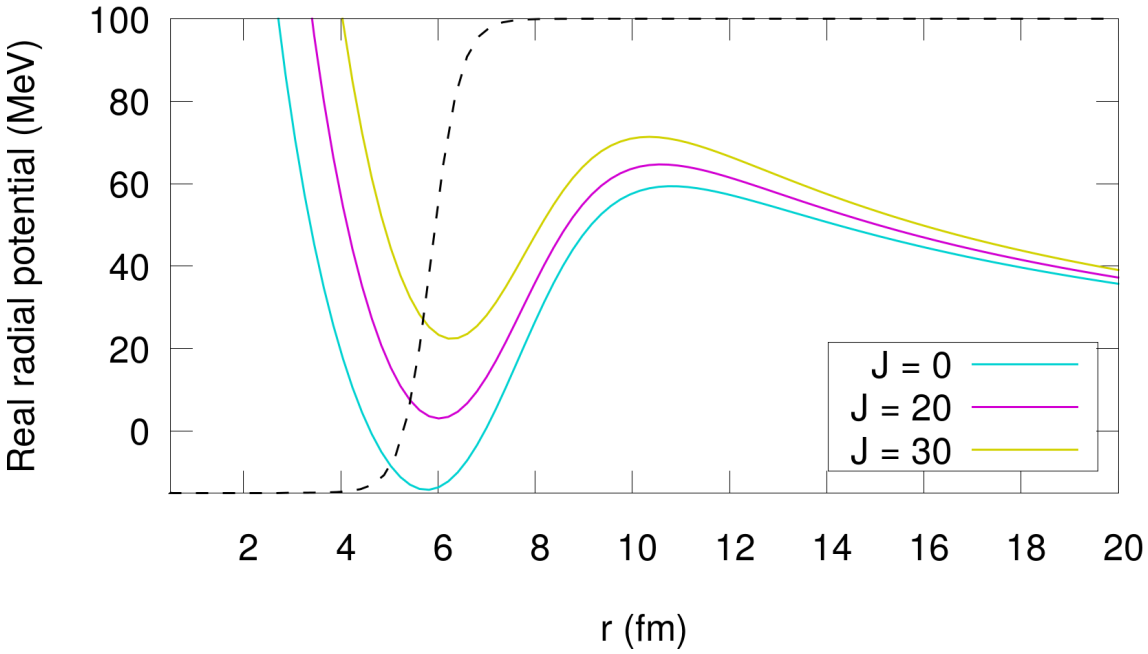

Figure 2.2: Radial potentials for varying J. The cyan, magenta and yellow lines correspond to the potentials for $J = 0$, 20 and 30 respectively. The location of the absorption potential for $J = 0$ is shown as a black dashed line (absorption potential energy values not to scale). The parameters used to generate the Woods-Saxon part of the radial potential are provided in Table 4.2.

$$W(r) = -\frac{W_0}{1 + \exp((r - r_{\text{pock}})/a_{\text{W}})}, \tag{2.10}$$

where r_{pock} is the location of the pocket of the nuclear potential, or the shortest distance where the nuclear potential in equation (2.3) is minimised. We show the real potentials for varying J in Fig. 2.2. In our work, $W(r)$ also contains an absorbing boundary condition at the edge of the numerical radial grid (see appendix C.2 for details on the radial grid). This is because the numerical radial grid has a feature where $\psi_{n,J}(r_{\text{min}}) = \psi_{n,J}(r_{\text{max}})$, which means that particularly penetrative waves or reflected waves can re-route back towards $r = 0$ and affect the calculations.

2.2.2 Coupling matrix elements

As described at the beginning of section 2.2, we model the projectile as inert, and also we assume the target has a ground state rotational band. In this rotational band, we include only the quadrupole and hexadecapole modes for both nuclear and Coulomb excitation. The rotations are modelled as a deformation in the effective radius of the target, which modifies the Woods-Saxon potential [32]

$$V_{\rm N}(r,\hat{O}) = -\frac{V_{\rm WS}}{1+\exp\Big((r-r_{\rm WS}-\hat{O})/a_{\rm WS}\Big)}, \tag{2.11}$$

where $\hat{O}$ is the deformation on the unperturbed radius $r_{\rm WS}$. The quadrupole and hexadecapole terms are contained in $\hat{O}$. The nuclear coupling matrix elements between spins I_n and $I_{n'}$ are evaluated as

$$V_{{\rm N},nn'}(r) = \sum_{\alpha} \langle I_n|\alpha\rangle \langle\alpha|I_{n'}\rangle V_{\rm N}(r,\lambda_\alpha) - V_{\rm N}(r,0)\delta_{nn'}, \tag{2.12}$$

where $\delta_{nn'}$ is the Kronecker delta, $\hat{O}\,|\alpha\rangle = \lambda_\alpha\,|\alpha\rangle$ and

$$V_{\rm N}(r,\lambda_\alpha) = -\frac{V_{\rm WS}}{1+\exp((r-r_{\rm WS}-\lambda_\alpha)/a_{\rm WS})}. \tag{2.13}$$

The last term in equation (2.12) prevents double counting of the Woods-Saxon potential when $n = n'$. In the rotational basis, the matrix elements of the operator $\hat{O}$ are given by

$$\langle I_n|\,\hat{O}\,|I_{n'}\rangle = r_{\rm T}\left(\beta_2\mathcal{F}(2,I_n,I_{n'}) + \beta_4\mathcal{F}(4,I_n,I_{n'})\right), \tag{2.14}$$

where $r_{\rm T} = r_{\rm coup}A_T^{1/3}$, $r_{\rm coup}$ is the coupling radius parameter, β_2 and β_4 are the deformation parameters for the quadrupole and hexadecapole modes respectively, and

$$\mathcal{F}(I,I_n,I_{n'}) = \sqrt{\frac{(2I+1)(2I_n+1)(2I_{n'}+1)}{4\pi}}\begin{pmatrix} I_n & I & I_{n'} \\ 0 & 0 & 0 \end{pmatrix}^2, \tag{2.15}$$

where the bracketed array is a 3-j symbol. We also include the deformed target Coulomb interaction, up to second order in the expansion of β_2 and first order in β_4. This term is given by

$$\begin{aligned} V_{{\rm C},nn'}(r) = {} & \frac{3Z_{\rm P}Z_{\rm T}}{5}\frac{r_{\rm T}^2}{r^3}\left(\beta_2 + \frac{2}{7}\sqrt{\frac{5}{\pi}}\beta_2^2\right)\mathcal{F}(2,I_n,I_{n'}) \\ & + \frac{3Z_{\rm P}Z_{\rm T}}{9}\frac{r_{\rm T}^4}{r^5}\left(\beta_4 + \frac{9}{7\sqrt{\pi}}\beta_2^2\right)\mathcal{F}(4,I_n,I_{n'}). \end{aligned} \tag{2.16}$$

The total interaction potential $V_{nn'}(r)$ in equation (2.9) is given by the sum of the nuclear and Coulomb components (i.e.: $V_{nn'}(r) = V_{{\rm N},nn'}(r) + V_{{\rm C},nn'}(r)$). For

all results in this thesis, we include the 0^+, 2^+ and 4^+ states in the ground state rotational band of the target.

2.3 On the iso-centrifugal approximation

We expect the iso-centrifugal approximation to hold for instances when the projectile and target are not able to get very close to one another. This is expected to be the case for high J values, but is invalid for low J values. A formal treatment of the spin-orbit interaction has been relegated to the future work section, but we will briefly explain the process here for clarity.

Essentially, in order to incorporate the spin-orbit interaction, a substitution of $\hat{L} = \hat{J} - \hat{I}$ is performed into the Laplacian (equation (2.6)) [48]. The cross terms from the squaring of $\hat{L}$ are responsible for the spin-orbit interaction, and thus when fully expanded are modulated by the inverse distance pre-factor. This is why the iso-centrifugal approximation is said to be applicable when the distance between the target and projectile is large.

However, this pre-factor also contains the term $(\mu)^{-1}$ when fully expanded. For collisions where the target is significantly larger than the projectile, and the projectile is small, then $\mu \to M_{\mathrm{P}}$, and thus the interaction term can become relevant even if J is high. For our work, this term is neglected in order to simplify calculations for efficiency, but it is definitely a relevant term for nuclear collisions in general.

2.4 Wave-packets

We will now show the form of the incident wave-function that we use in this work. The label αi is used to refer to the entrance channel of the reaction, which is initial nuclear configuration and quantum numbers of the target and projectile. The initial wave-function of our time propagation is known as a wave-packet. One form of the wave-packet that we use is a Gaussian envelope boosted by a plane wave, which is given by the expression

$$\psi_{\alpha i,J}(r,t_i) = \langle r|\psi_{\alpha i,J}(t_i)\rangle = \exp\left(\frac{-(r-r_i)^2}{2\sigma_i^2}\right) \times \exp(-ik_i r), \tag{2.17}$$

where t_i is the initial time (which is a constant), r_i is the centre of the initial wave-packet, σ_i the radial width and k_i is the average wave-number for the incident wave packet, which depends on the incident energy E_i and σ_i and is found by solving $E_i = \langle\psi_{\alpha i,J}|\,\hat{H}_{\mathrm{CRM}}\,|\psi_{\alpha i,J}\rangle$. For details on how the wave-function is propagated in time using Hamiltonian $\hat{H}_{\mathrm{CRM}}$, refer to appendix A.4 for the form of the time propagator,

and appendix C for the method we use that calculates the necessary matrix elements. Together, the methods described in these appendices culminate to form our novel TDCCWP method.

Later in this thesis, we find that other forms of equation (2.17) are more effective for some calculations. However, we refer to these alternative wave-functions as wave-packets still. This is because they embody the spirit of the wave-packet; they are a spatially modulated envelope function which is boosted towards $r = 0$. The choice of these alternate wave-packets is novel, and is motivated in further detail in chapter 5 (equation (5.13)).

Chapter 3

The window operator method

This chapter details the window operator method, which is a method that helps us generate more tangible results from the wave-function, which can be compared to nuclear physics experiments. The window operator is part of a class of operators that resolve wave-packets into specific energy components, which is crucial in order to correctly match the experimental conditions for nuclear collisions [4]. Similar operators to the window operator, that are also explored in this thesis, are the Green's operators [12].

3.1 Transmission coefficients

The transmission, defined as any flux that penetrates the potential barrier, is an important quantity for determining absorption cross sections. Absorption cross sections are the cross sections associated with the absorption process described in section 2.1. An example of an absorption cross section that we can calculate is known as the elastic absorption cross section, which is the absorption cross section in the entrance channel. For our scattering problem, the elastic absorption cross section is given by [4]

$$\sigma_{\text{abs,el}}(E) = \frac{\pi\hbar^2}{2\mu E}\sum_J (2J+1)\mathcal{T}_{\text{el}}(E,J), \tag{3.1}$$

where $\mathcal{T}_{\text{el}}(E,J)$ is the energy resolved transmission coefficient for the collision state with energy E and orbital angular momentum J in the entrance (or elastic) channel. The reason why these quantities are resolved in energy is because the states prepared in experiments have narrow energy distributions. With the method that we have currently proposed, we cannot accurately perform sums like in (3.1) by merely calculating the transmission content of our wave-packets. This is because the wave-packets that we propagate are not resolved in energy; instead they exist as a super-

position of energies. Thus, we require a method that can resolve the wave-packets in energy, which can be achieved using the window operator method [49,50]. Whilst equation (3.1) does depend on the elastic transmission, in this chapter and the next we focus on the total transmission from integrating over all channels, since this is more convenient when bench-marking our results from those of time-independent methods.

Using the window operator method, we can calculate transmission coefficients using [51]

$$\mathcal{T}_\alpha(E,J) = 1 - \mathcal{R}_\alpha(E,J), \tag{3.2}$$

where $\mathcal{T}_\alpha(E,J)$ is the transmission from all channels from the initial state $|\psi_{\alpha i,J}(t_i)\rangle$, where we have labelled the initial spin state/channel using the label αi, and $\mathcal{R}_\alpha(E,J)$ is the reflection coefficient given by

$$\mathcal{R}_\alpha(E,J) = \frac{\mathbb{P}_{f,J}(E)}{\mathbb{P}_{\alpha i,J}(E)} = \frac{\langle\psi_{f,J}|\,\hat{\Delta}(E)\,|\psi_{f,J}\rangle}{\langle\psi_{\alpha i,J}(t_i)|\,\hat{\Delta}(E)\,|\psi_{\alpha i,J}(t_i)\rangle}, \tag{3.3}$$

where $|\psi_{f,J}\rangle$ is the final state from the time propagation of $|\psi_{\alpha i,J}(t_i)\rangle$, $\mathbb{P}(E)$ is the probability of a state having energy E and $\hat{\Delta}(E)$ is an energy projection operator that behaves similarly to $\delta(\hat{H}_{\mathrm{CRM}} - E)$. We can choose to use a window operator for the energy projection, which is given by [49,50]

$$\hat{\Delta}(E) \equiv \hat{\Delta}(\hat{H}_{\mathrm{CRM}}, E, \zeta, n) = \frac{\zeta^{2^n}}{(\hat{H}_{\mathrm{CRM}} - E)^{2^n} + \zeta^{2^n}}, \tag{3.4}$$

where ζ is known as the energy resolution parameter and n is a positive integer that controls the shape of the energy window/bin. With this operator, $\langle\psi|\,\hat{\Delta}(E)\,|\psi\rangle$ represents the probability of finding the system, in state $|\psi\rangle$, with energy in the range $E \pm \zeta$. The energy spectrum is constructed for a set of energies E_k where $E_{k+1} = E_k + 2\zeta$. We can express $\mathbb{P}(E_k) = \langle\Omega_{E_k}|\Omega_{E_k}\rangle$, which can be calculated by solving the equation

$$((\hat{H}_{\mathrm{CRM}} - E_k)^n - \mathrm{i}\zeta^n)\,|\Omega_{E_k}\rangle = \zeta^n\,|\psi\rangle\,. \tag{3.5}$$

Here, the $|\Omega_{E_k}\rangle$ states represent energy resolved bin states with energy in the range $E_k \pm \zeta$. Equation (3.5) is applicable only when $\hat{H}_{\mathrm{CRM}}$ is Hermitian. Whilst our Hamiltonian includes an absorption potential (and thus is not Hermitian), the absorption term can be neglected when using the window operator. This is because the initial and final states we use in equation (3.3) are far away from the range of the absorption, so the influence of the absorption potential on these states is negligible.

3.2 Hamiltonian matrix

The form of the Hamiltonian matrix that we use in equation (3.5) is a collection of several smaller matrices that account for our basis choice used. As an example, for a target that has three states in its ground state rotational band ($0^+, 2^+$ and 4^+ for instance), the Hamiltonian matrix equation takes the form

$$\bar{H}_{\mathrm{CRM}}\vec{\psi} = \begin{pmatrix} \begin{pmatrix} 0^+ - 0^+ \end{pmatrix} & \begin{pmatrix} 0^+ - 2^+ \end{pmatrix} & \begin{pmatrix} 0^+ - 4^+ \end{pmatrix} \\ \begin{pmatrix} 2^+ - 0^+ \end{pmatrix} & \begin{pmatrix} 2^+ - 2^+ \end{pmatrix} & \begin{pmatrix} 2^+ - 4^+ \end{pmatrix} \\ \begin{pmatrix} 4^+ - 0^+ \end{pmatrix} & \begin{pmatrix} 4^+ - 2^+ \end{pmatrix} & \begin{pmatrix} 4^+ - 4^+ \end{pmatrix} \end{pmatrix} \begin{pmatrix} \begin{pmatrix} 0^+ \end{pmatrix} \\ \begin{pmatrix} 2^+ \end{pmatrix} \\ \begin{pmatrix} 4^+ \end{pmatrix} \end{pmatrix}. \tag{3.6}$$

Here, the vector $\vec{\psi}$ is comprised of the three spatial wave-functions for each rotational state stacked on top of one another. This definition is convenient to code because it allows us to define a single matrix for the matrix multiplication. In this Hamiltonian matrix of matrices, the matrices on the diagonal of $\bar{H}_{\mathrm{CRM}}$, referred to henceforth as the self coupled-channel matrices, are a sum of the kinetic matrix, the diagonal potential matrix arising from the potential operator $\hat{V}$, $\hat{V}_{\mathrm{coup}}$ and the centrifugal potential, as well as a diagonal matrix of the excitation energies ϵ_n (see equation (2.8) for more details on each operator). The matrices off the diagonal, a.k.a. the non-self coupled-channel matrices, are contributions solely from the operator $\hat{V}_{\mathrm{coup}}$. We will illustrate how to construct these matrices below. Both the self and non-self coupled-channel matrices are square radial matrices with dimensions $N \times N$, where N is the number of sampling points in the radial Fourier grid (see appendix C.2 for more details).

3.2.1 Self coupled-channel matrix elements

The self coupled-channel matrix $(I_n - I_n)$ is a mixture of diagonal and non-diagonal matrices. It can be expressed as

$$(I_n - I_n) = \bar{K} + \bar{U}_J + \bar{V}_{nn} + \epsilon_n \mathbb{1}, \tag{3.7}$$

where $\bar{K}$ is the kinetic matrix, $\bar{U}_J$ is the Coulomb, Woods-Saxon and centrifugal

potential matrix, $\bar{V}_{nn}$ is the diagonal coupling potential matrix, and $\mathbb{1}$ is the identity matrix. The diagonal elements of the self coupled-channel matrix are given by

$$(I_n - I_n)_{jj} = \bar{K}_{jj} + U(r_j) + \frac{J(J+1)\hbar^2}{2\mu r_j^2} + V_{nn}(r_j) + \epsilon_n, \tag{3.8}$$

where r_j is the j^{th} element of the radial Fourier grid, and $U(r), V_{nn}(r)$ are the same potentials as those used in equation (2.9). The off diagonal elements are given by

$$(I_n - I_n)_{jj'} = \bar{K}_{jj'}. \tag{3.9}$$

We can express the kinetic matrix elements using the discrete variable representation (DVR). Assuming the maximum radial grid point $r_{\max}$ is large for our system, we can express the kinetic matrix elements for an evenly spaced grid as [52]

$$\bar{K}_{jj'} = \frac{\hbar^2}{2\mu\Delta r^2}(-1)^{(j-j')} \begin{cases} \pi^2/3 - 1/(2j^2), & \text{if } j = j'. \\ 2/(j-j')^2 - 2/(j+j')^2, & \text{otherwise,} \end{cases} \tag{3.10}$$

where Δr is the radial grid spacing.

3.2.2 Non-self coupled-channel matrices

The non-self coupled-channel matrices are constructed more simply than the self coupled-channel matrices of $\bar{H}_{\text{CRM}}$. The non-self coupled-channel matrix $(I_n - I_{n'})$ is a diagonal matrix with elements

$$(I_n - I_{n'})_{(jj)} = V_{nn'}(r_j), \tag{3.11}$$

where $V_{nn'}(r)$ is the coupling potential from equation (2.9).

3.3 Window operator properties

We can analyse the properties of the window operator in order to determine appropriate values of its constants that we should use. We can rewrite the probability $\langle\psi|\,\hat{\Delta}(\hat{H}_{\text{CRM}}, E_k, \zeta, n)\,|\psi\rangle$ as

$$\langle\psi|\,\hat{\Delta}(\hat{H}_{\text{CRM}}, E_k, \zeta, n)\,|\psi\rangle = \sum_E \langle\psi|\Phi_E\rangle\,\Delta(E, E_k, \zeta, n)\,\langle\Phi_E|\psi\rangle\,, \tag{3.12}$$

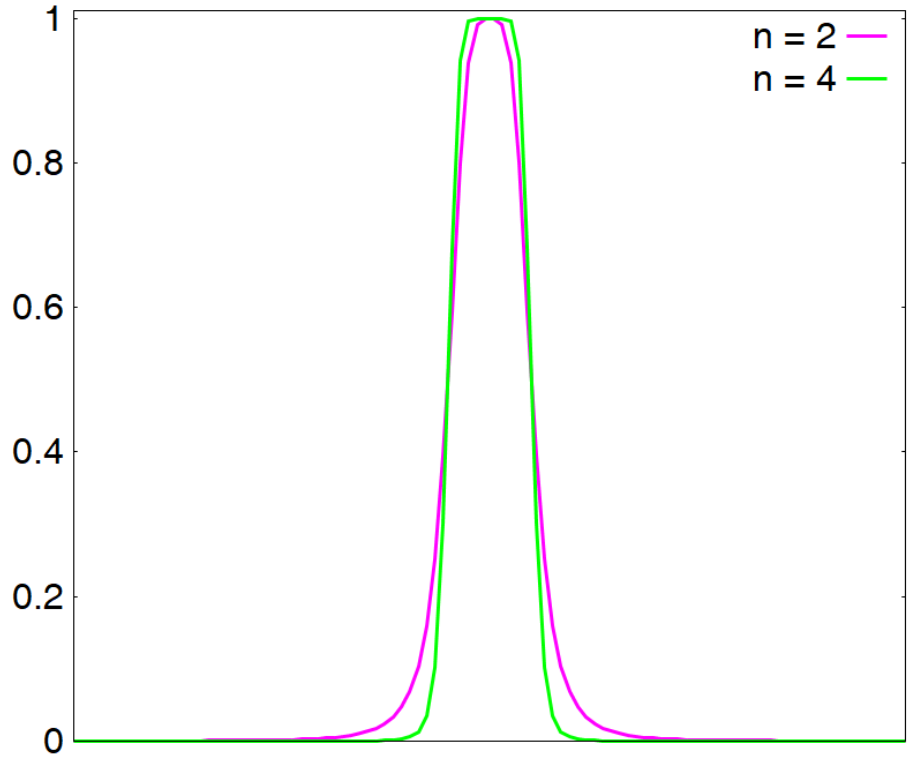

Figure 3.1: Two energy windows centered at E_k for arbitrary ζ with varying n. Increasing n makes the window more rectangular.

where $\Delta(E, E_k, \zeta, n) = \frac{\zeta^{2n}}{(E-E_k)^{2n}+\zeta^{2n}}$, $\hat{H}_{\text{CRM}} |\Phi_E\rangle = E |\Phi_E\rangle$ and $\langle\Phi_E|\psi\rangle$ are the energy coefficients of state $|\psi\rangle$. In other words, the window operator now weights the energy coefficients of state $|\psi\rangle$. But what does this weighting look like whilst varying the parameters? If we increase ζ, we simply increase the width of the distribution. ζ is the parameter that affects the closeness of the energy window/bin to the central energy E_k. Increasing n makes the windows more rectangular in shape, as shown in Figure 3.1.

If we apply the limit $n \to \infty$, the weighting function becomes rectangular, and then the summand of equation (3.12) can be written as

$$\lim_{n\to\infty} \left[\langle\psi|\Phi_E\rangle \, \hat{\Delta}(E, E_k, \zeta, n) \, \langle\Phi_E|\psi\rangle \right] = \begin{cases} |\langle\Phi_E|\psi\rangle|^2 & E_k - \zeta \leq E \leq E_k + \zeta \\ \\ 0 & \text{otherwise} \end{cases}, \tag{3.13}$$

or in other words, equation (3.12) only includes the energy coefficients of energies in the interval $[E_k - \zeta, E_k + \zeta]$ in this limit.

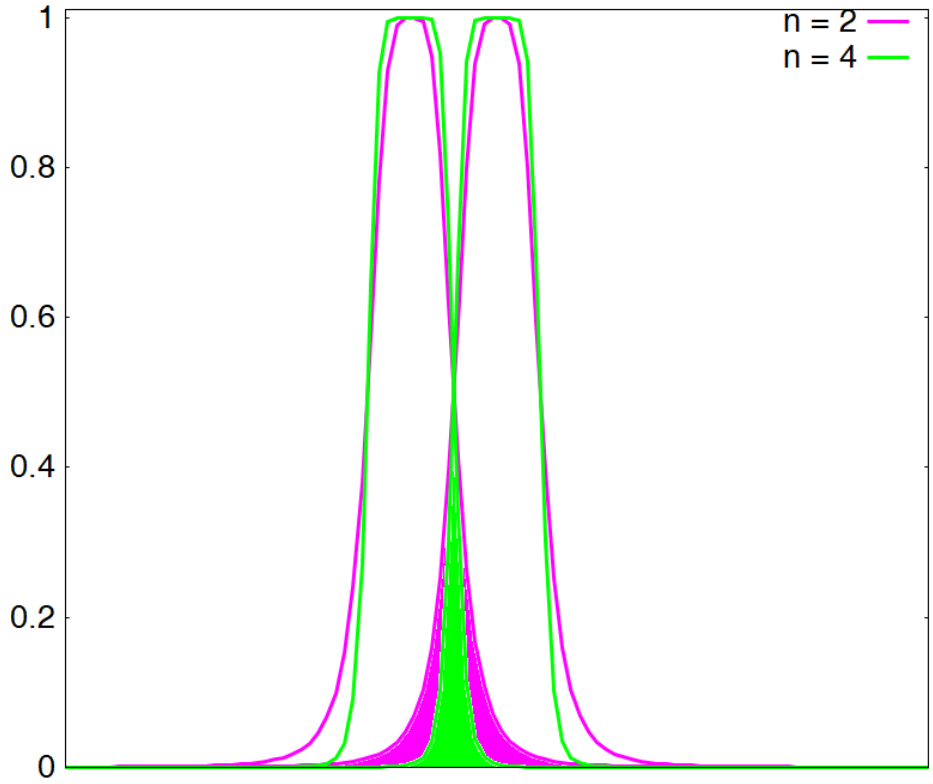

Figure 3.2: Two energy windows centered at E_k and E_{k+1}, separated by 2ζ for arbitrary ζ with varying n. The overlap for $n = 4$ is shown by the inner green coloured area, and for $n = 2$ it is the sum of both the green and magenta coloured areas.

We construct a set of sampling energies $\{E_k\}$ with the difference between adjacent sampling energies E_k and E_{k+1} equal to 2ζ. This ensures the windows are lined up next to each other, and no window shares coefficients in the limit $n \to \infty$. For finite n the windows overlap, and can share coefficients, as shown in Figure 3.2.

Increasing n increases the computational effort needed to generate the coefficients. Typically, $n = 2$ is used as it is often good enough to produce correct results despite the relatively high overlap between adjacent window functions. In general, overlap is not desirable, since we use all of the energy windows to normalise the probabilities $\mathbb{P}(E)$. The accuracy of the window operator is mainly affected by the absolute size of the energy coefficients $\langle \Phi_E | \psi \rangle$. If the energy coefficients of state $|\psi\rangle$ in the energy window $E_k \pm \zeta$ are too low, then the $|\Omega_{E_k}\rangle$ state generated by the window operator calculation will be inaccurate. We will see how this limits our TDCCWP method in the next chapter, and how it can be circumvented.

3.4 Why not propagate asymptotic eigenstates?

If we require energy resolved transmission coefficients, one may wonder why we do not simply propagate the eigenstates of the asymptotic Hamiltonian (which is the Hamiltonian in the limit $r \to \infty$), and calculate the transmission by performing a radial integral across the fusion pocket. In general, using the window operator on a propagated wave-packet is faster. This is because the numerical grid sizes needed to support the propagation of energy eigenstates are too large for efficient calculations. The window operator method allows one to use more sensible grid sizes and parameters to perform the energy resolution.

Chapter 4

^{16}O + ^{154}Sm TDCCWP window operator results

In this chapter, we present the results of single and multi channel propagations for ^{16}O + ^{154}Sm collisions. The incident wave-packet that we use in equation (3.3) is chosen to be a Gaussian envelope with a plane-wave boost, like in equation (2.17). Firstly, we present results for a single channel head-on collision without absorption to ensure the propagator is accurate, and then compare these to the results with the absorption potential active. The absorption transmission coefficients from the window operator method are compared to those from the time-independent Schrödinger equation (TISE). Then, we introduce the three channels and varying J values and perform the same comparison to the TISE. The Fourier grid, initial wave-packet, absorption potential and window operator parameters used can be found in Table 4.1, and the Woods-Saxon and coupled-channels parameters that we used are shown in Table 4.2. As mentioned in section 2.2, the term 'barrier' refers to the potential barrier produced by the Woods-Saxon, Coulomb and centrifugal potentials. A publication in Physical Review C using results from this chapter can be found in reference [53].

4.1 Single channel propagation without absorption

We begin by looking at propagations for a single channel Hamiltonian, in order to quantify the quality of our numerical time propagator. We define a quantity called the fidelity measure as

$$\begin{aligned} F_{\mathbb{1}} &= |\langle\psi(t_i)|\psi(t_i)\rangle - \langle\psi(t)|\psi(t)\rangle| \\ &= |1 - \langle\psi(t)|\psi(t)\rangle|, \end{aligned} \tag{4.1}$$

where || denotes the absolute value. Similarly, we define the energy fidelity measure

Table 4.1: Model parameters used for the Fourier grid, wave-packet, imaginary potential and window operator.

Variable	Value	Description
N	2048	No. of sampling points in the Fourier grid
$r_{\min}$/fm	0.5	Minimum value of r in the Fourier grid
$r_{\max}$/fm	500	Maximum r in Fourier grid
Δt/s	10^{-22}	Propagator time step
r_i/fm	200	Initial position of wave-packet
σ_i/fm	10	Width parameter of initial wave-packet
W_0/MeV	50	Imaginary potential well height
a_{W}/fm	0.3	Imaginary potential well range
n	2	Window operator overlap parameter
ζ/MeV	0.5	Window operator resolution parameter

as

$$\begin{aligned} F_E &= |\langle\psi(t_i)|\hat{H}|\psi(t_i)\rangle - \langle\psi(t)|\hat{H}|\psi(t)\rangle| \\ &= |E_i - \langle E(t)\rangle|. \end{aligned} \tag{4.2}$$

In principle, for propagations with no absorption, the value for both $F_{\mathbb{1}}$ and F_E should be zero, since information/energy is conserved. The energy fidelity measure and fidelity measure of the propagation without absorption are shown in Figs. 4.1(a) and 4.1(b) respectively. Both quantities remain acceptably small throughout the propagation. A high quality fidelity is needed in order to discern between loss of information/energy due to actual physical processes, and loss of information/energy due to the numerical implementation of the propagator. We shall see later that we are indeed able to discern these two effects.

4.2 Single channel propagation with absorption

The difference between not including and including the absorption potential can be illustrated clearly by comparing Fig. 4.2 and Fig. 4.3, which show the time evolution of the wave-packet without and with absorption respectively. With the absorption, the information close to $r = 0$ in the radial pocket is completely absorbed, unlike in Fig. 4.2(b) where some information is trapped inside the pocket. Thus, the propagation in Fig. 4.3 should only contain outgoing waves (since incoming waves either get reflected by the barrier and become outgoing, or penetrate the barrier and get absorbed), which can be verified using Fig. 4.4(c), which shows that after the interaction the momentum density is located solely in the positive-k (outgoing) region.

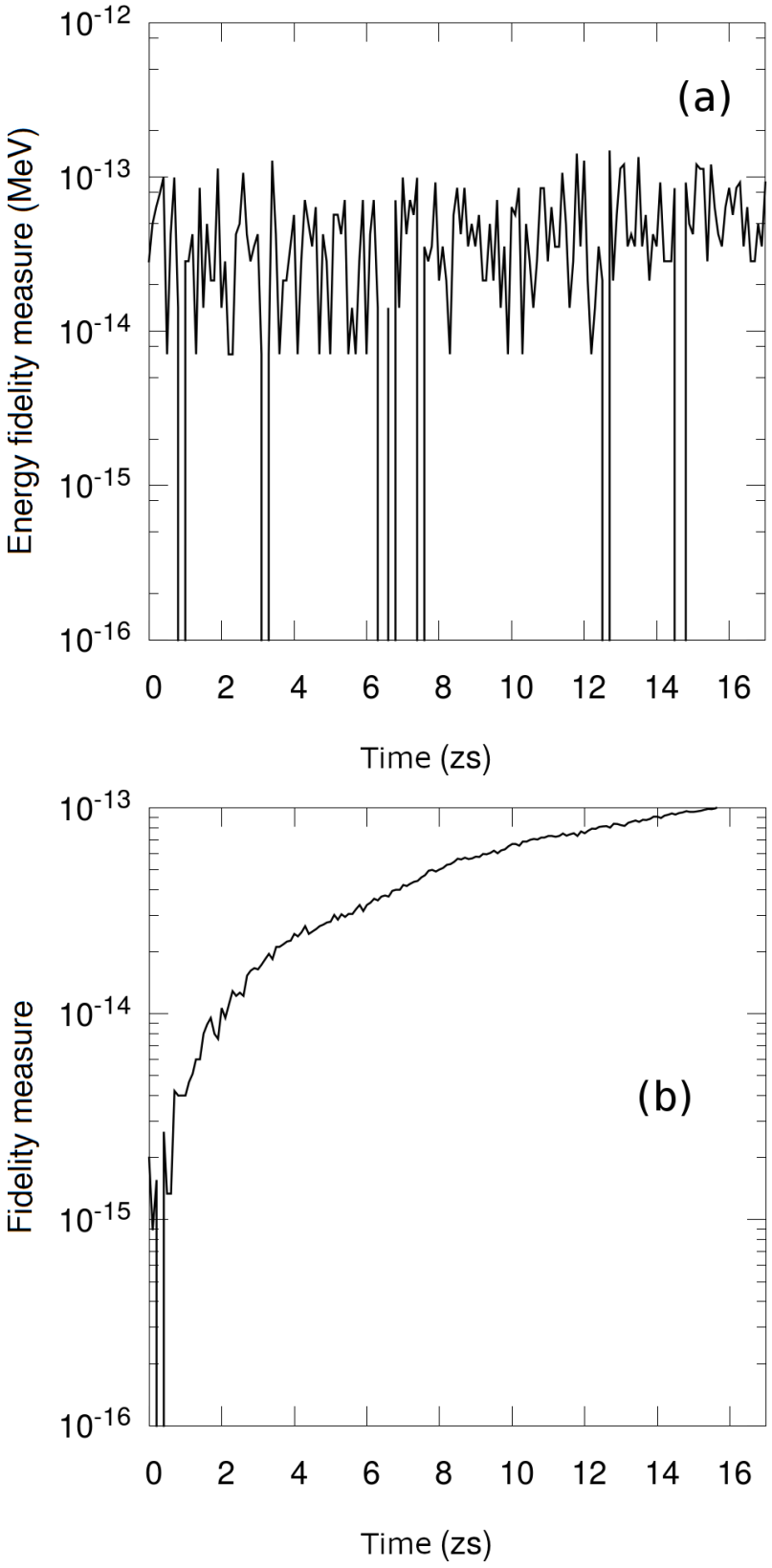

Figure 4.1: (a) Energy and (b) normalisation fidelity measures (see text) over time for the single-channel propagation in Fig. 4.2.

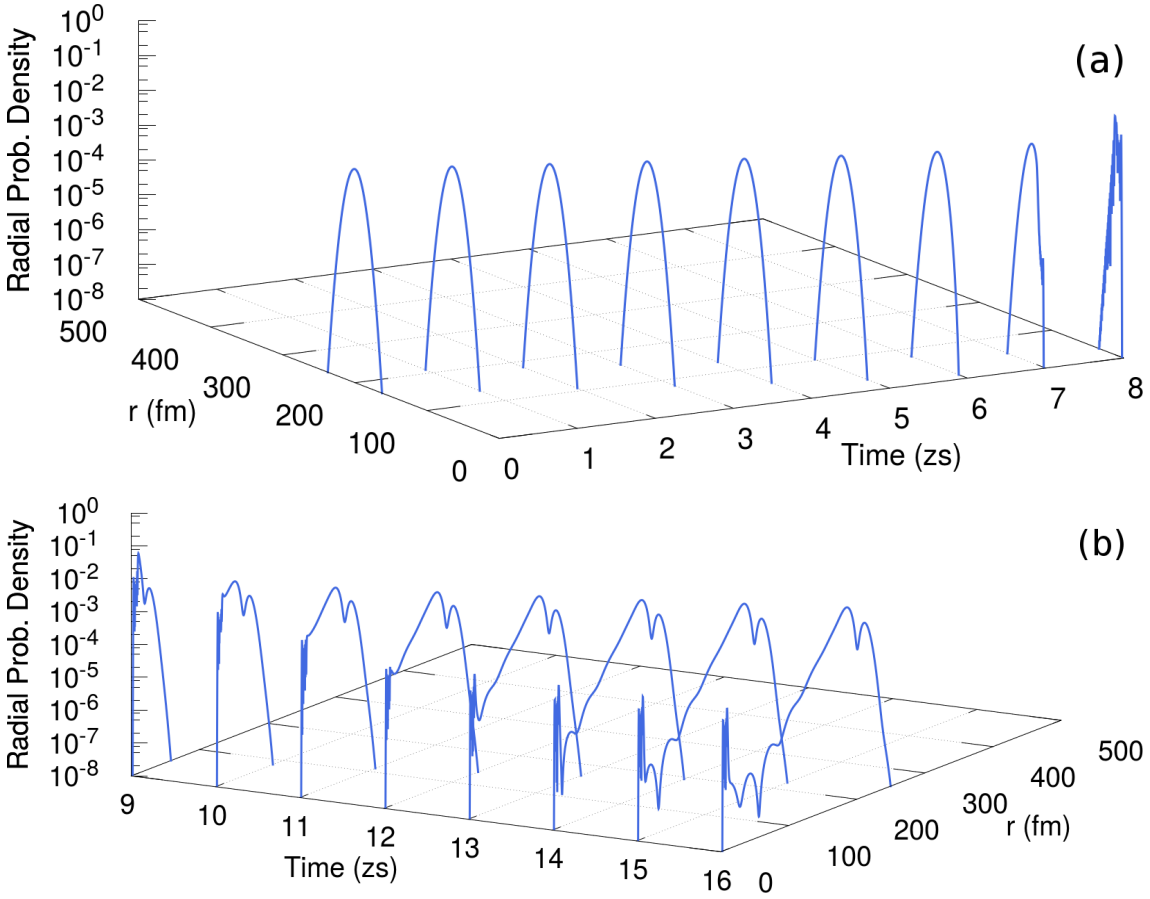

Figure 4.2: Evolution of the radial probability density (a) from 0 to 8 zs, and (b) from 9 to 16 zs, for $J = 0$ and $E_i = 60$ MeV for the single-channel ^{16}O+^{154}Sm collision, without absorption.

We can see in Fig. 4.5 that the expectation energy and state population ($\langle\psi(t)|\,\hat{H}\,|\psi(t)\rangle$ and $\langle\psi(t)|\psi(t)\rangle$ respectively) decrease due to the absorption. In Fig. 4.5(a), the loss of average energy is due to the decrease of the high energy components of the energy probability distribution of the time-dependent state. The magnitude of the decrease due to absorption is much greater than the magnitude of decrease solely due to the numerical propagation in Fig. 4.1, indicating that we can accurately discern the absorption from the numerical error in Fig. 4.1.

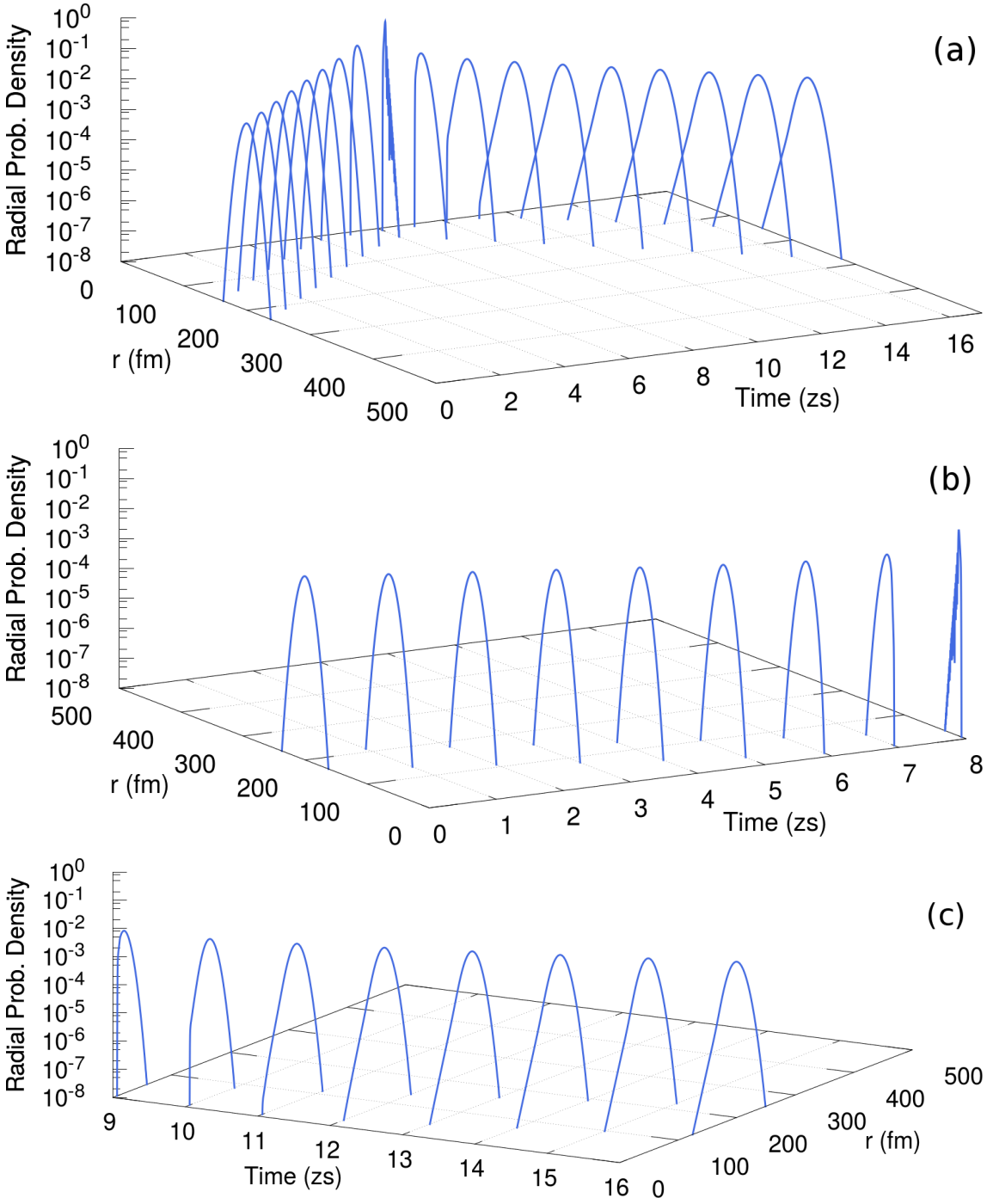

Figure 4.3: Evolution of the radial probability density (a) across the whole time period, b) from 0 to 8 zs, and c) from 9 to 16 zs, for the same setup used in Fig. 4.2, but with the absorption potential present.

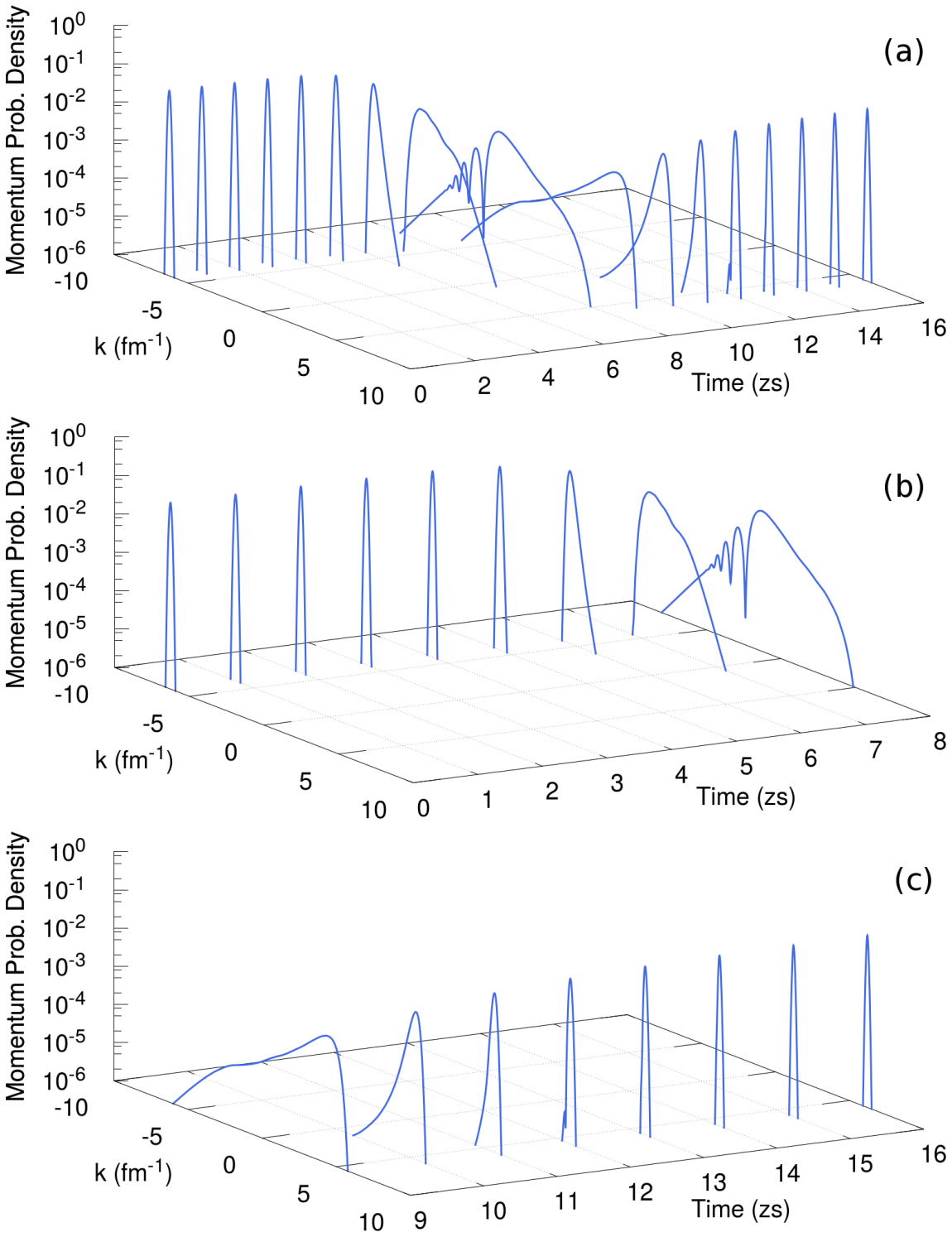

Figure 4.4: The same as in Fig. 4.3, but for the momentum probability density.

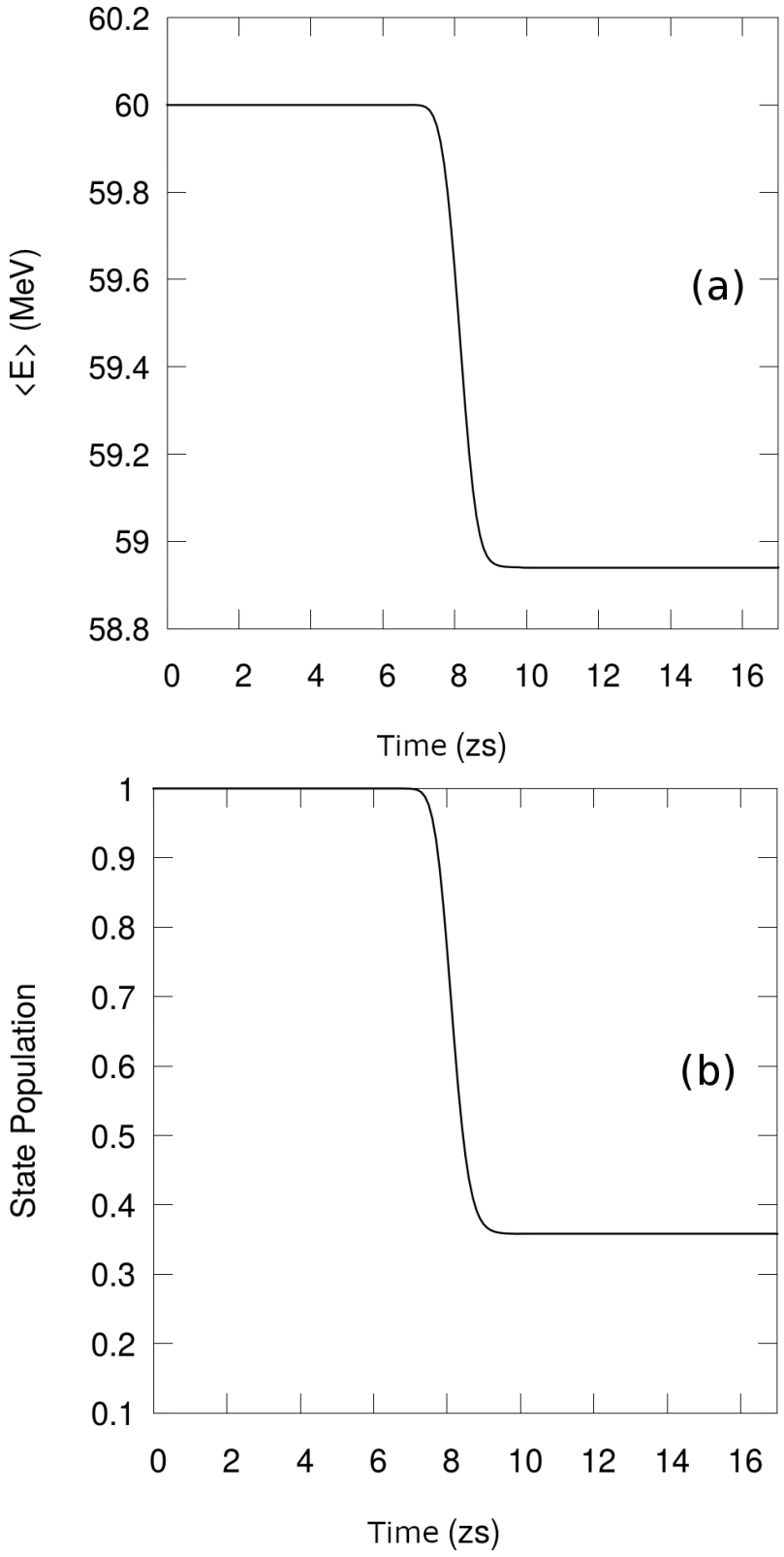

Figure 4.5: (a) Expectation energy and (b) normalisation over time for the single-channel propagation in Fig. 4.3.

4.3 Single channel transmission coefficients

When the momentum density is in the positive-k region only, then the results calculated by solving the TISE for positive momentum states and the results calculated using these outgoing wave-packets should be equivalent. We choose the final state $|\psi_{f,J}\rangle$ in equation (3.3) to be the state $t = 16$ zs. Using the energy-resolved states generated by acting the window operator on our initial and final states, we compare the transmission coefficients from our TDCCWP method and the TISE in Fig. 4.6 for a number of incident energies E_i. For each E_i, we can see that some TDCCWP transmission coefficients are in agreement with the TISE curve, but then there are deviations at energies further away from E_i. This is what we expect from our window operator calculation, since for energy values close to E_i, the wave-packet energy coefficients are relatively high in magnitude, which makes the calculation from the window operator more numerically accurate (as mentioned in section 3.3). However, once one performs calculations for energies outside of this energy range, then the energy coefficients are no longer high enough to calculate the transmission accurately. In principle, the transmission coefficients should not depend on the choice of E_i in our model, since the transmission coefficients are calculated as overlap integrals of energy eigenstates, and the eigenstates of the Hamiltonian are not dependent on E_i.

We illustrate a method to circumvent this effect in Fig. 4.7, which shows a portion of the probabilities generated by applying the window operator on the initial state of $E_i = 60$ MeV. Whilst the final probabilities are also important in determining the transmission, they are not needed to be shown here to illustrate this point. Here, the probability $\mathbb{P}_{\alpha i,J}(E) \approx |\langle \Phi_E | \psi_{\alpha i,J}(t_i) \rangle|^2$, where $\langle \Phi_E | \psi_{\alpha i,J}(t_i) \rangle$ is the energy coefficient of the initial state (see equation (3.12) for details on energy coefficients). In Fig. 4.7(a), for energies close to E_i, the probabilities $\mathbb{P}_{\alpha i,J}(E)$ (and thus the energy coefficients) are relatively high in absolute value, which results in a convergent calculation of the transmission coefficients. However, past $E = 1.08V_B$ for instance, where V_B is the barrier energy, the energy coefficients are now too low in order to calculate the transmission coefficients accurately. Therefore, if we then propagate with another incident wave-packet (with $E_i = 62.5$ MeV, for instance), as shown in Fig. 4.7(b), then the coefficients past $E = 1.08V_B$ are higher relative to those of $E_i = 60$ MeV, and so the transmission calculation for $E_i = 62.5$ MeV in that energy region should be more convergent to the expected TISE results.

Not only are the $E_i = 62.5$ MeV coefficients more convergent in the $E > 1.08V_B$ region, but the transmission coefficients from both the $E_i = 62.5$ MeV and $E_i = 60$ MeV curves in Fig. 4.6 overlap with one another. This is because there are energy regions where the energy coefficients are high for both wave-packets. This allows one to perform multiple propagations with differing E_i, collect the results, and chain together the transmission coefficients to form a total transmission coefficient profile that is convergent across an energy range. However, there is a numerical limit to this technique - when E_i is much smaller than the barrier energy, then none of the probabilities from the window operator will be accurate, since the reflection coefficient in equation (3.3) is very close to unity for that wave-packet, and therefore

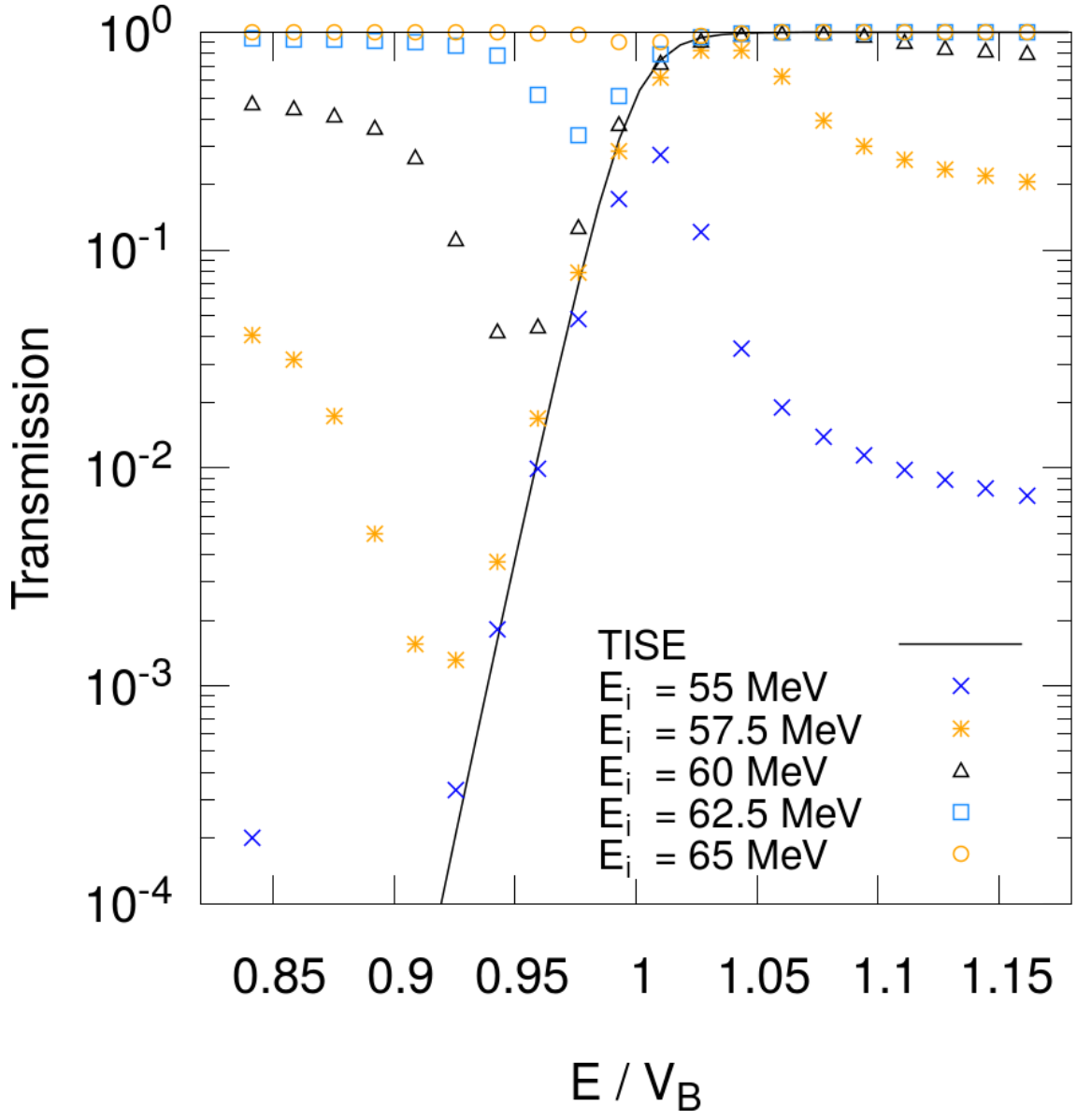

Figure 4.6: Energy-resolved transmission coefficients using the window operator method for $J = 0$ and the TISE results from using the CCFULL code of Ref. [32]. The profile resulting from the overlap of these E_i profiles shows the transmission coefficients (explained in text, shown in Fig. 4.8). Barrier energy for $J = 0$ is equal to 59.41 MeV

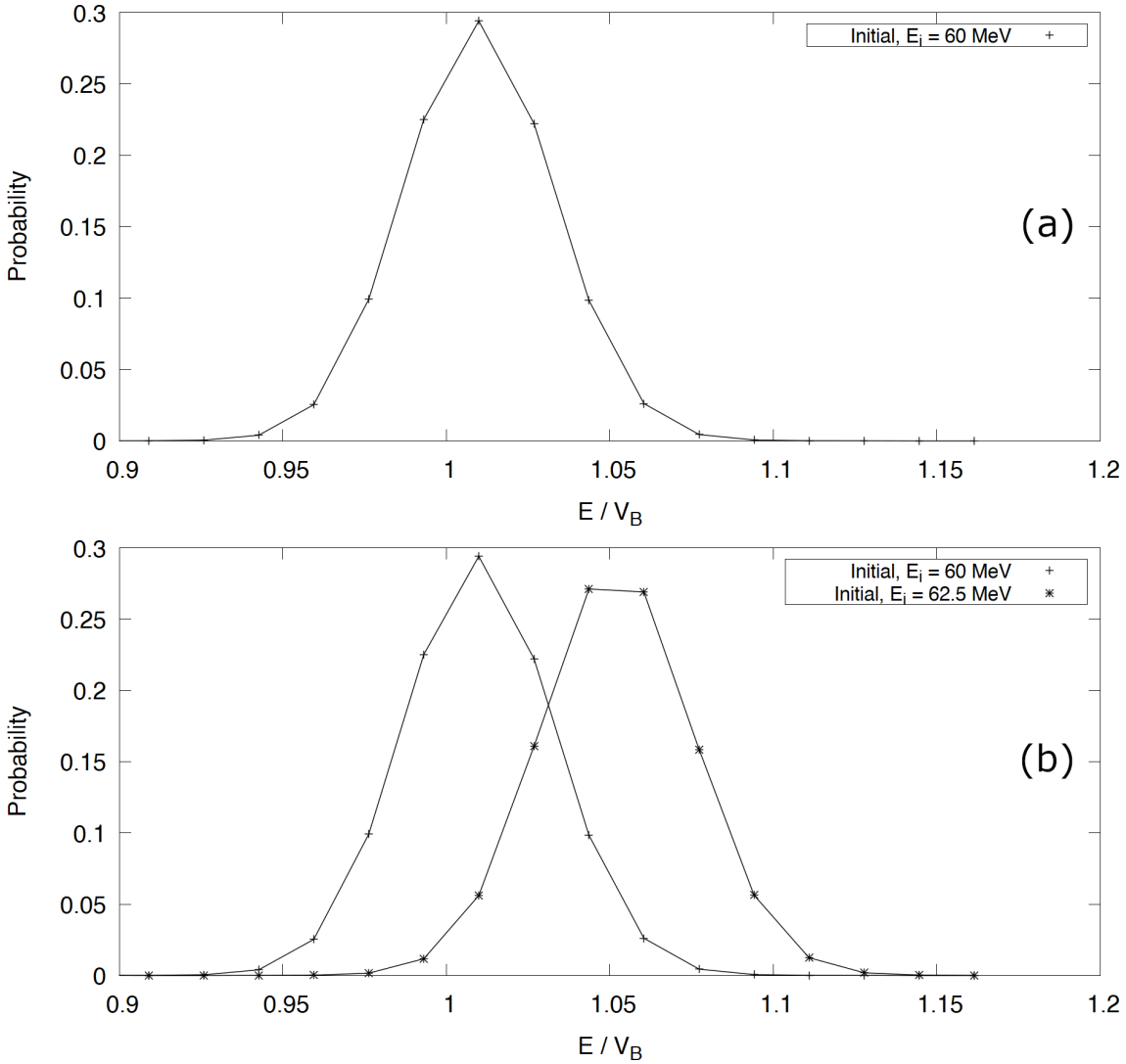

Figure 4.7: Window operator probabilities $\mathbb{P}(E)$ for the energy resolved initial states with (a) $E_i = 60$ MeV and (b) $E_i = 60$ MeV and 62.5 MeV.

the calculation of the transmission using the subtraction in equation (3.2) becomes inaccurate.

In order to overlap the transmission coefficients correctly, we employ a simple procedure. Firstly, for a given value of J, start with the lowest value of E_i, denoted by $E_{i,0}$. Then, compare the $E_{i,0}$ transmission coefficients with those for the next highest value of E_i, denoted by $E_{i,1}$. For some value $E = E_{\text{conv}}$, where $E_{\text{conv}} > E_{i,0}$, there will be a convergence between the $E_{i,0}$ and $E_{i,1}$ transmission coefficients. E_{conv} corresponds to an energy where both the energy coefficients for the two wave-packets of initial energies $E_{i,0}$ and $E_{i,1}$ are high in value (for example $E_{\text{conv}} \approx 1.03V_B$ in Fig. 4.7(b)). The tolerance for this convergence was set to 10^{-2}, such that if the absolute difference between the $E_{i,0}$ and $E_{i,1}$ transmission coefficients is less than or equal to the tolerance 10^{-2}, then we consider the curves converged. Then, once convergence has been established, the overlapped profile will consist of the transmission coefficients for $E_{i,0}$ for energies $E < E_{\text{conv}}$, and the transmission coefficients for $E_{i,1}$ for energies $E \geq E_{\text{conv}}$. This procedure is then repeated using $E_{i,1}$ and $E_{i,2}$, and so on until the maximum value of E_i is reached. The total overlapped TDCCWP transmission coefficients can be shown in Fig. 4.8. The TDCCWP transmission coefficients agree well with the TISE results for a wide range of energies, including some below the barrier, indicating that we can obtain energy-resolved quantities using a time-dependent method.

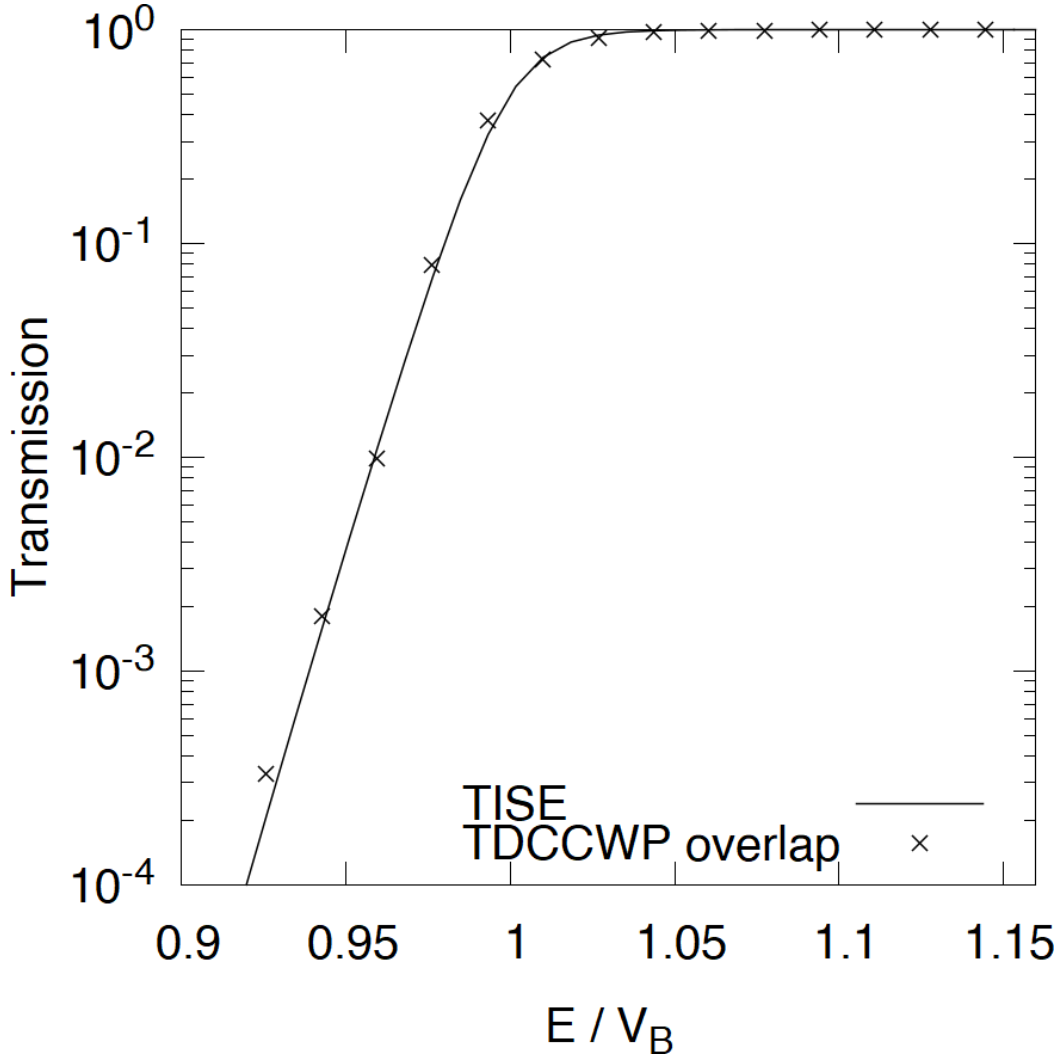

Figure 4.8: Overlapped energy-resolved transmission coefficients for $J = 0$ and the TISE results from using the CCFULL code of Ref. [32] . Overlapping profile generated by linking E_i profiles from Fig. 4.6 with transmission coefficients that have an absolute difference of $\leq 10^{-2}$.

Table 4.2: Model parameters pertaining to the coupled-channels Hamiltonian for the ^{16}O and ^{154}Sm collision, assuming the projectile is spherical and inert and the target has a rotational band. Wood-Saxons and rotational parameters obtained from [54].

Variable	Value	Description
V_{WS}/MeV	165	Wood-Saxons well depth
r_{WS0}/fm	0.95	Wood-Saxons well centre
a_{WS}/fm	1.05	Wood-Saxons well range
ϵ_2/keV	82	Second excited state energy (2^+)
β_2	0.322	Quadrupole deformation parameter
β_4	0.027	Hexadecapole deformation parameter
r_{coup}/fm	1.06	Rotational coupling radius

4.4 Three channel propagation

The following section is a summary of our work in Ref. [53]. As explained in sections 2.2 and 2.2.2, we model the projectile as spherical and inert and the target with a rotational band with the $0^+, 2^+$ and 4^+ states. Introducing three channels means increasing the parameter space of our model to include for the nuclear and Coulomb rotational couplings. The propagation parameters are the same as in the single channel case, shown in Table 4.1.

The propagation of the radial and momentum wave-functions for $E_i = 60$ MeV and $J = 0$ are shown in Figs. 4.9 and 4.10 respectively. Qualitatively we observe a similar absorption behaviour in Fig. 4.9(a) as in Fig. 4.3. We can also see in Fig. 4.9(b) that the 2^+ and 4^+ states penetrate deeper into the barrier. This is because these states are mainly generated via the transfer of flux from the higher momentum states of the 0^+ state in the entrance channel. This can be verified in Fig. 4.10(b), where we observe that the higher momentum 0^+ states convert into the 2^+ and 4^+ states at around $6 - 7$ zs. This is what we expect physically because the strength of the coupling potentials are decreasing for penetration approaching the barrier radius, which is illustrated in Fig. 4.11. This means that the closer the states get to the barrier radius, the more likely it is for excitation to occur, and hence the momentum states in the entrance channel with deeper penetration are more likely to become excited. States that penetrate deeper than the barrier radius are not considered in this explanation, since they are quickly absorbed and thus we cannot deduce their excitation mechanism with respect to penetrability.

Figs. 4.12(a) and 4.12(b) show the expectation energy and wave-function norm over time. For a long time before the nuclei reach the barrier, the norm is conserved with an accuracy of 10^{-14} like in Fig. 4.1(b). The loss of norm of the 0^+ state due to both fusion absorption and nuclear excitation is much larger than 10^{-14}, indicating that we can distinguish between loss of norm due to relevant physical processes

and the loss of norm due to computational error. There is a small loss of average energy due to the absorption. We confirm that there are no more interactions after at least 10 zs because the momentum distribution of the wave-function in Fig. 4.10(c) is completely located in positive momentum and the wave-function norm in Fig. 4.12(b) remains constant. Thus for times after at least 10 zs the comparison between the TDCCWP method and the TISE should yield the same results. The propagation results agree with our expectations.

4.5 Three channel transmission coefficients

The method and analysis is identical for the single channel case described before, and thus they are not repeated here. Figs. 4.13 and 4.14 show the raw and overlapped transmission data for $J = 0$ respectively, and Fig 4.15 shows the overlapped transmission data for $J = 20$ and $J = 30$. Note that the $J = 30$ results in Fig. 4.15(b) are different to the results in Fig. 7(b) published in [53], due to a mistakenly missing divisor of H_- in the absorption of equation (A.30) in the published results. The results in this thesis are produced from the corrected code, and accurately reproduce the transmission coefficients as expected.

4.6 Summary

Overall, we can see that the propagation performs quantitatively well and reproduces the expected transmission coefficient for a wide range of energies around the barrier energy. The transmission coefficients are still determined accurately when the number of excited states is increased, indicating that the method has good scalability. This model is able to calculate absorption cross sections using equation (3.1) and may be useful for interpreting experimental fusion data.

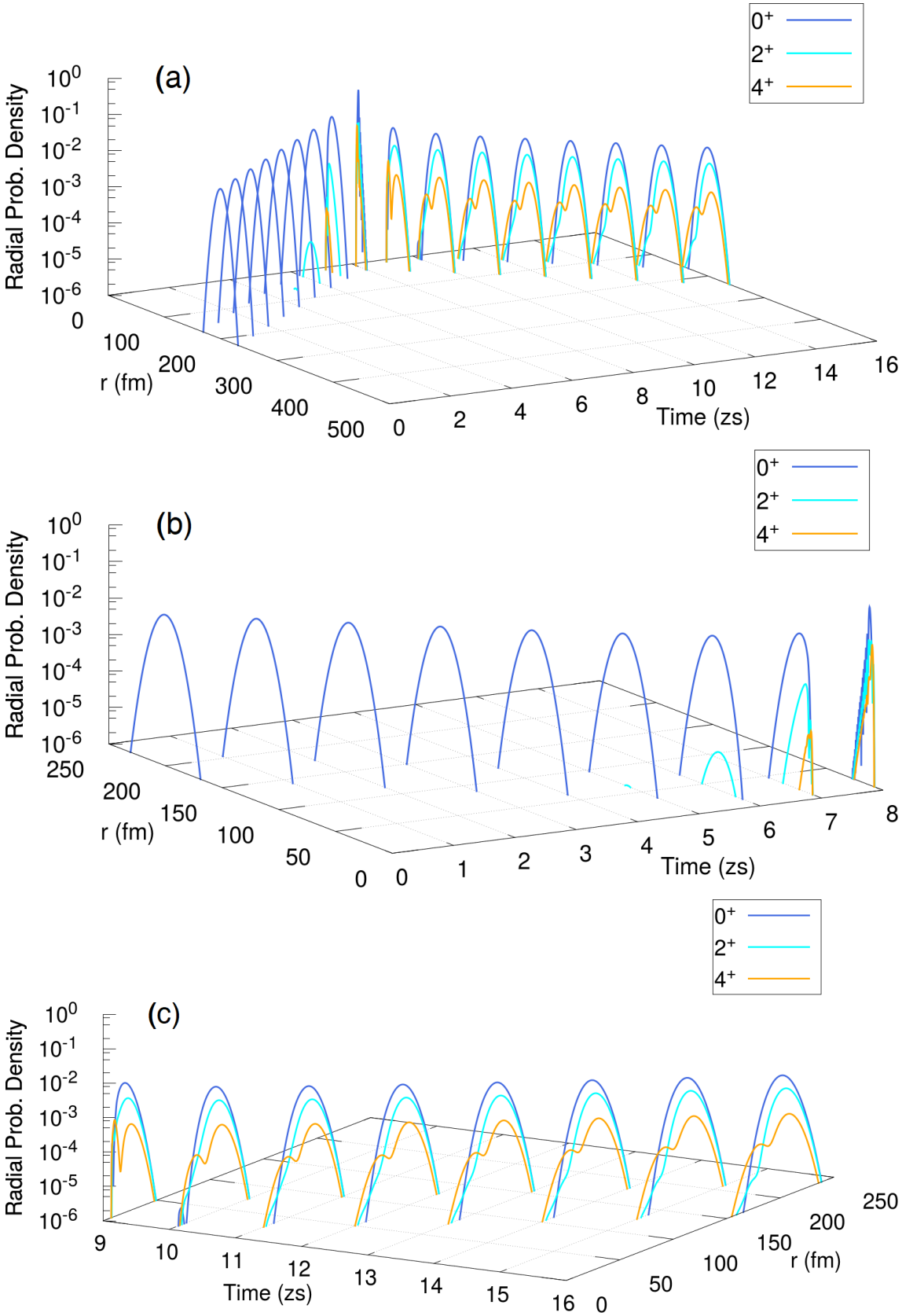

Figure 4.9: Evolution of the radial probability density a) over the whole time period b) from $0-8$ zs (incoming) c) from $9-16$ zs (outgoing), for $J=0$ and $E_i=60$ MeV for the ^{16}O $+^{154}$Sm collision. The blue (dark grey), cyan (light grey) and orange (grey) distributions are the $0^+, 2^+$ and 4^+ states of ^{154}Sm respectively.

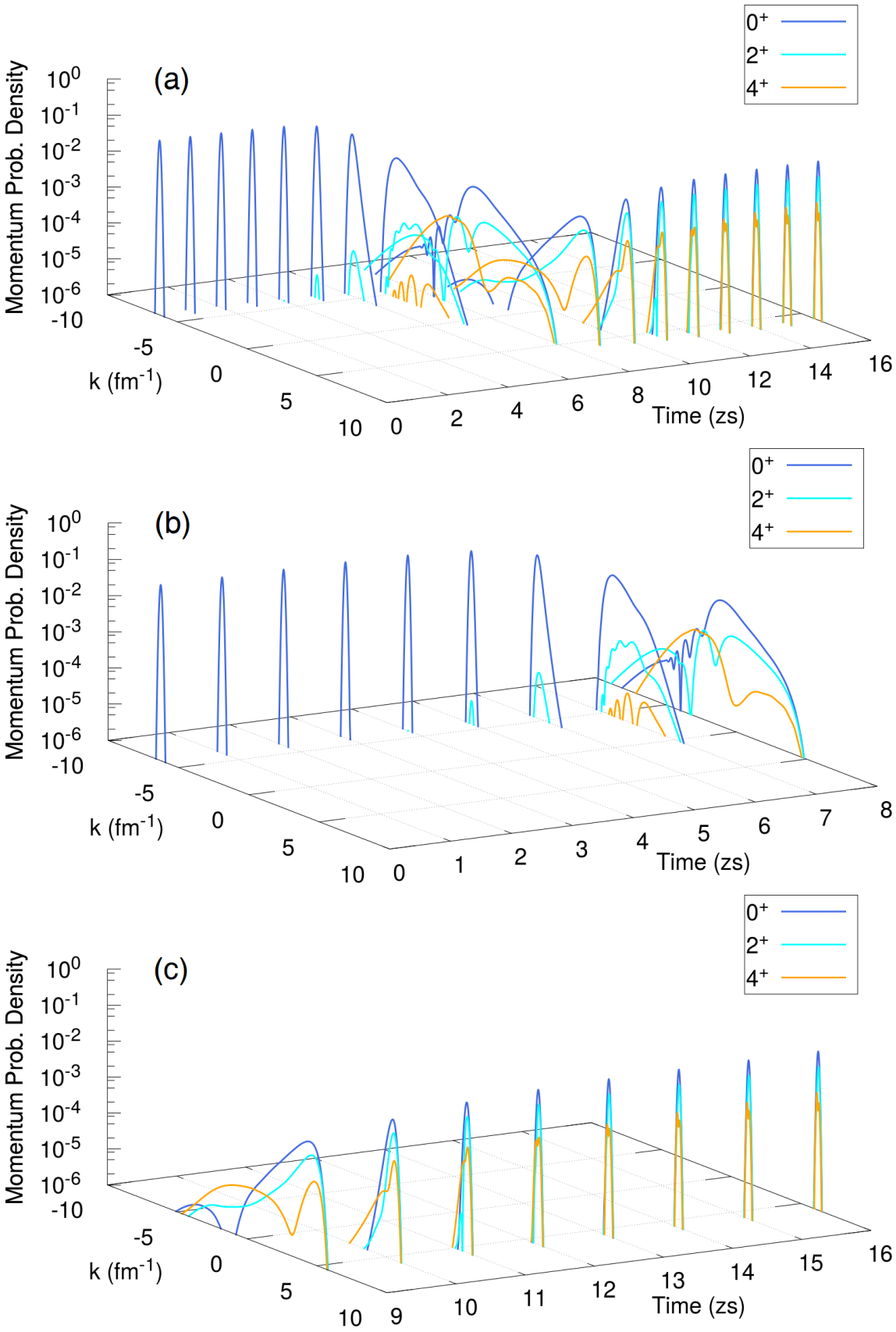

Figure 4.10: The same as Fig. 4.9, but for the momentum probability density.

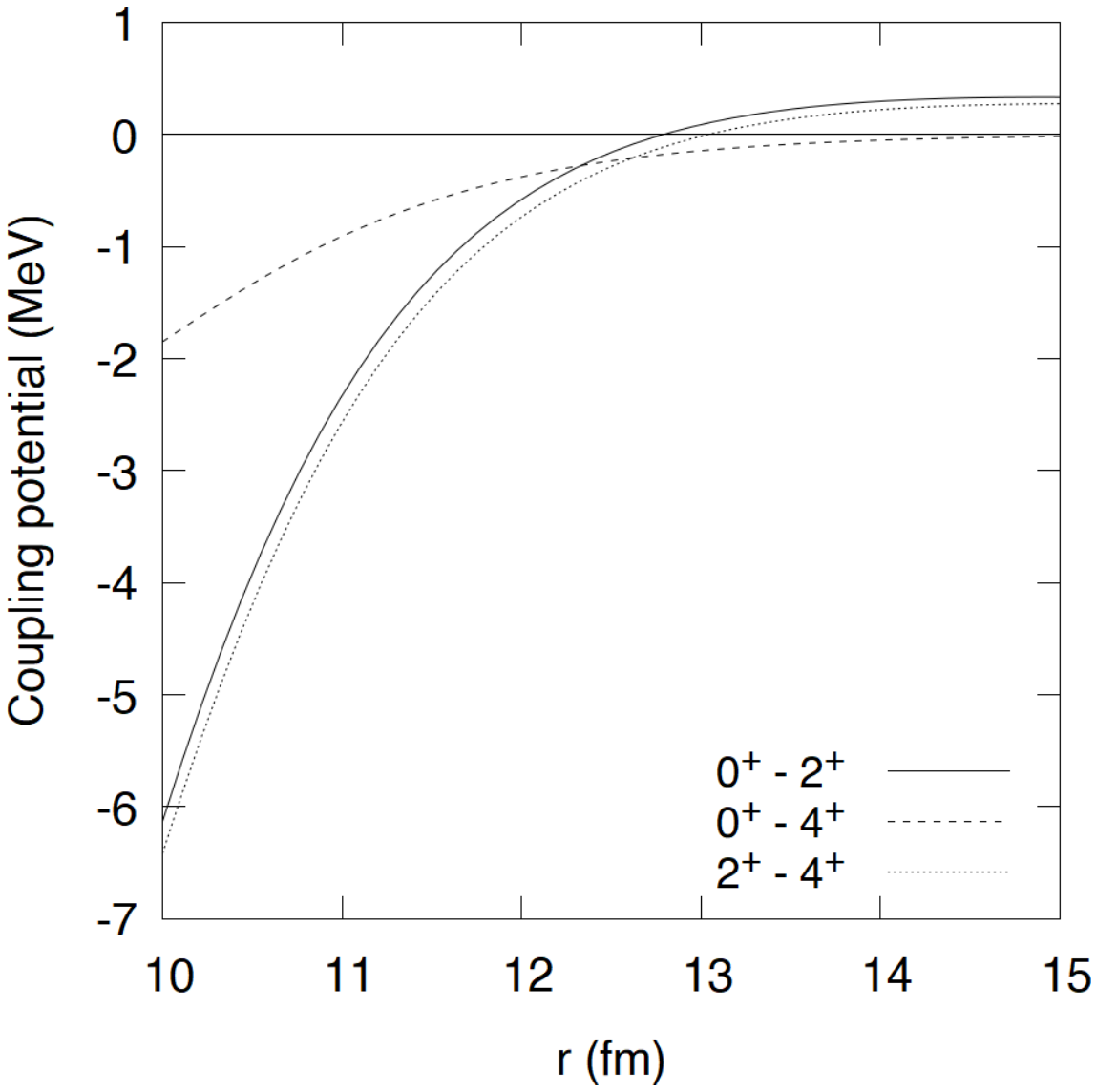

Figure 4.11: Coupling potentials for the ^{16}O + ^{154}Sm system from our parameterisation. Barrier radius for $J = 0$ is equal to 10.81 fm.

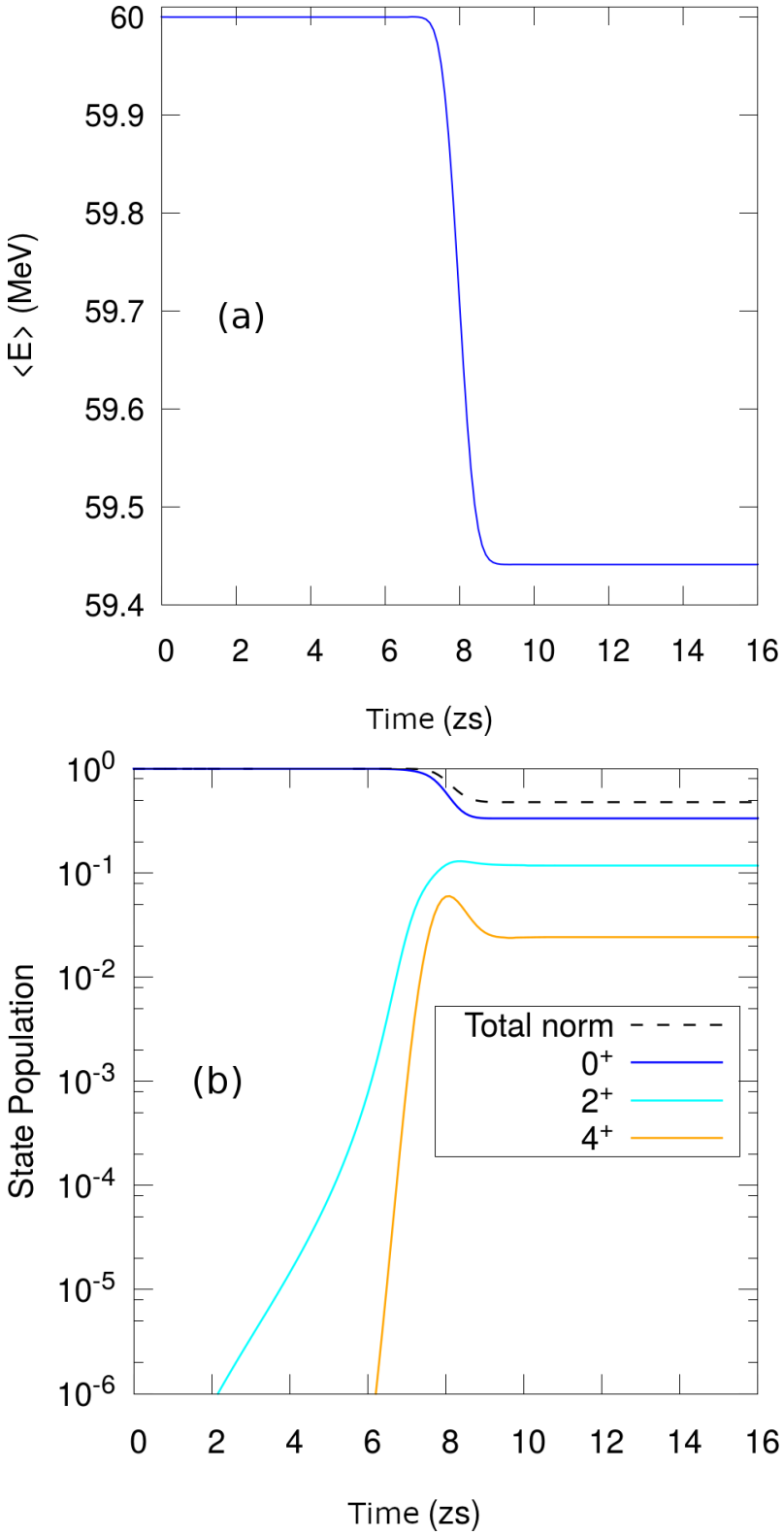

Figure 4.12: Expectation energy and wave-function norm over time for $J = 0$ and $E_i = 60$ MeV. a) Expectation energy over time. Decrease in the expected energy mirrors absorbed norm in Fig. 4.12(b). b) State populations (wave-function norm) over time. The blue (dark grey), cyan (light grey) and orange (grey) lines are the $0^+, 2^+$ and 4^+ state populations of ^{154}Sm respectively, and the black dashed line shows the total state population. Absorption occurs after 6zs, and after $\sim$ 9zs all of the state populations stabilise.

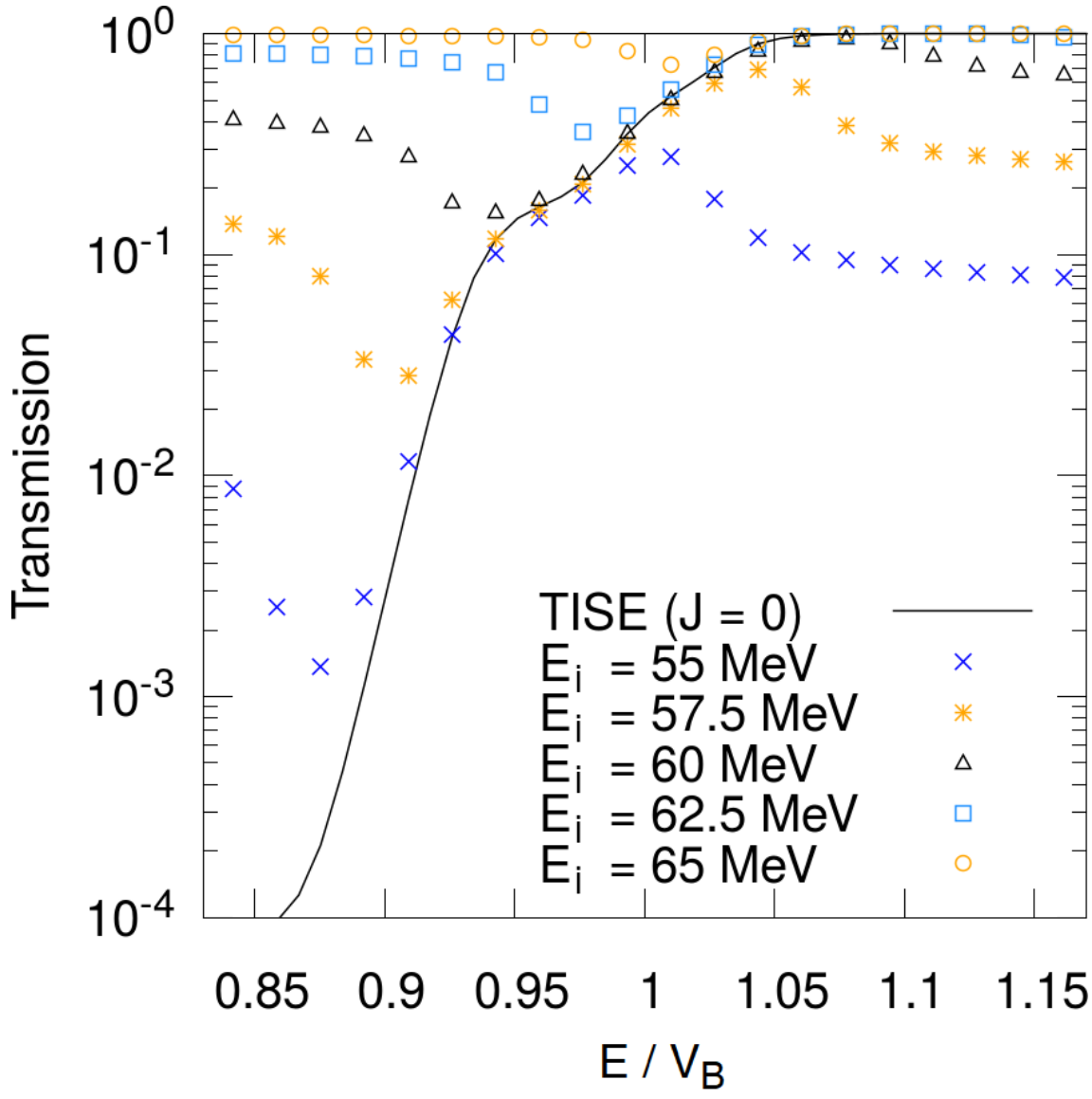

Figure 4.13: (Color online) Energy resolved transmission coefficients using the window operator method for $J = 0$ and the TISE results from using the CCFULL code of Ref. [32]. The profile resulting from the overlap of these E_i profiles are the transmission coefficients (explained in text, shown in Fig. 4.14. Barrier energy for $J = 0$ is equal to 59.41 MeV.

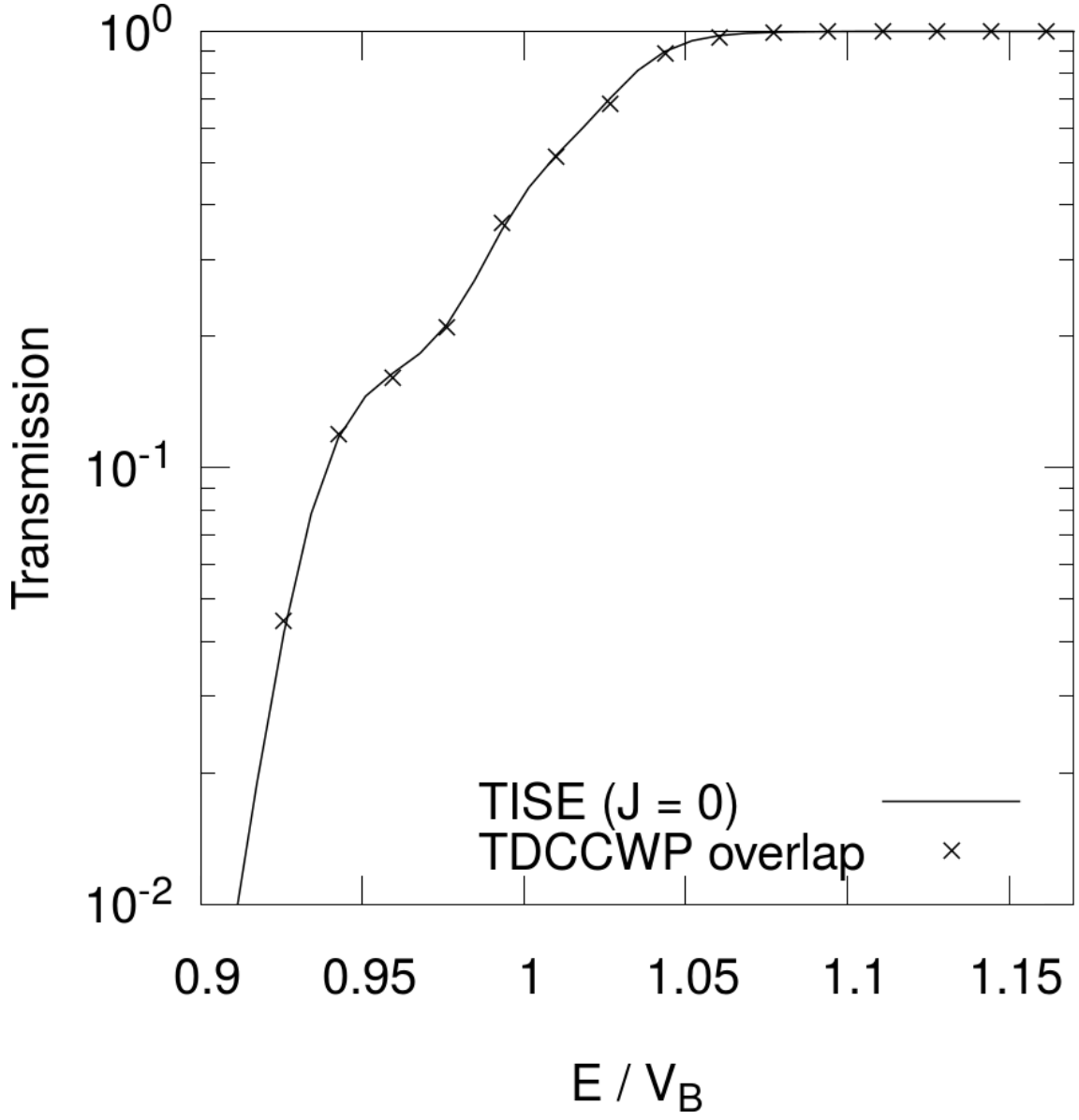

Figure 4.14: Overlapped energy resolved transmission coefficients for $J = 0$ and the TISE results from using the CCFULL code of Ref. [32]. Overlapping profile generated by linking E_i profiles from Fig. 4.13 with transmission coefficients that have an absolute difference of $\leq 10^{-2}$.

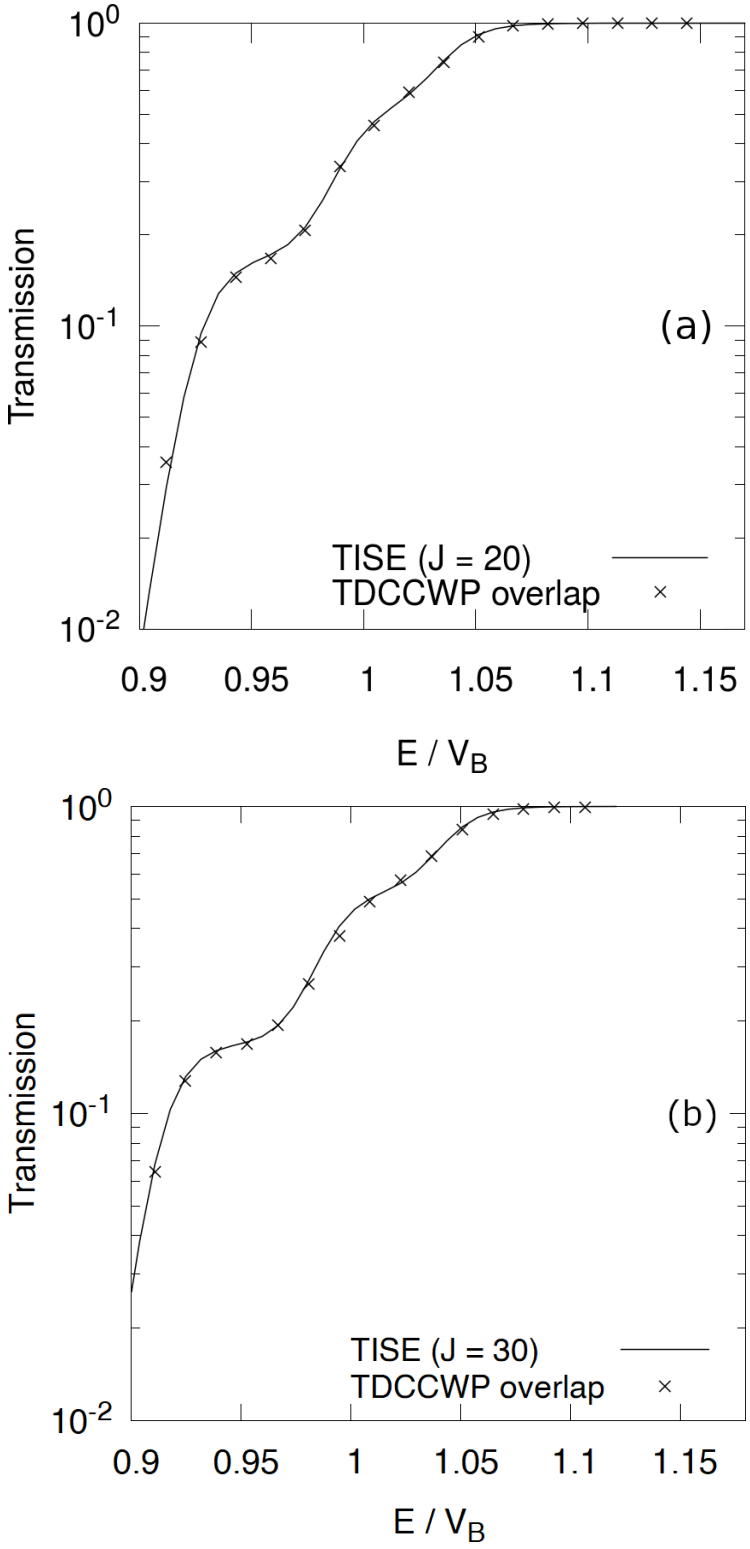

Figure 4.15: Overlapped energy resolved transmission coefficients and the TISE results from using the CCFULL code of Ref. [32]. a) For $J = 20$ (barrier energy V_B equal to 64.69 MeV). b) For $J = 30$ (barrier height V_B equal to 71.38 MeV).

Chapter 5

Differential cross sections and S-matrix for reactive scattering

This chapter details the development of the S-matrix method, which is useful in finding reactive scattering differential cross sections. Whilst the results in the previous chapter are very promising, there is always a concern that no matter how one optimises the parameters of the window operator, the energy resolution may not be as accurate as from, say, a Green's operator. Thus, we have developed an alternative method that uses Green's operators to determine the S-matrix. The S-matrix (or scattering matrix) is the probability amplitude for the transition between initial and final scattering states [12]. The S-matrix is used directly to find the scattering differential cross sections, which can be integrated over to find scattering cross sections [4]. It can also be used to find transmission coefficients used in equation (3.1), as well as for energy resolution in situations where the asymptotic eigenstates of the Hamiltonian are known.

5.1 Scattering differential cross sections

The scattering differential cross sections are a key observable in nuclear reactions, and are ubiquitous in nuclear experiments. We briefly went over the concept of cross sections before in section 1.1, and we will provide a more detailed explanation here. Consider a reaction that results in the emission of nuclei/particles of type b, with a projectile beam intensity of $\mathrm{I_P}$ nuclei/particles per unit area, aimed at a target with n_T nuclei of a specific type A_T. We expect that the rate of emission of nuclei/particles of type b to be proportional to both $\mathrm{I_P}$ and n_T. If the projectile beam intensity increases, then there are more nuclei/particles per unit area and therefore more reactions should occur. If n_T is increased, then we also expect more reactions to occur. The constant of proportionality is the cross section [4]. The differential cross section is a similar concept - it is the constant of proportionality between the rate of emission of nuclei/particles of type b within the solid angle $\mathrm{d}\Omega$,

and the quantities $\mathrm{I_P}$, n_T and $\mathrm{d}\Omega$ [4]. The scattering differential cross section is the differential cross section for nuclei/particles of type b produced by a scattering reaction.

The differential cross section is a relatively intuitive concept to experimentalists. It can be calculated relatively easily because experimentalists measure the rate of emission of nuclei/particles of type b within solid angles, since they place their detectors at angles around the reaction centre. Since the projectile beam intensity is known/controlled, as well as the composition of the target, the differential cross sections can be calculated, and then the cross sections can be found by integrating the determined differential cross sections over the solid angle. In general, the scattering differential cross sections are given by [4]

$$\frac{\mathrm{d}\sigma_{\beta\alpha}(E,\theta,\phi)}{\mathrm{d}\Omega} = \frac{v_\beta}{v_\alpha}|f_{\beta\alpha}(E,\theta,\phi)|^2, \tag{5.1}$$

where Ω is the solid angle, E is the kinetic energy of the radial motion, $f_{\beta\alpha}(E,\theta,\phi)$ is known as the scattering amplitude, and v_γ is the velocity of flux in channel γ. The scattering amplitude is an angular dependent coefficient that relates the scattered wave-function of the relative motion to the radial eigenstates of the asymptotic Hamiltonian [4]. The calculation of the scattering amplitude involves a summation over the total angular momentum J. In order to calculate the differential cross sections, we make some assumptions to simplify the scattering amplitude computations. Firstly, we assume that the direction of the beam is aligned along the z axis. This means that the angular velocity, and therefore the direction of the angular momentum J, is initially confined to the xy plane. The consequence of this is that, at least initially, the magnetic projection number $m_J = 0$, since m_J is the projection of the angular momentum J on the z axis, which is zero if the angular momentum is in the xy plane. Next, if we assume that any spin-orbit interactions are negligible (such as in the iso-centrifugal approximation), then $m_J = 0$ for the entire reaction, and then the differential cross sections will only depend on the polar angle θ since only terms with $m_J = 0$ enter the sum ($m_J = 0$ terms have no ϕ dependence). Consequently, the scattering amplitude for collisions involving charged particles is given by [4]

$$f_{\beta\alpha}(E,\theta,\phi) = f_C(\theta)\delta_{\alpha\beta} + \frac{1}{2ik_{\alpha i}}\sqrt{\frac{v_\alpha}{v_\beta}}\sum_J (2J+1)\exp\left(2\mathrm{i}\sigma_{\alpha,J}\right)\left(S^{SF}_{\beta\alpha}(E,J) - \delta_{\alpha\beta}\right)P_J\left(\cos(\theta)\right), \tag{5.2}$$

where $f_C(\theta)$ is the pure Coulomb point charge (or Rutherford) scattering amplitude, $\delta_{\alpha\beta}$ is the Kronecker delta, $k_{\alpha i}$ is the wave-number of the incident channel α, $\sigma_{\alpha,J}$ are known as the Coulomb phase shifts, $S^{SF}_{\beta\alpha}(E,J)$ are the space-fixed on-shell S-matrix elements (discussed in section 5.2) and $P_J\left(\cos\left(\theta\right)\right)$ are Legendre polynomials. The term on-shell means that the collective radial motion of the nuclei satisfies the

energy-momentum relation [55]. The Coulomb point charge scattering amplitude has the form

$$f_C(\theta) = -\frac{\eta_\alpha}{2k_{\alpha i}\sin^2\left(\frac{\theta}{2}\right)} \exp\left(-i\eta_\alpha \ln\left(\sin^2\left(\frac{\theta}{2}\right)\right) + 2\mathrm{i}\sigma_{\alpha,0}\right), \tag{5.3}$$

where

$$\eta_\alpha = \frac{Z_\mathrm{T} Z_\mathrm{P} \mathrm{e}^2}{4\pi\epsilon_0 \hbar v_\alpha}. \tag{5.4}$$

Note that η_α is known as the Sommerfeld parameter, and it is used to calculate the Coulomb phase shifts, i.e.:

$$\sigma_{\alpha,J} = \arg\left(\Gamma(J+1+\mathrm{i}\eta_\alpha)\right), \tag{5.5}$$

where Γ is the Gamma function. If we are modelling a neutron capture reaction, then $\eta_\alpha = 0$, which means that $\sigma_{\alpha,J} = 0$ from the argument of the Gamma function, and the expression in equation (5.2) reduces to the same expression that is derived for electrically neutral particles [4]. The heart of the calculation of equation (5.2) is the calculation of the S-matrix elements, since all other quantities in equation (5.2) are known parameters of the system.

5.1.1 High energy limit

There is an analytical result to equation (5.2) for when the collision energy is at least several MeV above the largest potential barriers involved in the calculation. In the limit $E \to \infty$, we expect the S-matrix elements to tend to zero. This is because at high collision energies, all barriers preventing fusion are penetrated, and thus there is no reflection at the barrier. Taking the limit of equation (5.2) yields

$$\lim_{E\to\infty} f_{\beta\alpha}(E,\theta,\phi) = f_C(\theta)\delta_{\alpha\beta} - \frac{1}{2ik_{\alpha i}}\sqrt{\frac{v_\alpha}{v_\beta}}\sum_J (2J+1)\exp\left(2\mathrm{i}\sigma_{\alpha,J}\right)\delta_{\alpha\beta}P_J\left(\cos(\theta)\right). \tag{5.6}$$

Clearly, in this limit the inelastic scattering amplitude becomes zero due to the Kronecker deltas, and only elastic scattering is present in equation (5.6). This is a crucial result that can be used to benchmark our time-dependent calculations at high energies, since equation (5.6) only depends on known parameters or quantities of the system. For collision energies several MeV higher than the barrier height, we expect our results of equation (5.2) to match the results from equation (5.6).

In reality, if all the material goes into fusion in this high energy limit, then the scattering amplitudes should become zero for all angles. The out-bound wave-function in this situation is null, and therefore not of the form of a Coulomb wave. Thus, the sum in equation (5.2) diverges from the physically expected result (since equation (5.2) is built on the assumption that the outgoing Coulomb wave exists). Nevertheless, this fictitious benchmark is still a useful way to check the results of our numerical calculation.

5.2 On-shell body-fixed S-matrix elements

Our main goal is to find the S-matrix elements for the body-fixed reference frame, and relate these to the space-fixed frame S-matrix elements. The body-fixed reference frame dynamics are achieved by rotating the three-dimensional dynamics onto the radial coordinate axis. In general, the body-fixed Hamiltonian for the nuclear system is not of the same form as equation (2.8), but in the iso-centrifugal approximation the two Hamiltonians are equivalent [48, 56]. This means that a time propagation of solely the radial wave-function (without any angular folding) yields the body-fixed S-matrix elements that we need. The more general form for the relationship linking the body-fixed S-matrix elements to the space-fixed S-matrix elements is relegated to the future work section since these forms of body-fixed Hamiltonians are relevant when treating the spin-orbit interaction. In our iso-centrifugal case, the relationship between the body-fixed and space-fixed elements is given by [56]

$$S^{SF}_{\beta\alpha}(E,J) = (2J+1)\begin{pmatrix} J & 0 & J \\ 0 & 0 & 0 \end{pmatrix}\begin{pmatrix} J & I_{\beta f} & J \\ 0 & 0 & 0 \end{pmatrix} S^{BF}_{\beta\alpha}(E,J), \tag{5.7}$$

where $S^{BF}_{\beta\alpha}(E,J)$ are the on-shell body-fixed S-matrix elements, which can be expressed as [57]

$$S^{BF}_{\beta\alpha}(E,J) = \langle \chi^{-}_{\beta f,E,J} | \chi^{+}_{\alpha i,E,J} \rangle \,, \tag{5.8}$$

where $|\chi_{\gamma,E,J}\rangle$ are the energy resolved asymptotic states of the body-fixed Hamiltonian $\hat{H}_{\mathrm{CRM}}$ of equation (2.8) for excitation channel γ with angular momentum J, and +/- indicates in/out-bound radial states (i.e.: the inwards direction is towards $r = 0$, and outwards is away). The energies of the initial and final states are the same, which is a direct consequence of the nuclei satisfying the energy-momentum relation as discussed earlier [55]. Consider the initial state in entrance channel α for our time propagation $|\psi^{+}_{\alpha i,J}(t_i)\rangle$, which is a superposition of in-bound body-fixed asymptotic states. We can extract the asymptotic state from the initial state using an energy projection operator

$$|\chi^{+}_{\alpha i,E,J}\rangle = \frac{1}{\Lambda_{\alpha i,E,J}}\delta(\hat{H}-E)\,|\psi^{+}_{\alpha i,J}(t_i)\rangle\,, \tag{5.9}$$

where

$$\Lambda_{\alpha i,E,J} = \langle\chi^{+}_{\alpha i,E,J}|\psi^{+}_{\alpha i,J}(t_i)\rangle\,, \tag{5.10}$$

and similarly for $|\chi^{-}_{\beta f,E,J}\rangle$ via some out-bound final state $|\psi^{-}_{\beta f,J}\rangle$. Substitution into (5.8) yields the result [57]

$$\begin{aligned}
S^{BF}_{\beta\alpha}(E,J) &= \frac{1}{\Lambda^{*}_{\beta f,E,J}\Lambda_{\alpha i,E,J}}\,\langle\psi^{-}_{\beta f,J}|\,(\delta(\hat{H}-E))^2\,|\psi^{+}_{\alpha i,J}(t_i)\rangle \\
&= \frac{\mathrm{i}}{2\pi\Lambda^{*}_{\beta f,E,J}\Lambda_{\alpha i,E,J}}\,\langle\psi^{-}_{\beta f,J}|\,\hat{G}^{+}(E)+\hat{G}^{-}(E)\,|\psi^{+}_{\alpha i,J}(t_i)\rangle \\
&= \frac{\mathrm{i}}{2\pi\Lambda^{*}_{\beta f,E,J}\Lambda_{\alpha i,E,J}}\,\langle\psi^{-}_{\beta f,J}|\,\hat{G}^{+}(E)\,|\psi^{+}_{\alpha i,J}(t_i)\rangle \\
&= \frac{1}{2\pi\hbar\Lambda^{*}_{\beta f,E,J}\Lambda_{\alpha i,E,J}}\int_{-\infty}^{\infty}\mathrm{d}t\exp\left(\frac{\mathrm{i}E(t-t_i)}{\hbar}\right)\langle\psi^{-}_{\beta f,J}|\,\hat{U}(t,t_i)\,|\psi^{+}_{\alpha i,J}(t_i)\rangle \\
&= \frac{1}{2\pi\hbar\Lambda^{*}_{\beta f,E,J}\Lambda_{\alpha i,E,J}}\int_{-\infty}^{\infty}\mathrm{d}t\exp\left(\frac{\mathrm{i}E(t-t_i)}{\hbar}\right)\langle\psi^{-}_{\beta f,J}|\psi^{+}_{\alpha i,J}(t)\rangle\,.
\end{aligned} \tag{5.11}$$

Here we have replaced the two delta functions with a single $G^{+}(E)$ Green's operator, and performed a Fourier transform into the time domain. The effect of the $G^{-}(E)$ Green's operator is omitted since the initial state $|\psi^{+}_{\alpha i,J}(t_i)\rangle$ consists only of inbound states, and thus $G^{-}(E)\,|\psi^{+}_{\alpha i,J}(t_i)\rangle = 0$. This expression from reference [57] is equivalent to the result derived by Tannor and Weeks in reference [58], with the practical advantage of avoiding a numerical implementation of the Møller operators, since the initial and final states are defined as asymptotic states already. We choose the final states $|\psi^{-}_{\beta f,J}\rangle$ so that their radial wave-functions are of the form

$$\langle r|\psi^{-}_{\beta f,J}\rangle = \exp\left(\frac{-(r-r_f)^2}{2\sigma_f^2}\right)\times\,\langle r|\chi^{-}_{\beta f,E_f,J}\rangle\,, \tag{5.12}$$

where E_f is an arbitrarily chosen final energy, taken to be equal to E (henceforth, the terms E and E_f will be used interchangeably, with a preference for E). Thus for the Hamiltonian in equation (2.8) the final radial wave-functions are the out-bound energy resolved asymptotic Coulomb wave-functions, modulated by a Gaussian envelope. The incident wave has a similar form

$$\langle r|\psi^{+}_{\alpha i,J}(t_i)\rangle = \exp\left(\frac{-(r-r_i)^2}{2\sigma_i^2}\right) \times \langle r|\chi^{+}_{\alpha i,E_i,J}\rangle\,, \tag{5.13}$$

where r_i, σ_i and E_i are the same as the parameters used in equation (2.17). Our novel choice of the initial and final states in equation (5.12) have been found to reduce the error in calculating the transmission coefficients from the S-matrix method. The Gaussian envelope function in equation (5.12) is used to converge the time integral in equation (5.11), since with this choice of wave-function $|\psi_{\alpha i,J}(t)\rangle$ will eventually travel past the final states, and thus a finite upper limit to the integral can be imposed. It should be noted that the number of grid points must increase from calculations in the previous chapter, since despite all the countermeasures employed to make integrals smoother they are quite oscillatory in nature. This also requires one to use more sophisticated (but still elementary) integration methods such as the Simpson's rule.

Time propagation and matrix inverse methods such as the window operator method are accurate, but are also counter-synergistic because the relatively large grid sizes needed for accurate time propagation make the matrix inverse calculations more time consuming. Using a time-dependent S-matrix calculation such as (5.11) is much more efficient in terms of computation time. It has a similar (high) level of accuracy, it can generate results faster for a fixed set of energies, and it foregoes matrix inverse calculations on the large grid which take a significant amount of computation time. However, the S-matrix method is only appropriate for systems where the asymptotic form of the final scattering states is known and calculable, which thankfully is the case for nuclear reactions.

A significant strength of the proposed S-matrix method is the ability to use any final state to extract the S-matrix elements, as opposed to a final state that comes from the time propagated state. The optimal choice of the envelope widths σ_f and σ_i is vital in order to generate accurate calculations, and the choices sufficient for accurate calculations for one set of input parameters are not necessarily sufficient for other inputs. As a rough guide, the initial state should be broad in momentum to minimise the number of time propagations needed for good overlap between adjacent E_i values, and the final states should be narrow in momentum in order to accurately determine the energy coefficients and the energy overlap.

5.2.1 Transmission coefficients from the S-matrix

We can find the reflection coefficients using the S-matrix method simply by summing the mod squared of the S-matrix elements over the final channels. Then, the transmission can be found using

$$\mathcal{T}_\alpha(E,J) = 1 - \mathcal{R}_\alpha(E,J) \tag{5.14}$$
$$= 1 - \sum_\beta \left| S^{BF}_{\beta\alpha}(E,J) \right|^2. \tag{5.15}$$

Having transmission data from other methods is very useful to compare the S-matrix data to. When there is no data to compare to, one ought to find the energy coefficients of the initial and final states used in equation (5.11), in order to best guide the judgement of how to consolidate the results for varying initial energies E_i. We will discover in the next chapter that there is a pattern for which energy components are convergent from each wave-packet of initial energy E_i.

5.3 Differential cross sections including spin-orbit interaction

There have been bodies of work concerning the interaction between the spin of the target with the orbital angular momentum, through mechanisms such as the Coriolis interaction. This have been used to study collisions between di-atoms and atoms [56].

The Coriolis effect is expected to have less of an impact on high J collisions, because the centrifugal barrier repels the two nuclei away from the spin-orbit interacting potentials (as explained previously in section 2.3). However, the spin-orbit interaction does depend on other parameters of the colliding system and undoubtedly is relevant. A reasonable extension of this work would be to model a spin-orbit calculation of the differential cross sections for differing J values, and compare it to those generated from equation (5.2). This will involve including Coriolis terms into equation (2.8), as well as extending the summation in equation (5.2) to include terms other than $m_J = 0$. The spin-orbit calculation is very involved, and takes a relatively long computation time even for the time-independent approach. This spin-orbit method is expanded upon in the future work section.

Whilst the iso-centrifugal approximation is indeed an unjustified simplification if one wants to calculate the differential cross section accurately for all angles, it is predicted to be a powerful approximation for the forward angles (i.e.: $\theta \sim 0$), since the contributions to forward angles occur at high J values where the approximation holds.

Chapter 6

TDCCWP S-matrix results

6.1 Updated model parameters

Since the integrals over time in equation (5.11) are relatively oscillatory in nature, it is necessary to increase the number of grid points and to decrease the parameter $r_{\max}$ to ensure a better point density for these integral calculations, which means that r_i must also be adjusted to properly contain the wave-packet within the numerical grid. The wave-packet width can be decreased from previously using this new and improved point density to afford more overlap between results from wave-packets of adjacent E_i values. The changes to the Fourier grid parameters are shown in Table 6.1.

Table 6.1: Updated Table 4.1 Fourier grid model parameters. Includes the r_f and σ_f parameters for the final states as described in equation (5.12).

Variable	Value	Description
NGP	3200	No. of grid points in the Fourier grid
$r_{\max}$/fm	350	Maximum r in Fourier grid
r_i/fm	150	Initial position of wave-packet
σ_i/fm	3	Width parameter of initial wave-packet
r_f/fm	120	Position of final states
σ_f/fm	10	Width parameter of final states

6.2 Investigating the $J = 0$ propagation of the S-matrix

We will begin by investigating how our calculation of equation (5.11) fares during the propagation of the wave-function. During the propagation, there are several aspects that we expect to see, namely:

1. The product $\left\langle \psi^-_{\beta f,J} \middle| \psi_{\alpha i,J}(t) \right\rangle$ should be zero whilst $|\psi_{\alpha i,J}(t)\rangle$ is incoming, and finite when it is outgoing.
2. Since $\left|\psi^-_{\beta f,J}\right\rangle$ is radially modulated, the product $\left\langle \psi^-_{\beta f,J} \middle| \psi_{\alpha i,J}(t) \right\rangle$ for larger times should tend to zero.
3. The overall integral of the products over time should converge to a finite value.

For the first aspect, the product $\left\langle \psi^-_{\beta f,J} \middle| \psi_{\alpha i,J}(t) \right\rangle$ is not able to be calculated whilst $|\psi_{\alpha i,J}(t)\rangle$ is incoming in our simulation, since the integral is highly oscillatory across space as expected from the expression. Analytically, this integral is zero, however since we are using a finite grid method it is impossible for any sensible number of grid points to calculate a zero for the integral. Thus, we only start integrating for times where the wave-function is outgoing.

A necessary but insufficient criterion for an outgoing wave in our simulation is when the average wave-number of the propagated wave is greater than zero. This is not sufficient to determine that the entire wave is an outgoing wave, since not all the components of the wave-packet reflect off the Coulomb barrier at the same time. Suppose we start integrating the S-matrix the moment after the average wave-number becomes positive. For some time before the average wave-number is greater than zero (and therefore before we start counting the integrand), there are components of the wave that have reflected that may not be counted. Therefore, we ensure that the final states are far away enough from the barrier, so that the earliest reflected components are counted when calculating the S-matrix elements. This justifies our choice of final state position in Table 6.1.

Fortunately, once the waves are outgoing, we do not have to deal with highly oscillatory integrals and the remaining aspects listed above are testable. We will test these aspects using the elastic (0^+) scattering data. To that end, we define the following expressions

$$I_2(E,t) = \int_{t_i}^{t} \mathrm{d}t' \exp\left(\frac{\mathrm{i}E(t'-t_i)}{\hbar}\right) \int_{r_{\min}}^{r_{\max}} \mathrm{d}r I_1(E,r,t'), \tag{6.1}$$

where

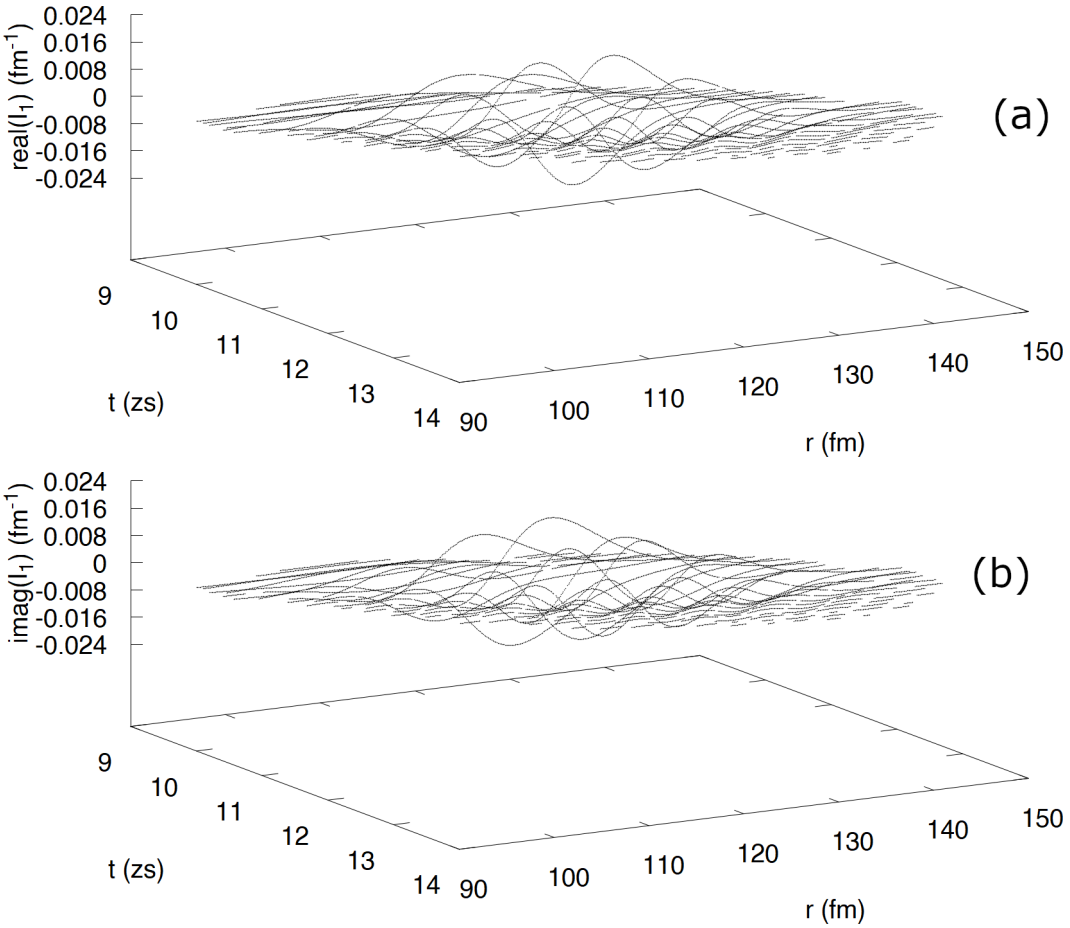

Figure 6.1: a) Real and b) imaginary parts of the integrand quantity $I_1(E, r, t)$ for $E = E_i = 60$ MeV and $J = 0$.

$$I_1(E, r, t) = \left\langle \psi^-_{\alpha f,J} \middle| r \right\rangle \langle r | \psi_{\alpha i,J}(t) \rangle \,. \tag{6.2}$$

$I_1(E, r, t)$ is the elastic product, and intends to test the second aspect. $I_2(E, t)$ folds $I_1(E, r, t')$ over space and up to time t, and intends to test the third. One may wonder why we do not simply fold over time first and then space when calculating I_2, which will allow one to save computation time by not have to perform a radial integration at every time step. The reason is simple - folding over time first means the new integrand over space becomes very highly oscillatory. These two expressions are the building blocks for the computation of the elastic S-matrix elements in equation (5.11).

The 3D plots of $I_1(E, r, t)$ are shown in Fig. 6.1. We can see for times $t \approx 9$ zs and $t \approx 14$ zs that the integrand I_1 is equal to zero, and thus we have effectively contained the information using the radially modulated final state $\left|\psi^-_{\alpha f,J}\right\rangle$. $I_1(E, r, t)$ for times earlier than 9 zs are not shown due to large rendering times and decreased clarity of the results, but for those times $I_1(E, r, t)$ is also equal to zero. Qualitatively, we can also see that for times between 9 and 14 zs, the folding along the radial direction

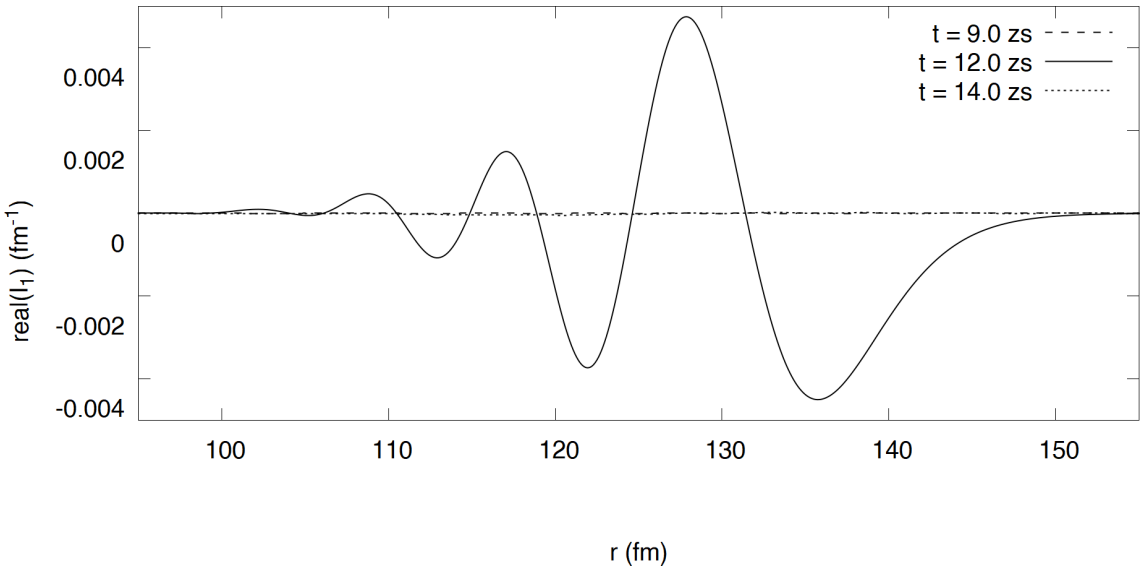

Figure 6.2: Real part of $I_1(E, r, t)$ for $t = 9, 12, 14$ zs. The imaginary part of $I_1(E, r, t)$ shows similar features and smoothness.

is very achievable with a method such as the Simpson's rule, since the oscillations along this direction are tame. This is made clearer in Fig. 6.2, which shows the real part of $I_1(E, r, t)$ for $t = 12$ zs. Evidently from Fig. 6.1, folding over time and then space as suggested earlier will create highly oscillatory integrals that are not calculable using our grid parameters and methods.

The value of $I_2(E, t)$ converges after a long time. This is illustrated in Fig. 6.3, which shows that the real and imaginary parts of $I_2(E, t)$ for $E = 60$ MeV converge for large times. All the aspects to test the propagation have been verified to be true, and thus the propagation is qualitatively successful. Fig. 6.4 shows that the integrals $I_2(E, t)$ for energies far away from $E_i = 60$ MeV do not converge to large integral values. This causes the same type of error that the window operator produced, and thus calls for the same solution - we must propagate over a set of E_i values in order to represent the reaction properly. For each J value, we choose six energies in steps of 1 MeV, with the maximum energy considered being $\max(E_i) = \text{ceiling}(V_B(J))$. So for $J = 0$, $E_i = \{55, 56, 57, 58, 59, 60\}$ MeV.

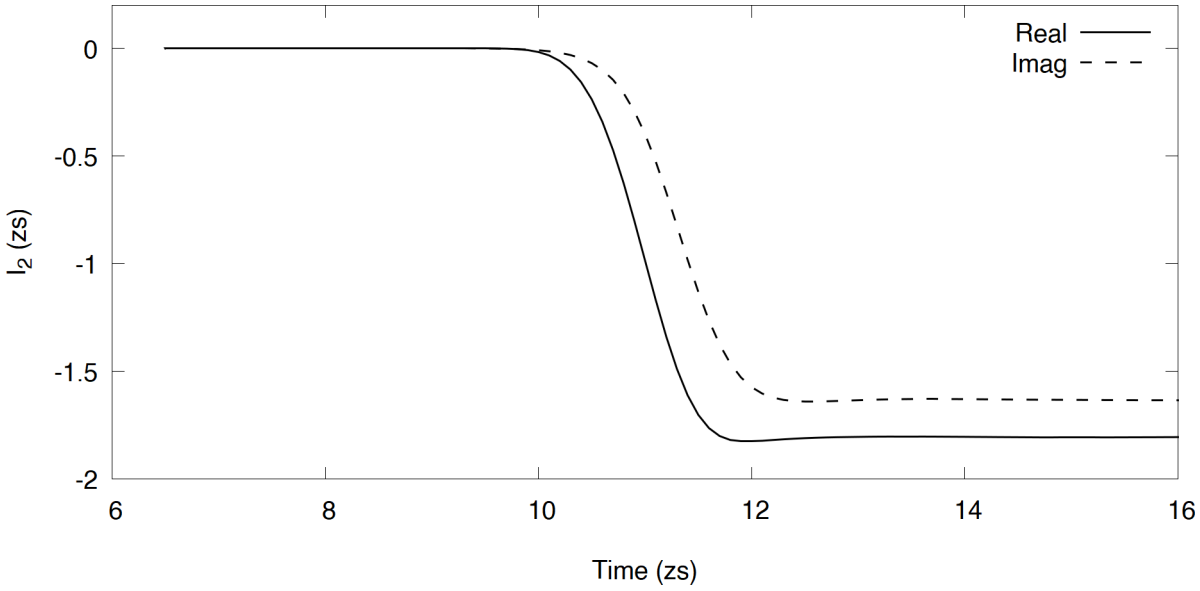

Figure 6.3: Real and imaginary parts of the integral $I_2(t)$ for varying time, and $E = E_i = 60$ MeV and $J = 0$. Convergence of the integral is achieved after $t \approx 13zs$.

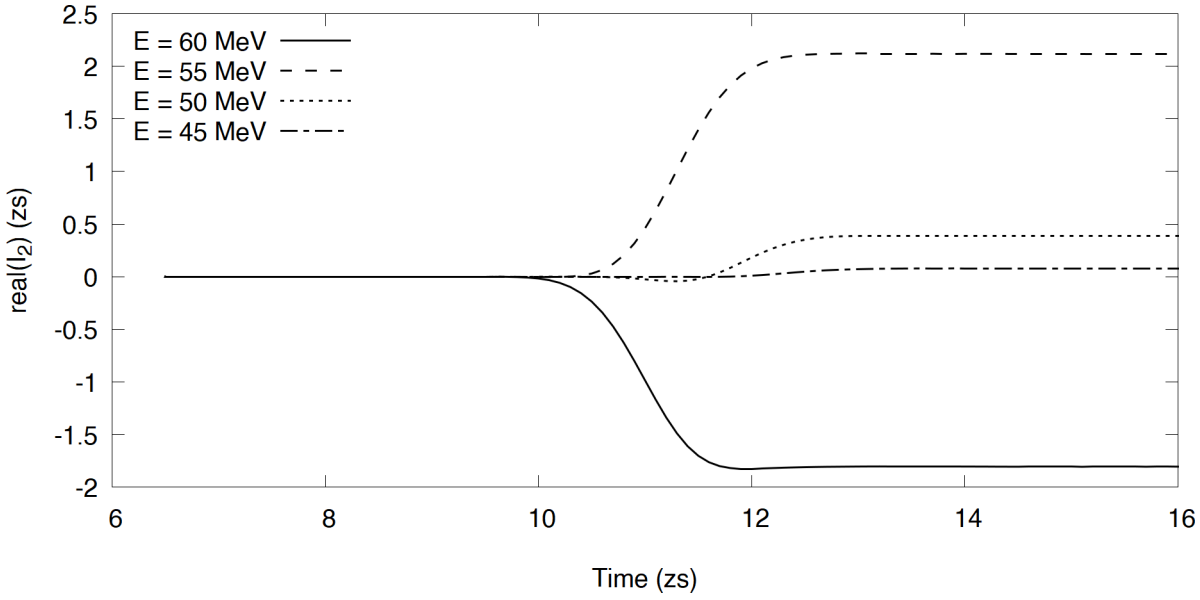

Figure 6.4: Real part of the integral $I_2(t)$ for varying time and E, for $E_i = 60$ MeV and $J = 0$. As E is decreased, the value of the integral decreases, which can become a source of error for the method like it was for the window operator. The imaginary parts follow a similar trend.

6.3 Transmission coefficients from the S-matrix

After all six propagations, the S-matrix data is used to calculate a transmission coefficient via equation (5.15), shown in Fig. 6.5. Unlike the transmission from the window operator, for the energies considered the transmission curves all behave similarly to one another as well as to the expected result. As energy decreases, the deviation between each curve becomes noticeable, but for high energies every curve successfully replicates the high transmission behaviour. This allows for more propagations to be done for energies below the barrier, without sacrificing the higher energy behaviour. Also, with this method one can use a significantly higher energy point density without impeding calculations, since no matrix inverses are invoked on our now much larger grid. Using matrix inverses with a window operator method to calculate energy resolved states would be somewhat unfeasible on our new grid. Like before, we can fit the E_i curves to the CCFULL data, which is shown in Fig. 6.6. This produces similar results to the window operator method, and allows us to describe transmission at energies below the barrier.

The process to overlap the transmission coefficients of varying E_i is remarkably consistent across all J values, but it is slightly different to the procedure described in chapter 4. We have found that the first E_i value agrees with the TISE transmission best up to 0.5 MeV above its value, the second agrees best for energies $0-1$ MeV above its value, the third for energies $0.5-1.5$ MeV above, the forth $1-2$ MeV above, the fifth $1.5-2.5$ MeV above, and the sixth for 2 MeV above its value and beyond. This pattern is the same for all J values, which is somewhat expected giving how we have systematised our time propagation and calculations.

What may be surprising is that the energy ranges where the curves agree are all above the E_i values. We found that the expectation energy for the final states $\left|\psi^{-}_{\beta f,J}\right\rangle$ is roughly equal to the energy E, and thus does not affect this skewing of these energy ranges. For our choice of $|\psi_{\alpha i,J}\rangle$, the expectation energy is larger than the energy E_i, thus S-matrix elements for energies above E_i are expected to be calculated better than those below.

6.4 The choice of final state

We previously justified the choice of using equations (5.13) and (5.12) for the initial and final wave-functions respectively, by saying the results are more accurate compared to using a Gaussian wave-packet with a similar for to the initial wave-function used in chapter 4. This is shown in Fig. 6.7, which features the transmission coefficients via the S-matrix elements for initial energy $E_i = 55$ MeV for two cases: one where the initial and final waves are boosted Gaussian waves (like what was done in chapter 4), and one where both the initial and final wave-functions are of the form of equations (5.13) and (5.12) respectively. As we can see, using two boosted Gaussian wave-functions produces poor convergence with the TISE at low energies,

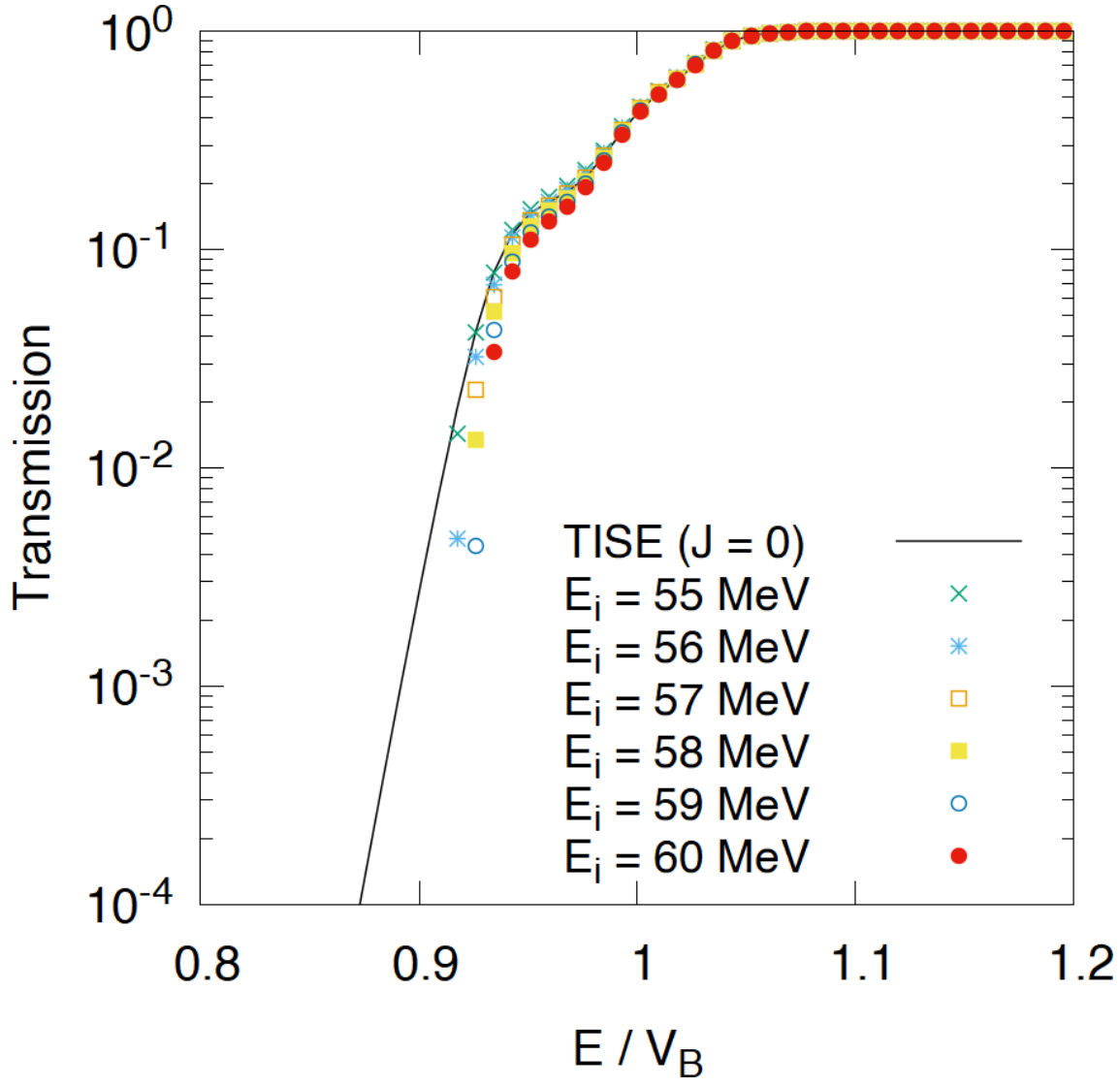

Figure 6.5: Energy resolved transmission coefficients for varying E_i and $J = 0$. Barrier height for $J = 0$ is equal to 59.41 MeV

.

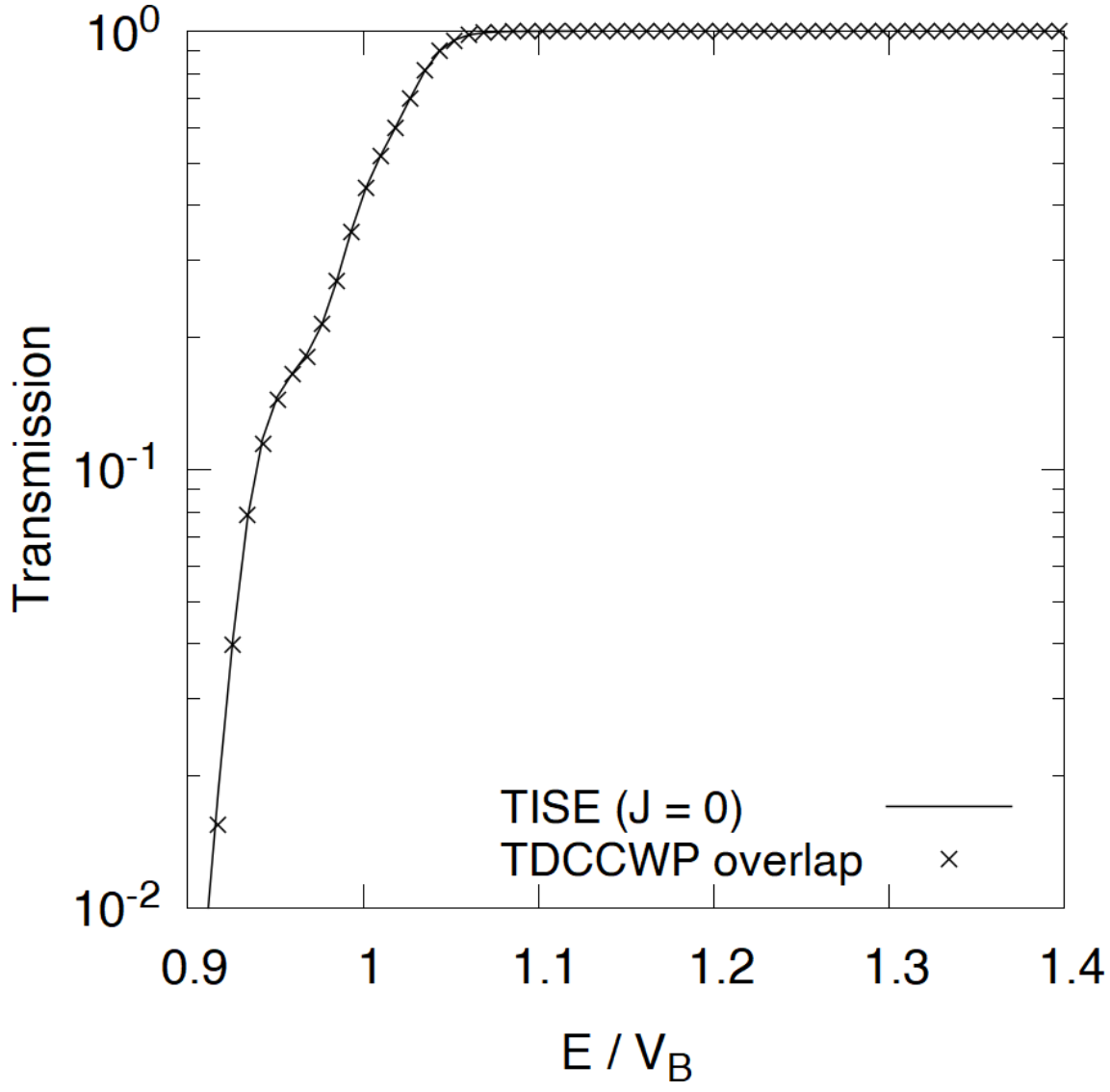

Figure 6.6: Overlapped transmission generated from the data in Fig. 6.5, which is compared to data from the CCFULL code from ref. [32].

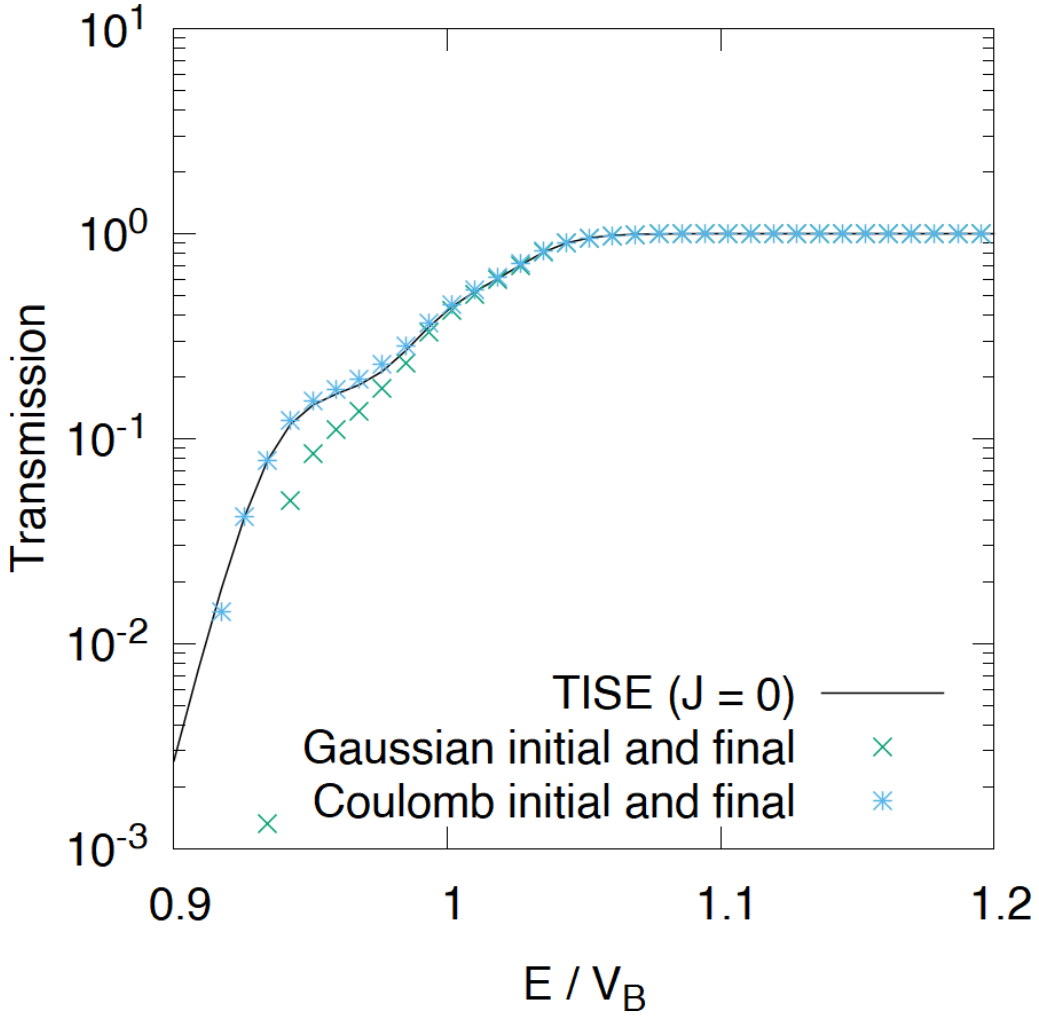

Figure 6.7: Transmission coefficients for initial energy $E_i = 55$ MeV for the two cases of initial and final wave-functions explained in the text. Using two boosted Gaussian wave-functions like equation (2.17) provides poor convergence to the TISE at low energies, whilst using two modulated Coulomb initial and final wave-functions (equations (5.13) and (5.12) respectively) provides significantly better convergence.

and using two modulated Coulomb wave-functions produces the best convergence.

6.5 Low energy coefficients

Our findings show that we can set up a simple procedure where one can lower the initial energy E_i, and continue to propagate into lower energies to find the S-matrix elements. Sadly, whilst the time propagation is still stable for energies far below the barrier and the calculations of integrals $I_1(E, r, t)$ and $I_2(E, t)$ are still reliable, this simple procedure cannot be carried out for energies far below the barrier. This is shown in Fig. 6.8, where decreasing the wave-packet initial energy does not produce accurate transmission results. The size of the error for these values is much larger than the accuracy of the time propagation, which at this point has almost zero transmission and only reflection.

It is absolutely vital to calculate low energy S-matrix elements, since the sum in equation (5.2) to calculate the scattering amplitude at any energy involves contributions from all J values. For example, in order to calculate the differential cross sections for $E = 60$ MeV, we need to know the S-matrix elements for all J at 60 MeV. Consider $J = 30$, which has a barrier of 71.38 MeV. At $E = 60$ MeV the amount of scattered material for $J = 30$ is large, and thus this J value contributes a substantial amount to the scattering differential cross section at this energy.

One way to try and address the lowest of energies is to extrapolate. Whilst this is not generally advised, we can use the fact that when $E \to 0$, only elastic scattering should be present, and the reflection coefficient should tend to unity. This is because the nuclei are far away from both the barrier and the interaction potentials that excite samarium into higher rotational states. Mathematically, this means that the complex radii of the S-matrix elements $\left|S^{BF}_{\beta\alpha}(E, J)\right|$ tends to unity for elastic scattering and zero for inelastic. We also know that as we decrease the energy from V_B, there must be a point along each of the S-matrix complex radii curves as a function of energy where for elastic scattering the curve has a positive gradient, and for inelastic scattering the curve has a negative gradient.

We can see on Fig. 6.9 that for $E_i = 55$ MeV and $J = 0$, between $E \approx 0.7V_B$ and $E \approx 0.8V_B$ the elastic and inelastic 4^+ complex radii gradients are clearly behaving like we expect. This means that we can make a more promising extrapolation using both the $E \to 0$ behaviour and these gradients. The behaviour in Fig. 6.9 for $E/V_B < 0.65$ is unphysical, and is due to the numerically small Green's operator integrals from the time propagation shown in Fig. 6.4.

The sign of the gradient of these S-matrix elements around $E \approx 0.8V_B$ and $E \approx 0.9V_B$ is conserved as one propagates into lower initial energies, as shown in Fig. 6.10 for the final spin state 0^+. Whilst the S-matrix elements no longer quantitatively match the transmission coefficients as E_i decreases (see Fig. 6.8), the fact that the sign of the gradient does not change for decreasing E and E_i supports the logic that we can use an extrapolation method with the gradients for the lowest E_i in the range $0.7V_B \leq E \leq 0.9V_B$. This is also true for the inelastic reflection probabilities in Fig. 6.11.

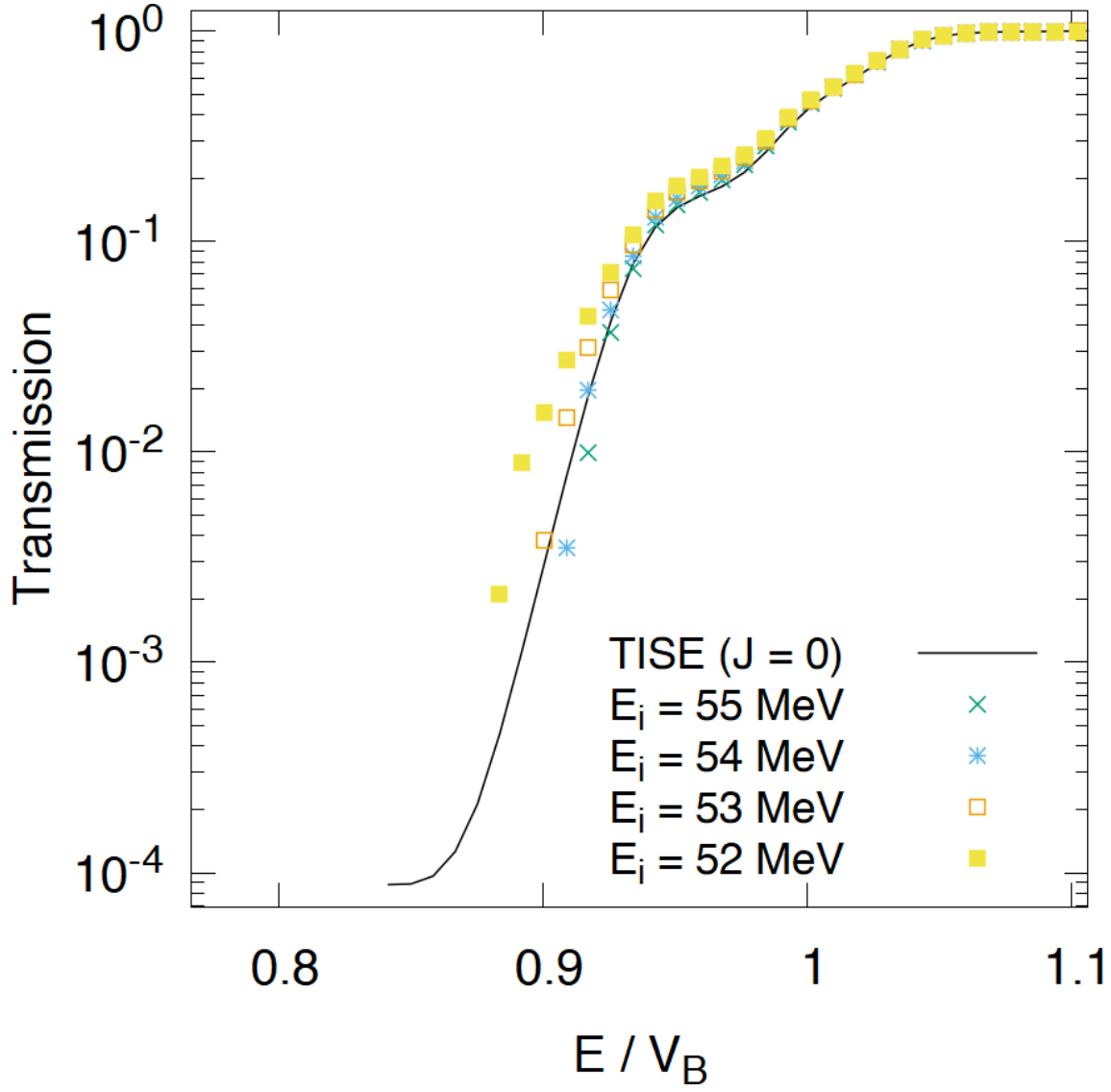

Figure 6.8: Transmission coefficients for varying low E_i. Propagating into lower E_i does not improve the convergence of the TDCCWP transmission coefficients with the TISE.

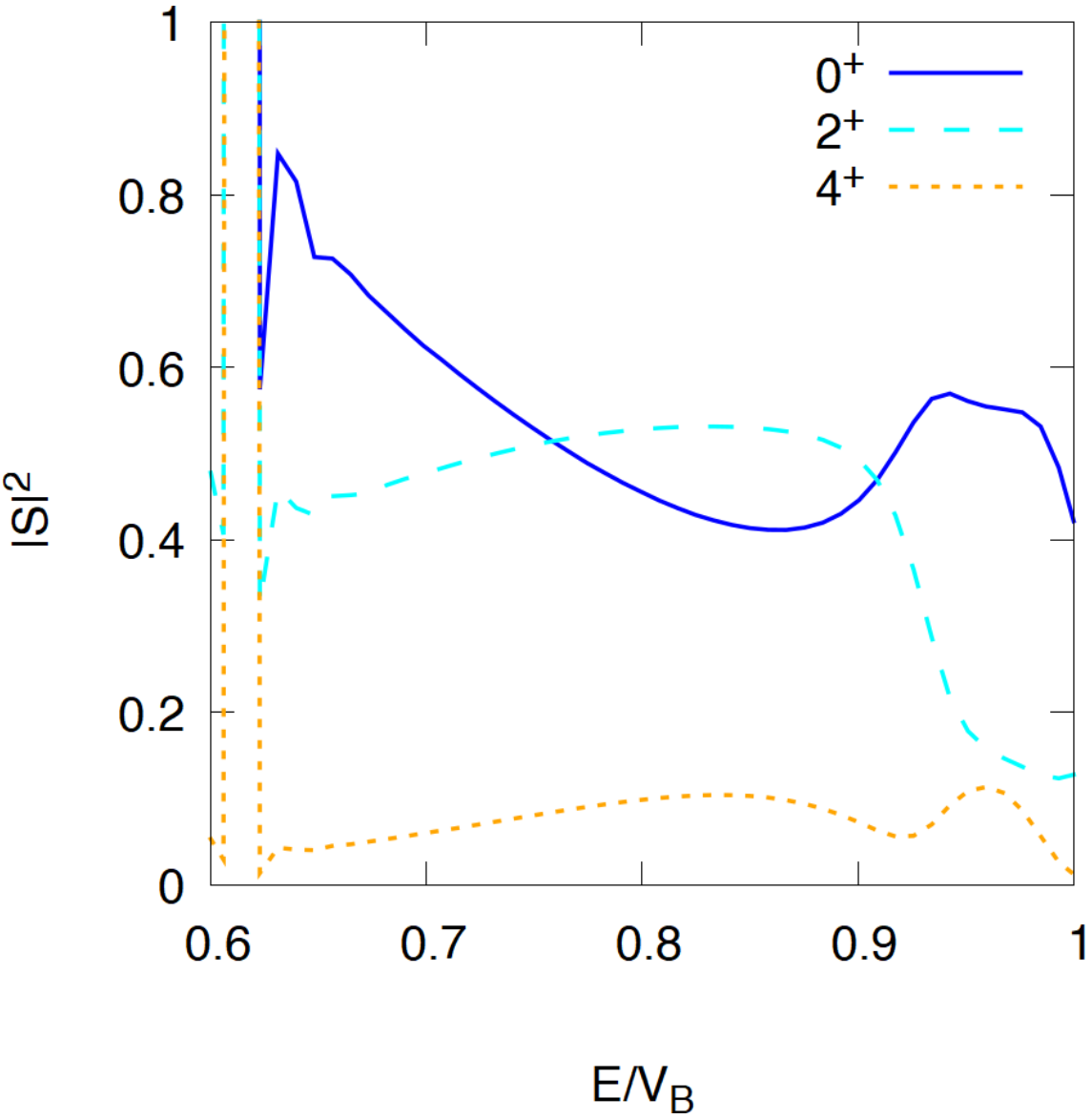

Figure 6.9: Reflection probabilities $\left|S^{BF}_{\beta\alpha}(E,J)\right|^2$ for $E_i = 55$ MeV for each of the different final spin states. Between $E \approx 0.7V_B$ and $E \approx 0.8V_B$, we have a coincidence where the 0^+ gradient is positive, and the inelastic gradients are negative or zero. For decreasing E/V_B, eventually we encounter unphysical results due to numerical inaccuracy.

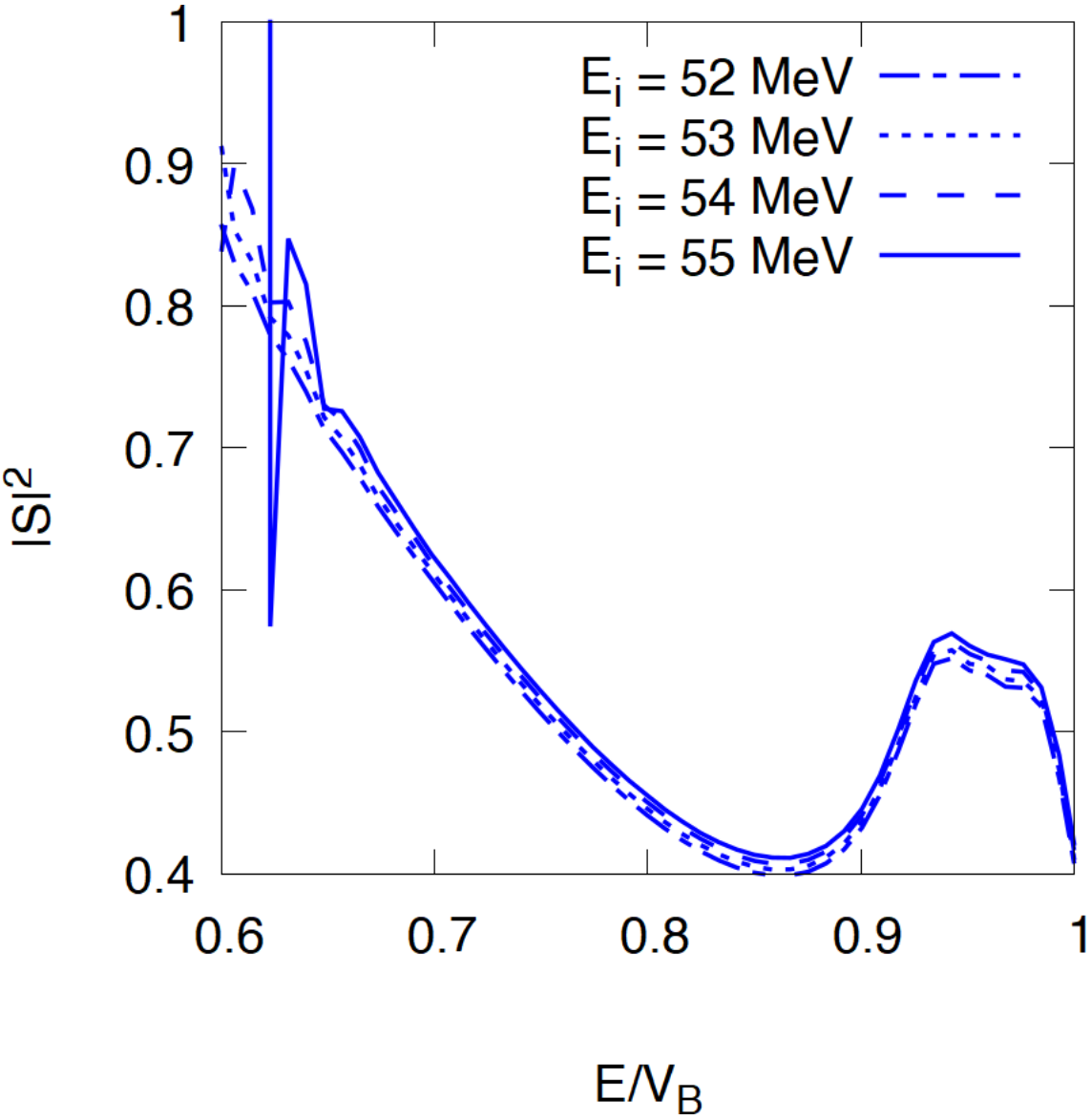

Figure 6.10: Reflection probabilities $\left|S^{BF}_{\beta\alpha}(E,J)\right|^2$ for varying E_i and final target spin state 0^+. The sign of the gradient is conserved as we decrease E_i, supporting the idea that this gradient stays positive, and brings the elastic S-matrix elements to unity. For decreasing E/V_B, each E_i value eventually generates a curve with unphysical results due to numerical inaccuracy.

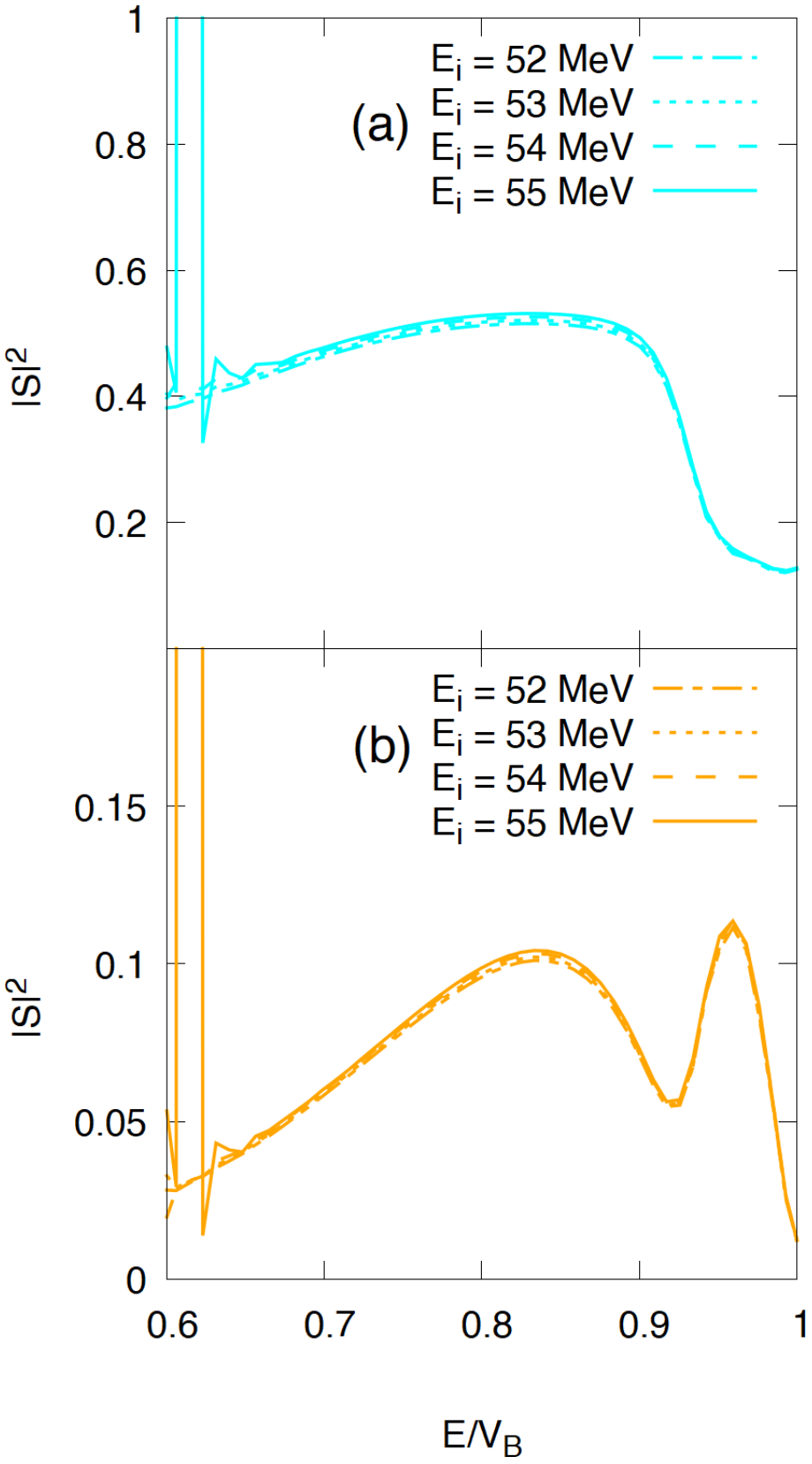

Figure 6.11: Same as Fig. 6.10, but for a) 2^+ and b) 4^+ target rotational states. As E_i is decreased, the sign of the gradient is negative and conserved, which will lead the inelastic S-matrix elements to zero.

Given what we know about the low energy limits of the complex radii of the S-matrix elements and Figs. 6.10 and 6.11, the behaviour of the sub-barrier complex radii of the S-matrix elements appears similar to the logistic function

$$f(x) = \frac{L}{1 + \exp(-k(x - x_0))} + C, \tag{6.3}$$

where L is the maximum value, k is the steepness and x_0 fixes the midpoint of the curve and C is a constant. Assuming $k > 0$ and $C = 0$, for $x \ll x_0$ the curve plateaus at zero, and for $x \gg x_0$ it plateaus at L. This behaviour is qualitatively similar to what we expect from both our S-matrix complex radii and the transmission coefficients, and thus this choice of fitting function is sensible.

After fitting both the low energy S-matrix elements and the transmission to logistic functions, the new transmission coefficients are shown in Fig. 6.12. The result matches the gradient of the TISE data very well and is satisfactory. The S-matrix reflection probabilities and phase shifts are shown in Figs. 6.13 and 6.14 respectively. The complex radii, fitted using the logistic function, are quantitatively accurate for low energies. The phase angles of the S-matrix elements for a given J are extrapolated using a Taylor expansion using the lowest E_i data-set, i.e.

$$\Phi(E, J) = \sum_{n=0}^{n_{\max}} \frac{\Phi^{(n)}(E_{\text{ex}}, J)}{n!}(E - E_{\text{ex}})^n, \tag{6.4}$$

where E_{ex} is a low energy and $\Phi^{(n)}(E_{\text{ex}}, J)$ is the n^{th} order derivative of $\Phi(E, J)$ evaluated at E_{ex}, which is approximated using a central finite difference method

$$\Phi^{(n)}(E_{\text{ex}}, J) = \frac{\Phi^{(n-1)}(E_{\text{ex}} + \Delta E, J) - \Phi^{(n-1)}(E_{\text{ex}} - \Delta E, J)}{2\Delta E}, \tag{6.5}$$

where $\Delta E = 0.5$ MeV, which is the spacing of our S-matrix energy grid. The $\Phi^{(n-1)}(E_{\text{ex}} \pm \Delta E, J)$ are evaluated using a backwards and forwards finite difference method respectively. To ensure accuracy, $n_{\max}$ was chosen to be equal to 50. The phase shifts show little deviation as the energy decreases. For energies above the barrier, the phase angles become erratic. This is due to high transmission at these energies which means what little of the wave-packet that is reflected is effectively numerical noise. This is not a problem that needs addressing, since the complex radii in these energy ranges tend to zero and so these erratic phase angles do not affect the sum in equation (5.2).

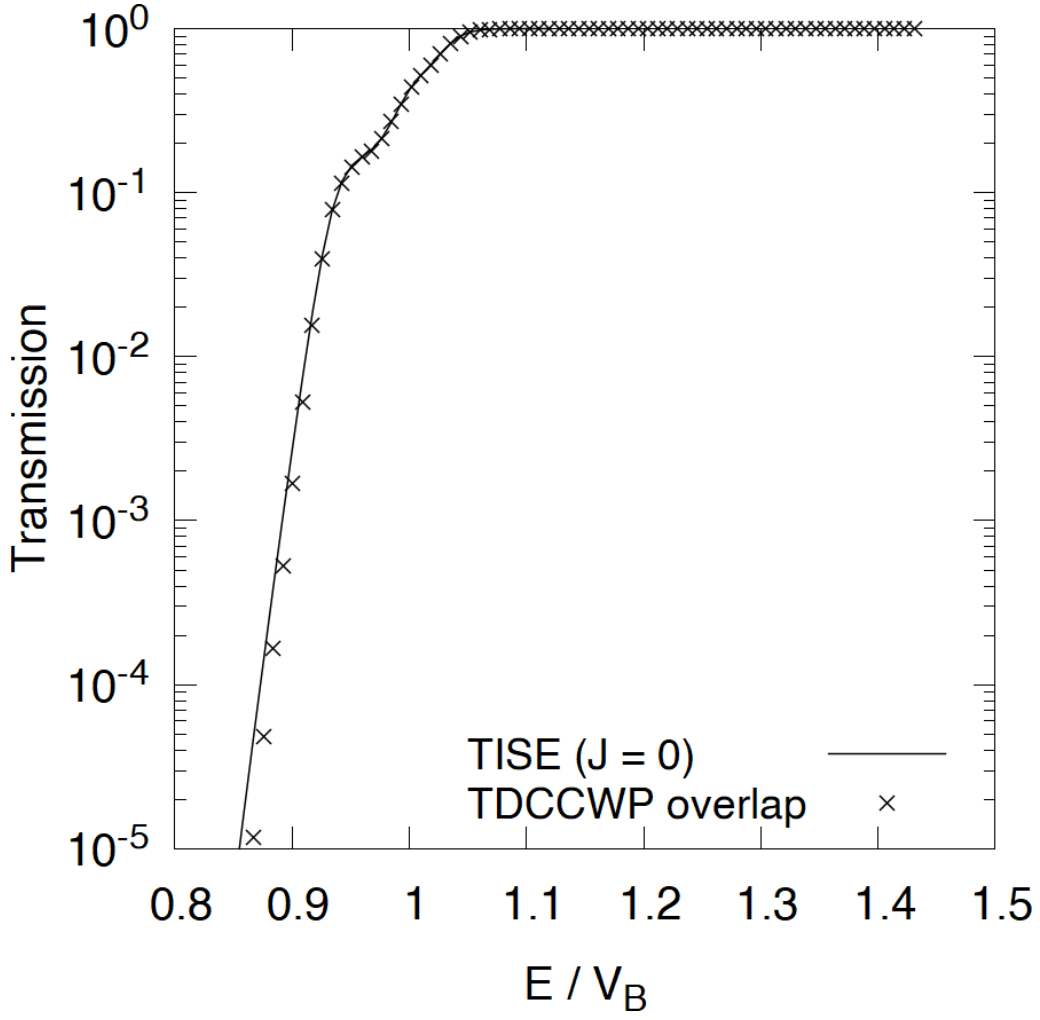

Figure 6.12: Overlapped and fitted transmission coefficients using the data from Fig. 6.6 and the logistic fitting procedures described in the text.

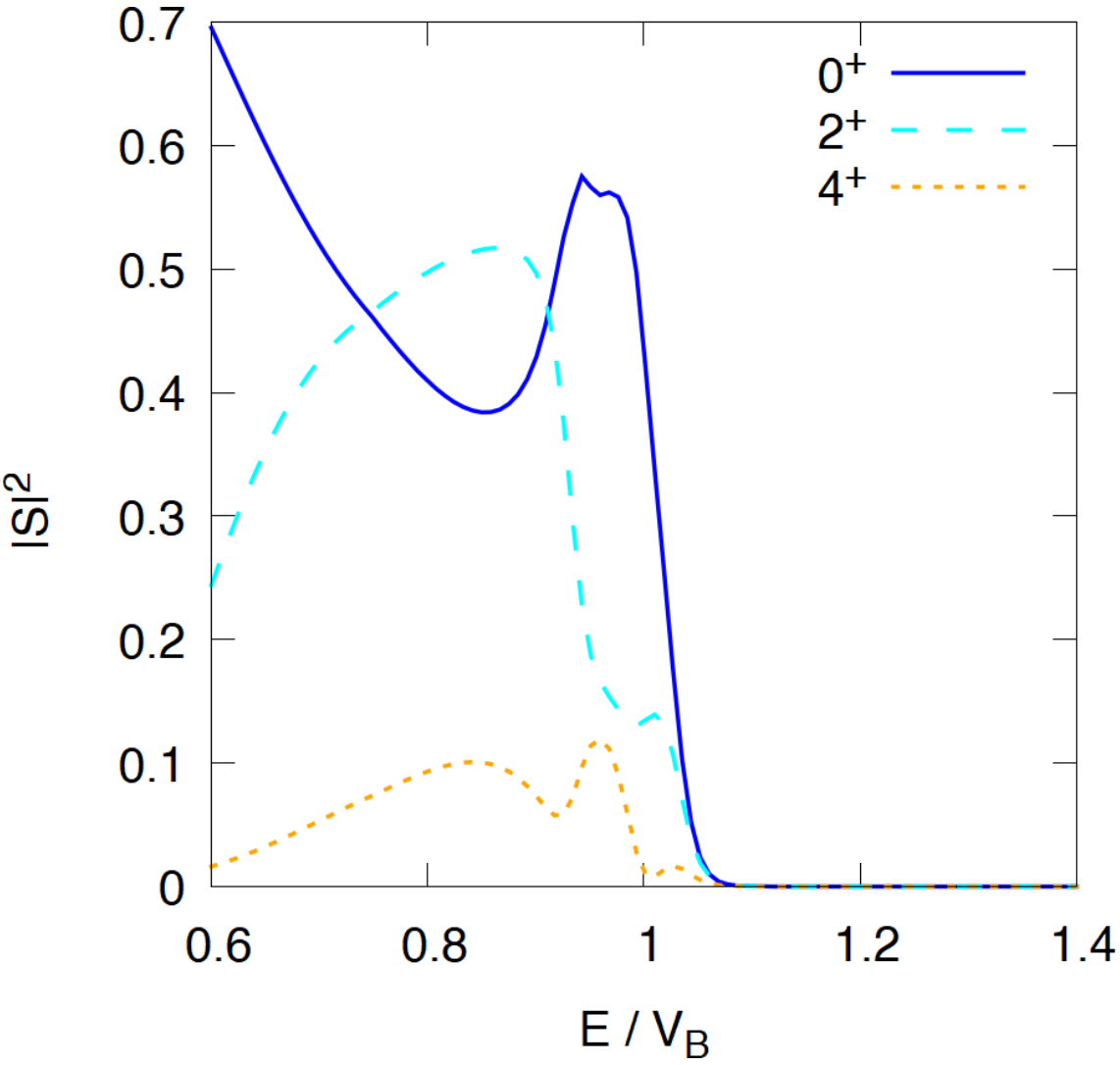

Figure 6.13: Complex radius of the S-matrix elements for each of the different final spin states. Logistic fitting used for all three curves, extrapolating to unity for the elastic elements and 0 for the inelastic.

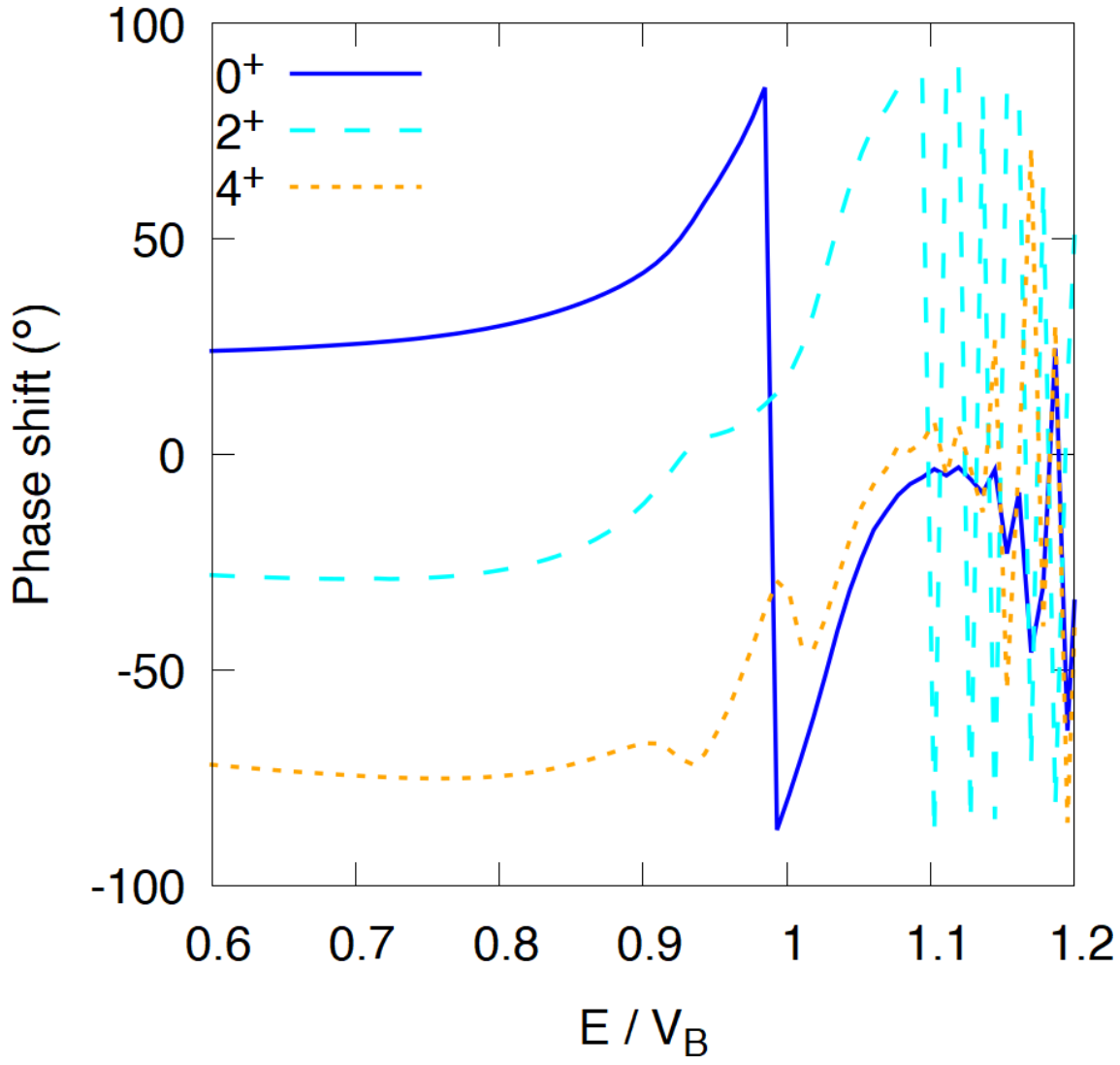

Figure 6.14: Same as Fig. 6.13, but for the phase shifts. The phase shifts become erratic for energies above the barrier height due to the reflected waves becoming near zero in amplitude, which makes numerical calculations for the phase shifts very inaccurate.

6.6 Comparison with FRESCO results

In this section, we compare the TDCCWP S-matrix with results generated from the FRESCO code [59] using the iso-centrifugal setting, which is a time-independent coupled-channel method that can calculate S-matrix elements and differential cross sections. FRESCO solves the TISE with a coupled-channels Hamiltonian of the same form as equation (2.5) [59]. From Fig. 6.15, we can see that the TDCCWP S-matrix elements are qualitatively similar to the FRESCO results. The main differences are that the FRESCO wave-functions are determined up to an unknown constant phase factor, the implementation of the iso-centrifugal approximation in FRESCO contains spin-orbit coupling form factors, and the coupled-channel calculations in FRESCO use higher order Coulomb interactions. In fact, if we correct for the constant phase factor in the TDCCWP results, the phase patterns become much more similar to that of FRESCO. This is shown in Figs. 6.18 and 6.19. The correction phase was chosen to be the value such that the phase shifts for both methods are equal at $E = 35$ MeV, an asymptotically small energy. Now we can see a more striking resemblance between the two methods, and have confidence that our method is qualitatively accurate at least.

6.6.1 Convergence of the elastic differential cross sections

At high J values, the combination of the elastic reflection probability and a phase shift of zero converges equation (5.2). As it stands, with this non-zero phase at low energies in Fig. 6.16, the results of equation (5.2) using the TDCCWP S-matrix elements will not converge. This is because the summand in equation (5.2) will always have a non-zero result for high J values. Therefore, we have decided to adjust all of the elastic phase shifts to match the $J = 0$ phase shifts like in Fig. 6.18. This allows us to simply use only the FRESCO results for $J = 0$ to correct the phase factors. Whilst there is an extremely slight dependence on the asymptotic phase shifts and the J value in the FRESCO data (shown in Fig. 6.20), correcting the TDCCWP elastic phase shifts to the $J = 0$ data is a sensible approximation. The TDCCWP results also have a slight dependence on the J value, but it is much larger than the dependence on J in the FRESCO results. This dependence is likely (at least in our method) due to small numerical inaccuracies. Due to this slight dependence and in order to be consistent, we opt to correct the inelastic data like in Fig. 6.19 as well. It is less important to do this because, from equation (5.2), any global phase factor will not affect the calculation of the inelastic differential cross section. For all J the difference between the TDCCWP method and the FRESCO results is approximately a constant global phase factor, which again can be seen in Fig. 6.20. After these phase corrections, our TDCCWP method produces similar results for $J = 20$ and 30, which are shown in Figs. 6.21 and 6.22. We are confident that, after these curation processes, our results are reasonably accurate, and thus we can begin to investigate the differential cross sections.

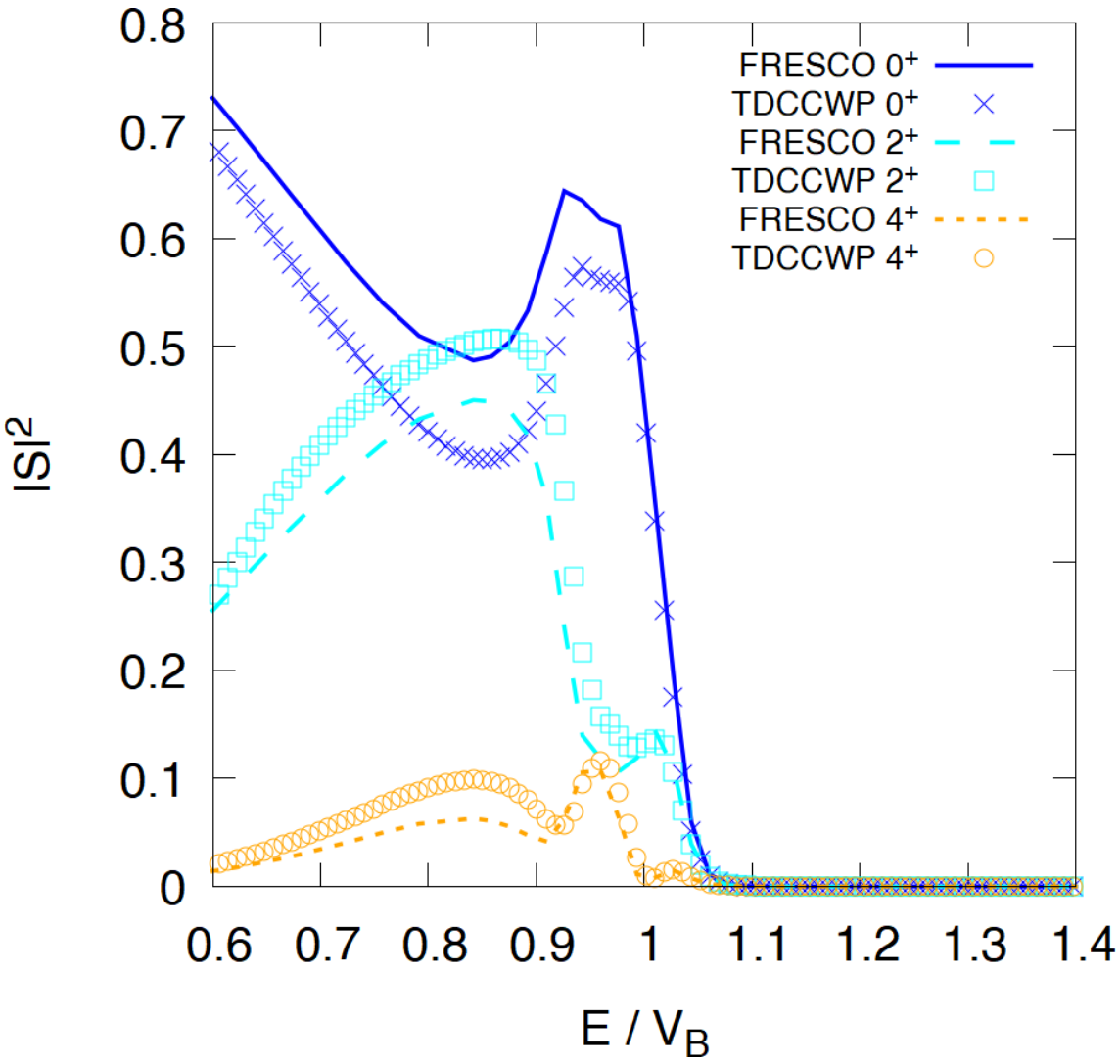

Figure 6.15: Comparison between the TDCCWP method and FRESCO results for the reflection probabilities for $J = 0$. Differences between the two methods are detailed in the text. The results between both methods are qualitatively similar.

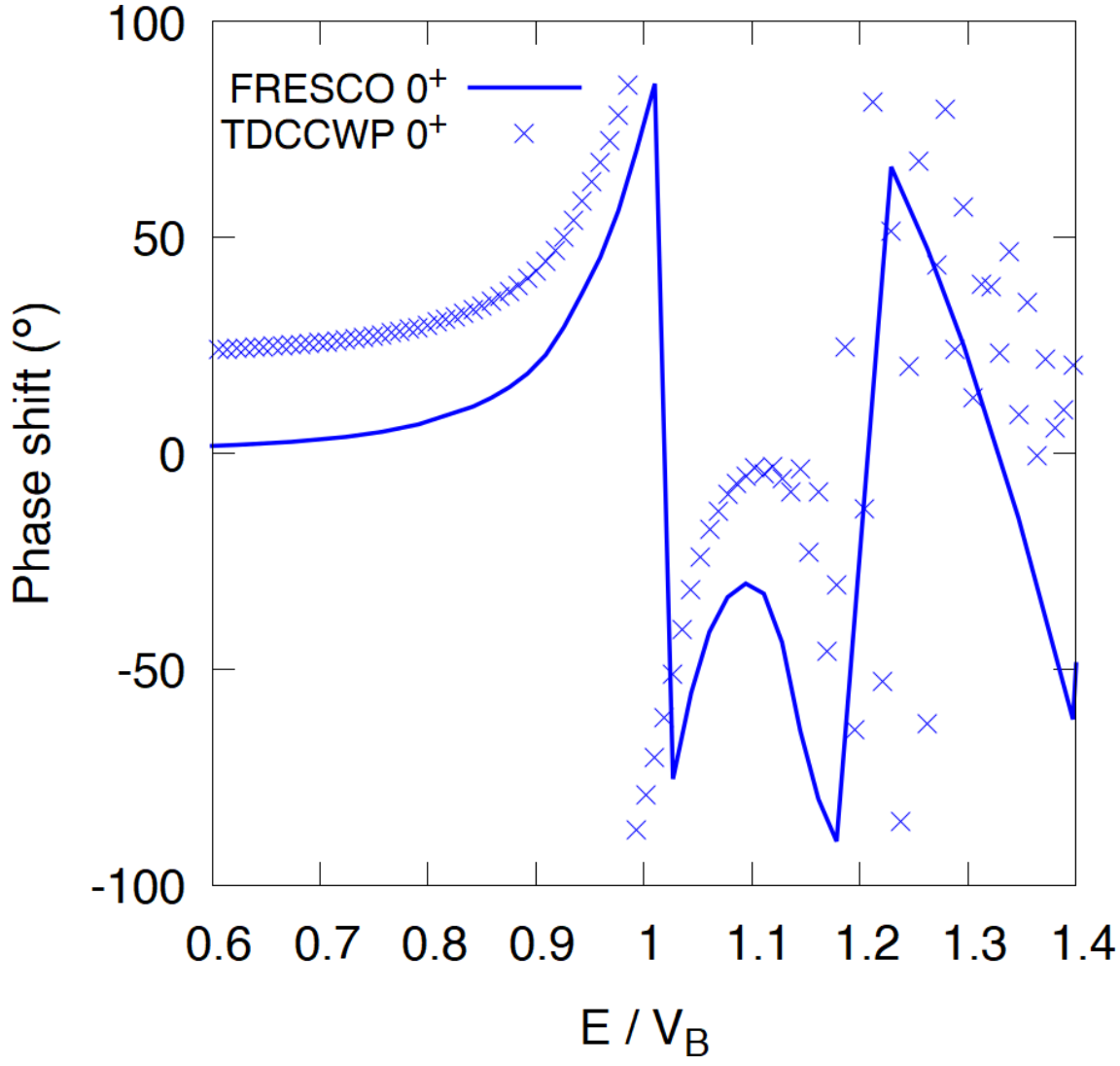

Figure 6.16: Phase shifts for $J = 0$ and the 0^+ target state. Solid line is the FRESCO calculation, and crosses are from the TDCCWP method. The results show a near constant phase difference between the two curves, which is not accounted for in the FRESCO method.

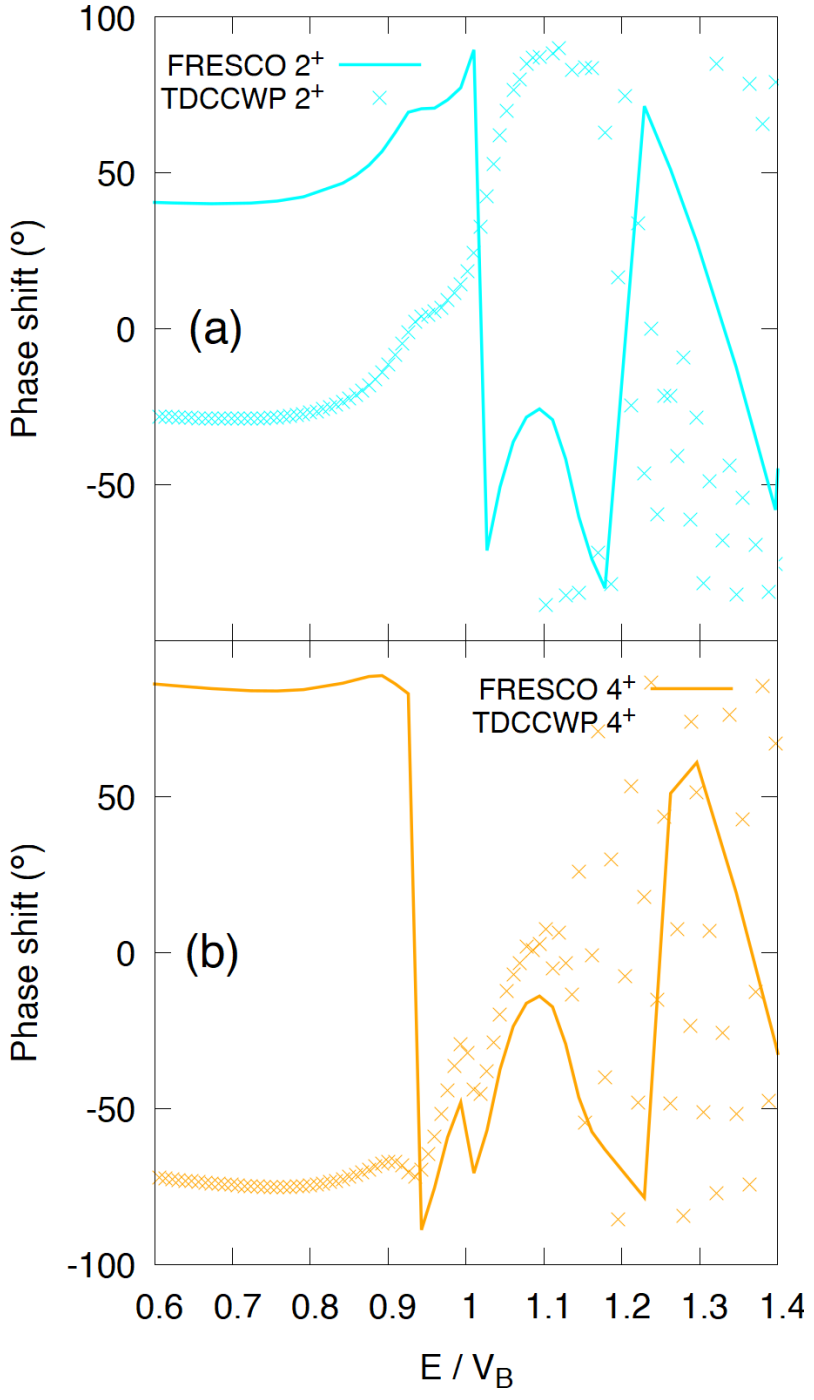

Figure 6.17: Same as Fig. 6.16, but for the a) 2^+ b) 4^+ target state.

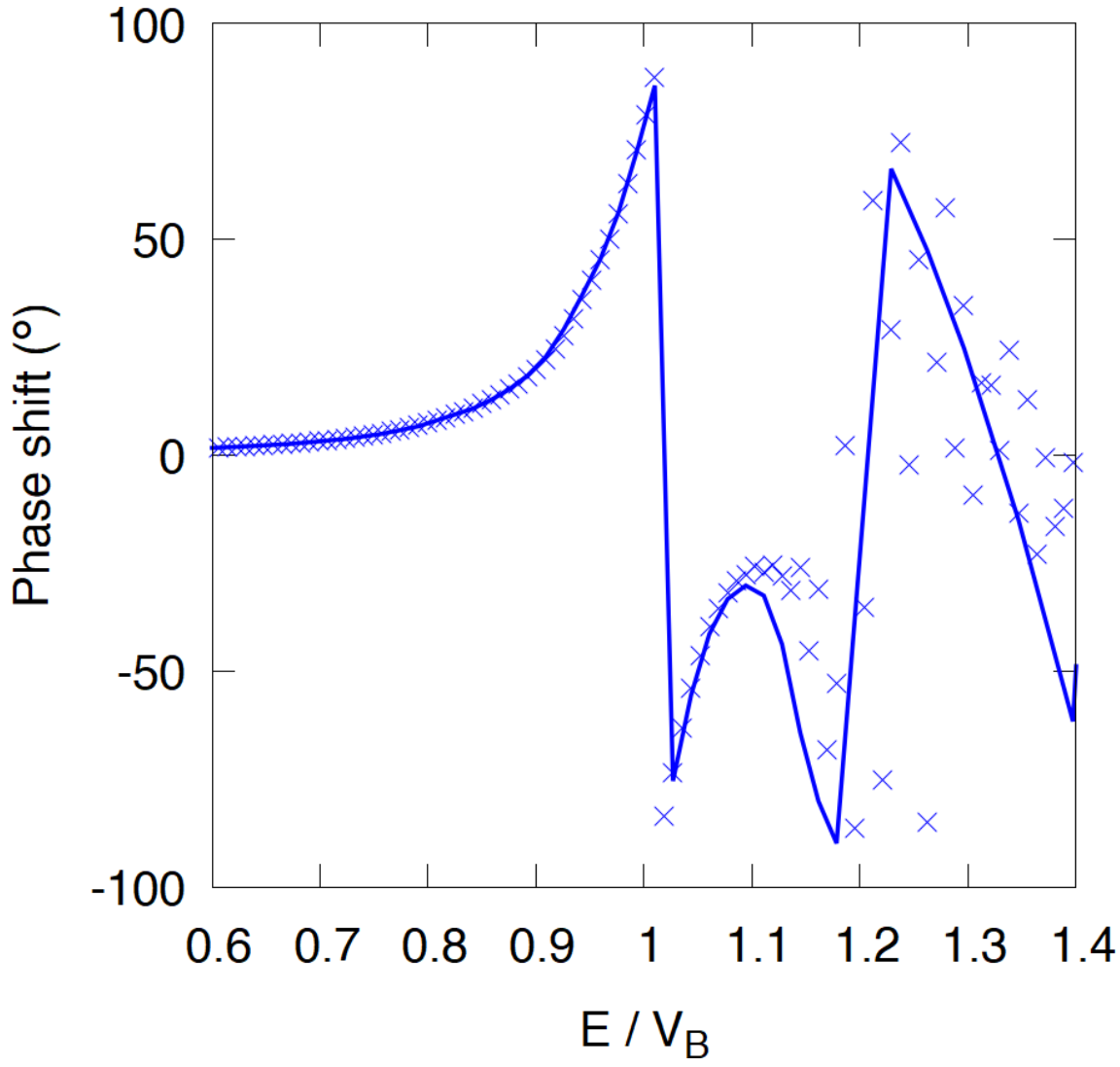

Figure 6.18: Phase shifts for $J = 0$ and the 0^+ target state. Solid line is the FRESCO calculation, and crosses are from the TDCCWP method after adding a constant phase. The constant phase was chosen to be the value such that the phase shifts for both methods are equal at $E = 35$ MeV, an asymptotically small energy.

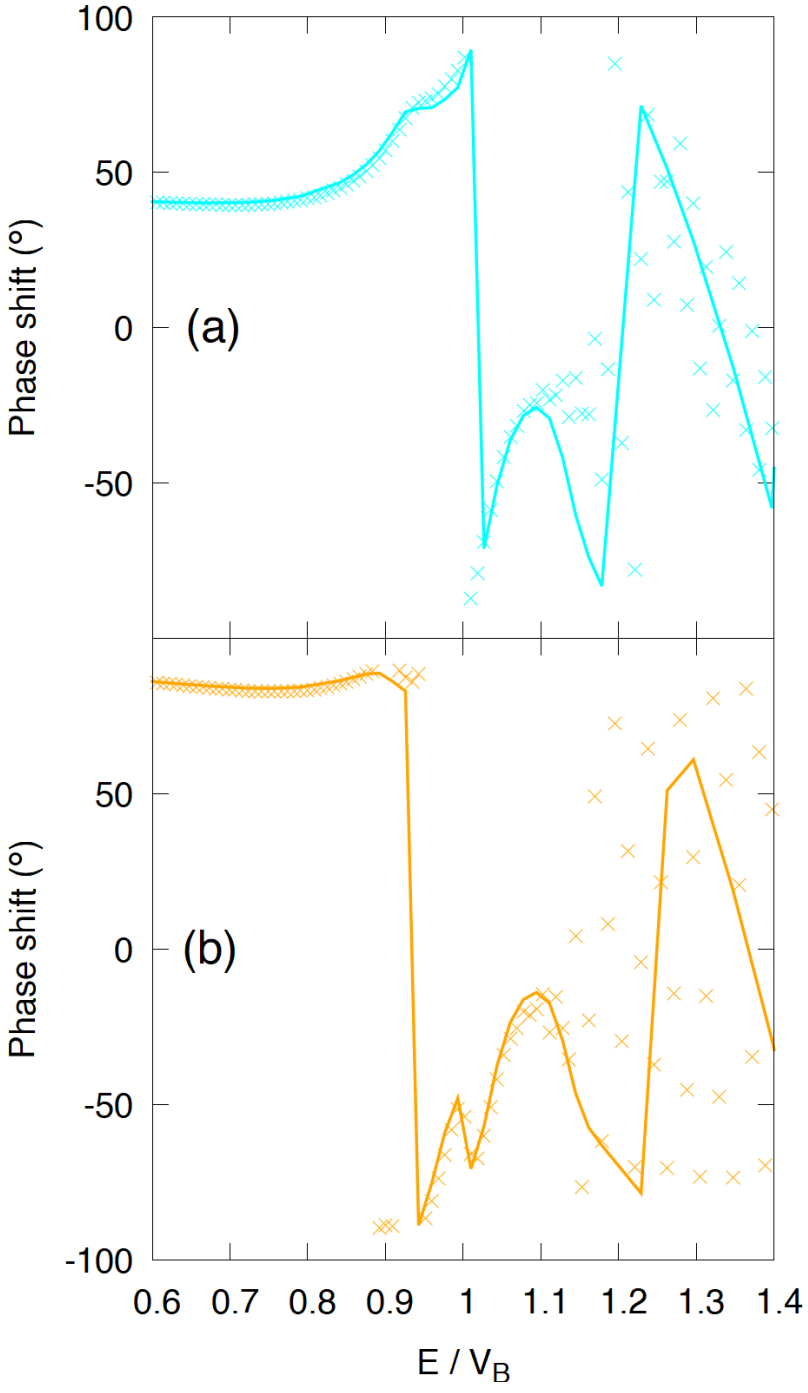

Figure 6.19: Same as Fig. 6.18, but for the a) 2^+ b) 4^+ target state.

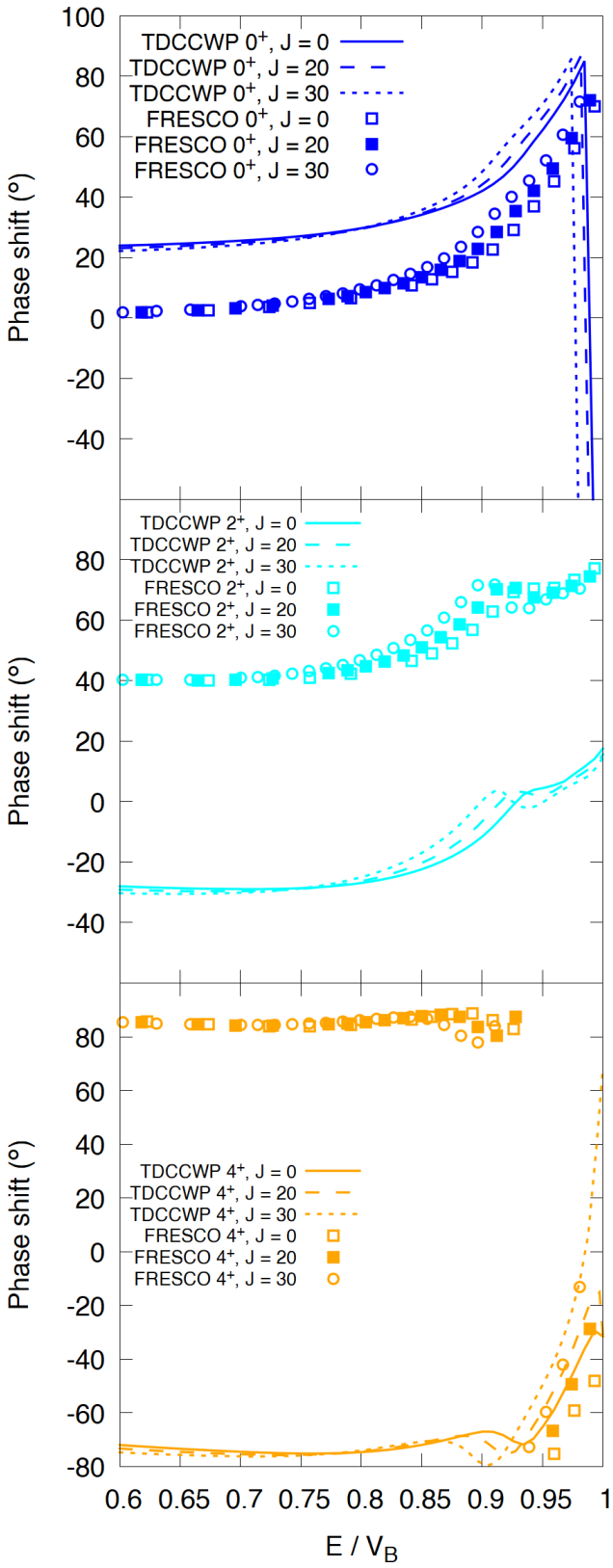

Figure 6.20: Uncorrected TDCCWP phase shifts vs. FRESCO for varying J. Both methods show a very slight J dependence, with the TDCCWP results showing a stronger relationship, likely due to numerical inaccuracies.

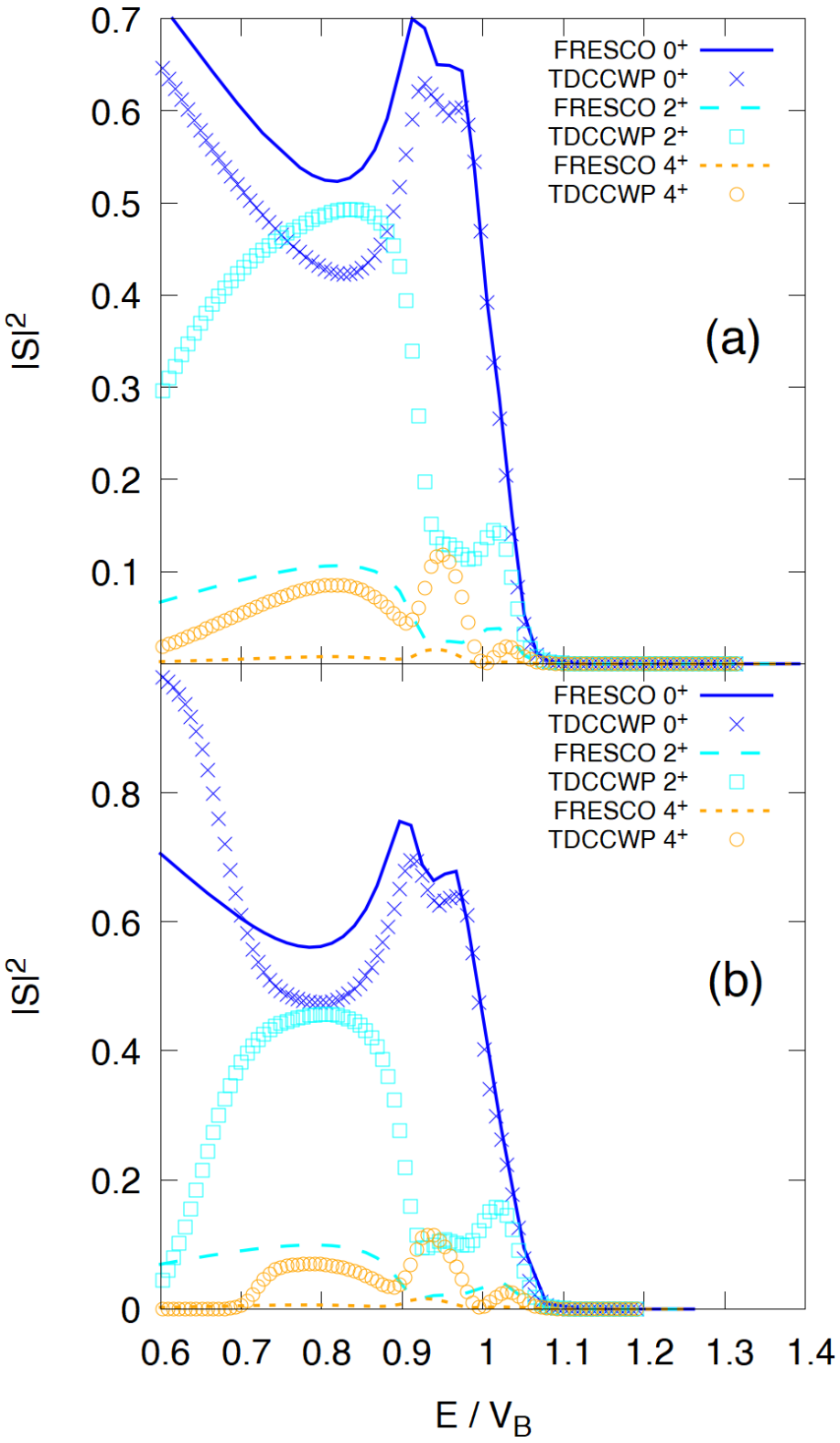

Figure 6.21: Comparison between FRESCO and TDCCWP S-matrix reflection probabilities for a) $J = 20$ b) $J = 30$. There is a similar qualitative agreement between the two methods like in Fig. 6.15.

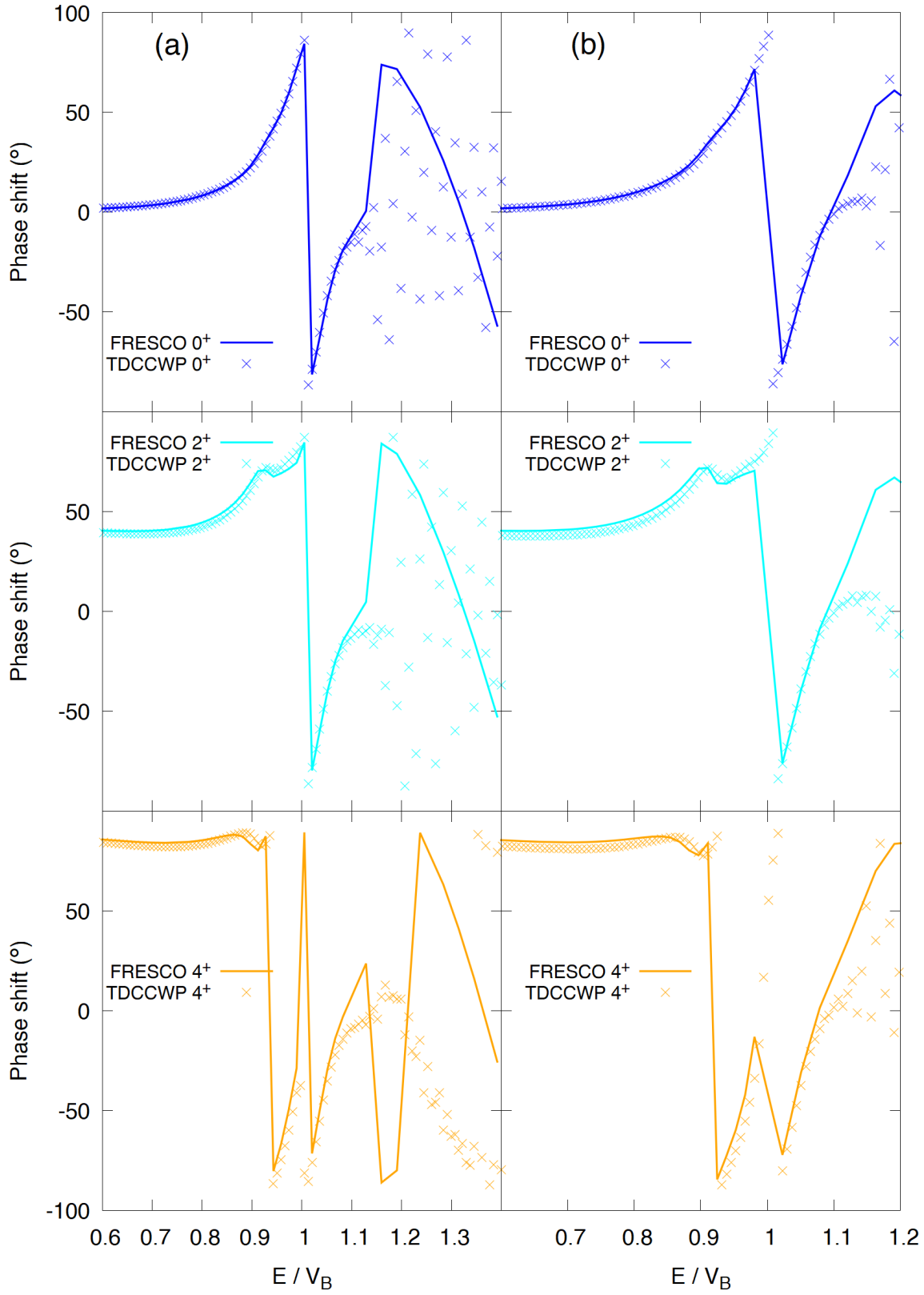

Figure 6.22: Same as Fig. 6.21, but for the a) $J = 20$ b) $J = 30$ phase shifts.

6.7 Summary

We performed time propagations of the S-matrix, and were able to replicate the time-independent transmission coefficients by varying the initial energy E_i. We verified that the integrals needed to find the S-matrix elements were calculable, and that after a long time the integrals converged as expected. We also verified that the choice of initial condition is extremely important to obtain the most accurate results.

Since we required the S-matrix elements for increasingly lower energies below the barrier height, we performed calculations for $J = 0$ for decreasing E_i. We found that the transmission (or normalisation of the S-matrix elements) was not improved by decreasing the initial energy in this way. However, since the data showed an expected trend where the elastic reflection probability goes to unity and the inelastic to zero, we employed a sigmoid fit to the data to help describe these low energy elements. We also used a very high order Taylor expansion in order to extrapolate the phase shifts.

Comparing this new curated data to the results of FRESCO, the S-matrix elements are reasonably similar. FRESCO calculations that use the iso-centrifugal approximation still contain form factors relating to spin-orbit coupling, and the coupled-channel calculations in FRESCO use higher order Coulomb interactions. We also noticed that the TDCCWP results have an almost constant phase factor difference between the phase shifts. This is because the FRESCO calculations involve a diagonalisation method, so the FRESCO S-matrix is determined up to a constant phase factor. The presence of these phase shifts have stark implications for the calculation of the differential cross section, and due to their unphysical implications for the differential cross sections, we have decided to correct for the phase factors by shifting the phases to replicate the $J = 0$ FRESCO data. This produces similar phases for all J values.

Chapter 7

TDCCWP differential cross section results

In the previous chapter, we established the need for extrapolation techniques for the S-matrix elements in order to generate sub-barrier elements with some accuracy. We compared this to the FRESCO method, which produced qualitatively similar results to ours within reason. Notably, the TDCCWP results included a constant phase difference that is not accounted for in the FRESCO calculations. Since this prevents the convergence of the elastic differential cross sections, we correct for the phase factor in the S-matrix elements. Now, in this chapter we will investigate what the differential cross sections look like using our method.

7.1 ^{16}O + ^{154}Sm collisions

7.1.1 Inelastic transition probabilities

We define the inelastic transition probability as $\mathbb{P}_{\beta\alpha J}(E) = \left|S^{SF}_{\beta\alpha}(E,J)\right|^2$. The inelastic transition probability is the probability of the transition from entrance channel αi to exit channel βf, for a specified E and J. We use equation (5.7) to calculate the inelastic transition probabilities, with our fitted S-matrix elements from our calculations of equation (5.11). We will focus on energies close to and above the barrier as this is a novel result, which conveniently avoids errors due to the extrapolation. Whilst it may seem like these results ought to be in the previous chapter, they will help us in explaining an interesting feature that appears in the differential cross sections.

The inelastic transition probabilities as a function of E/V_B for varying J are shown in Figs. 7.1 and 7.2. As J is increased, the overall probability decreases as a function of E/V_B, due to a combination of the decrease in interaction time and the decay

of the 3-J symbols used in equation (5.7). For energies below the barrier height, as J increases Fig. 7.1 shows the development of a local maximum in the interval $1 < E/V_B < 1.05$, and two local minima in the interval $0.9 < E/V_B < 1$ in the 2^+ transition probability. Fig. 7.2 shows a local maximum locating deeper below the barrier energy in the 4^+ transition probability. In fact, these two effects coincide with one another and produce a situation where the 4^+ transition probability is very close in value to the 2^+ transition probability. This is shown in Fig. 7.3. Note that this effect is present at $E \approx 66$ MeV. To verify this, a time propagation of a wave-packet with $E_i = 66$ MeV and $J = 30$ was performed, and indeed we see in Fig. 7.4 that the 4^+ scattering is at a similar order of magnitude to the 2^+ scattering.

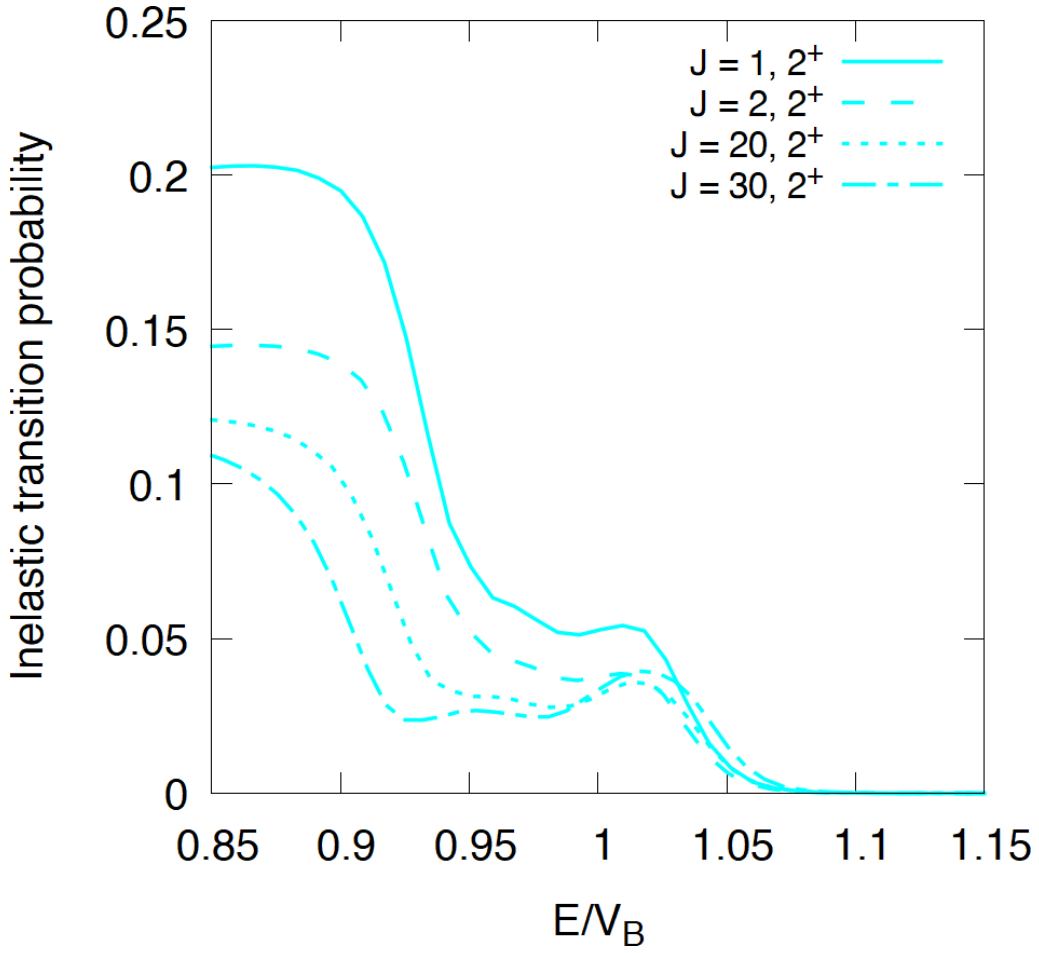

Figure 7.1: Inelastic transition probabilities for the 2^+ state in ^{154}Sm for varying J.

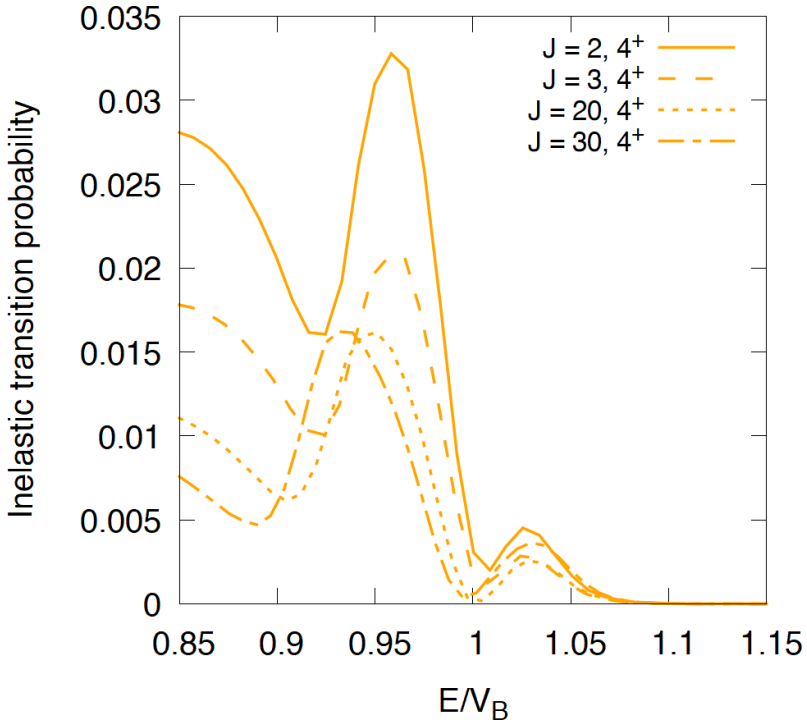

Figure 7.2: Same as Fig. 7.1, but for the 4^+ state.

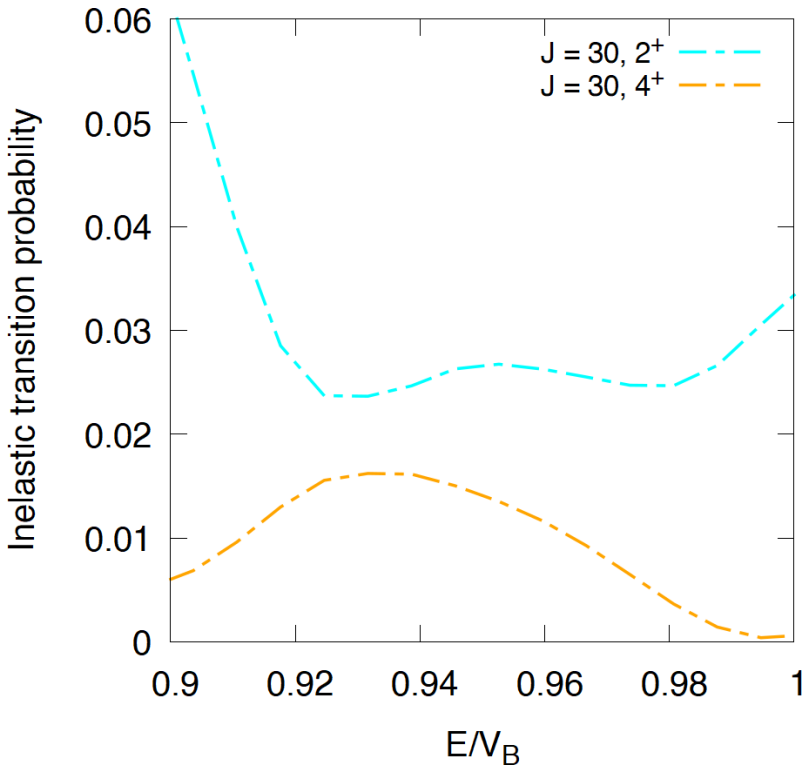

Figure 7.3: Inelastic transition probabilities for the 2^+ and 4+ states of ^{154}Sm. At $E \approx 66$ MeV, the inelastic transition probabilities have similar values.

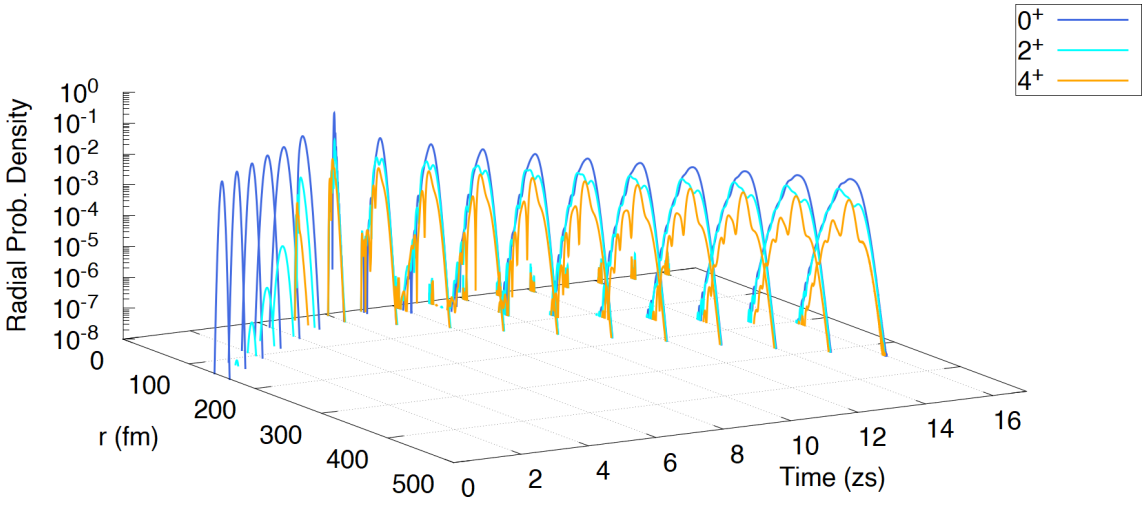

Figure 7.4: Time propagation of a radial wave-packet for $E_i = 66$ MeV and $J = 30$, which illustrates the effect of the similar inelastic transition probabilities at this energy from Fig. 7.3.

7.1.2 Differential cross sections

In this section, we have chosen to focus on collision energies $E = \{59, 66, 72\}$ MeV, and we include up to $J = 30$ in the evaluation of equation (5.2). These energies are chosen to give a reasonable idea of how calculations perform for energies below all barriers, energies above all barriers, and an intermediate energy. $E = 59$ MeV is relatively close to energy values where the S-matrix calculations for each J are accurate, but still within the extrapolated region. The other energies are outside of the extrapolated region for all J. These specific energies have experimental data for $^{16}\mathrm{O} + {}^{152}\mathrm{Sm}$, which can enable comparisons between the two nuclei if need be. For the case of $^{16}\mathrm{O} + {}^{154}\mathrm{Sm}$, we focus on looking at the effect of varying the number of channels.

Figs. 7.5, 7.6 and 7.7 show the differential cross sections for a varying number of channels, with partial waves up to $J = 30$. For the single channel case, any deviations from the Rutherford cross section are due to effects from the nuclear force. In our case, these are a combination of the fusion absorption from the absorption potential, and the effect of the presence of the Woods-Saxon potential. We can use the single channel data as a baseline to more thoroughly discern the effects of including the coupled-channels.

In Fig. 7.5, we can see that the introduction of channels to the calculation decreases the scattering for angles larger than $\approx 80°$. The decreases in elastic scattering at approximately $130°, 150°$ and $160°$ coincide with increases in scattering in the 2^+ and 4^+ differential cross sections. We can also see that as $\theta \to 180°$, the differential cross sections rapidly increase to large values, including the high energy analytical result, which is shown as a black solid line. We see that the forward angle differential cross sections are less sensitive to changing the number of channels at this energy, which is what we expect since these differential cross sections originate from high J value terms, which have higher barriers and prevent the two nuclei from getting close enough to react significantly via the nuclear force at this energy.

For $E = 66$ MeV, Fig. 7.6 shows a crossing of the 2^+ and 4^+ curves, which is consistent with the inelastic transition probabilities of Fig. 7.3 and the propagation in Fig. 7.4. As the number of channels increases from one to two, between $\theta \approx 90°$ and $\theta \approx 100°$, we can see that the elastic scattering decreases. We could imagine that for certain J values the introduction of a new channel provides a pathway, where elastic flux can avoid fusion absorption by exciting into the new excited state. This is because when the elastic state excites, the kinetic energy decreases due to the rigid rotor potential and thus this newly excited state becomes less penetrative. This can lead to an enhancement of the elastic scattering from the subsequent de-excitation of this newly excited scattering state. If this effect is indeed present, then it is less impacting when the number of channels increases from two to three, since we do not observe any elastic scattering enhancement in Fig. 7.6 when the number of channels increases in this way.

For $E = 72$ MeV, Fig. 7.7 shows that the behaviour at high angles has diminished

significantly, which is sensible since at these energies a majority of the nuclei will fuse at this energy for all the J values that we consider. The difference between the one, two and three channel cases at this energy is less significant, since at this energy all the barriers up to $J = 30$ have been classically penetrated, and thus there is less scattering. All of the energies show close to unity Rutherford ratio for small angles, which is consistent with expected results. They also show that for small angles, the majority of the 4^+ excitation originates from the 2^+, since at low angles the elastic differential cross section barely changes compared to the 2^+ cross section when the number of channels increases from two to three.

Fig. 7.8 shows the Rutherford ratios for a much higher energy of 115 MeV. For any amount of channels, the results from this should be very close to those from the high energy analytical solution of equation (5.6). As we can see, the Rutherford ratios are very close to the analytical solution at this energy, indicating our method for evaluating equation (5.2) is correct.

7.1.3 Comparison to experimental data

We present a comparison to experimental data in Fig. 7.9, which shows the differential cross section as a function of energy for $\theta = 175^\circ$ for up to $J = 30$ partial waves. There is not a strong agreement between the two data-sets, which is expected because $\theta = 175^\circ$ is a backwards angle, which means that low J values contribute most to the scattering and thus the iso-centrifugal approximation is very inaccurate. Note that increasing the number of partial waves does not help here, since the results are converged for a very low number of partial waves.

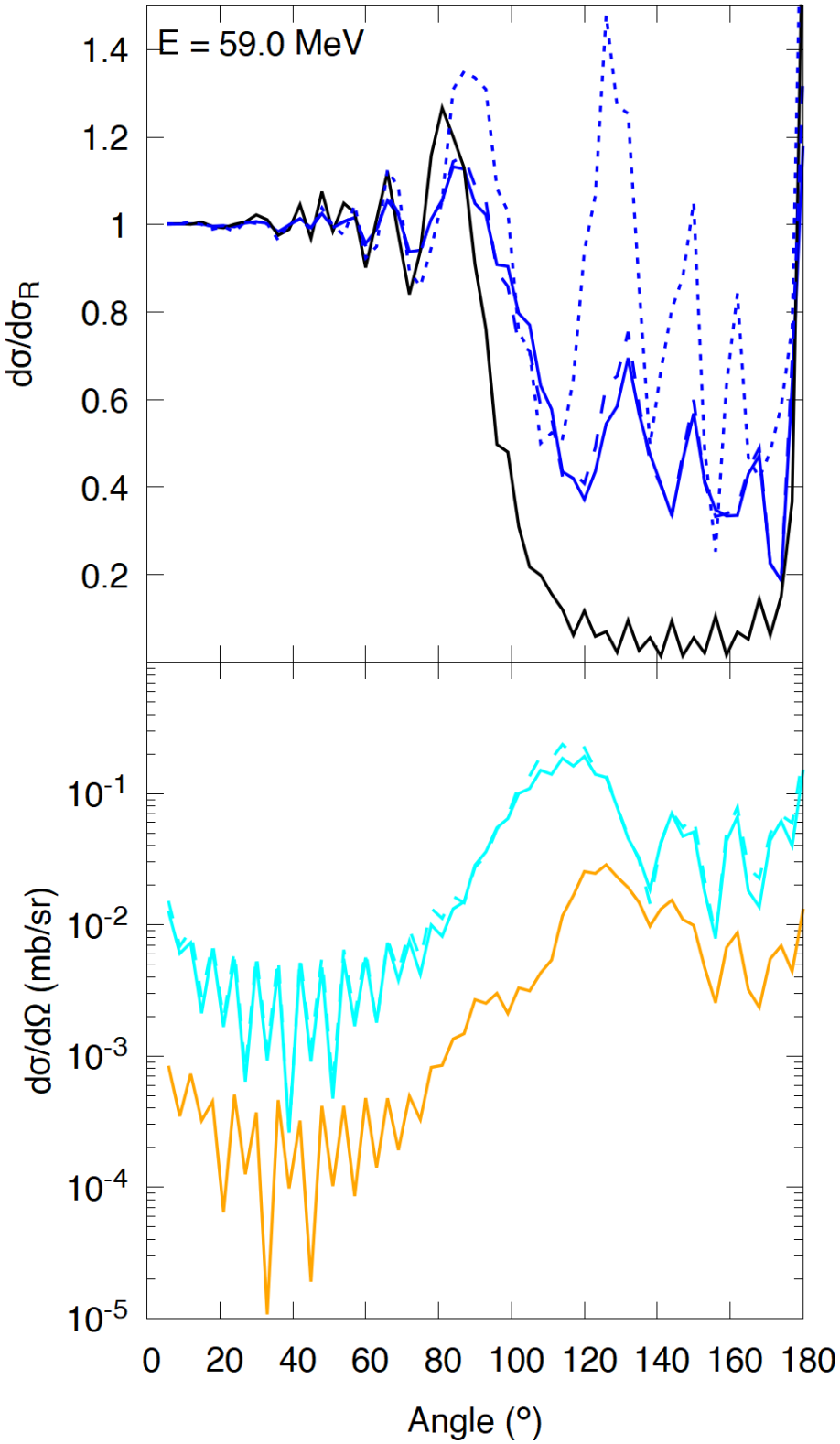

Figure 7.5: Our model calculations of ratio to Rutherford and the differential cross sections for $^{16}\mathrm{O} + {}^{154}\mathrm{Sm}$, for a varying number of channels at collision energy $E = 59$ MeV. The dotted line shows calculations involving a single 0^+ channel, the dashed line for two channels, and solid lines for the full three channel calculation. The high energy analytical result for the ratio to Rutherford from equation (5.6) is shown as a black solid line.

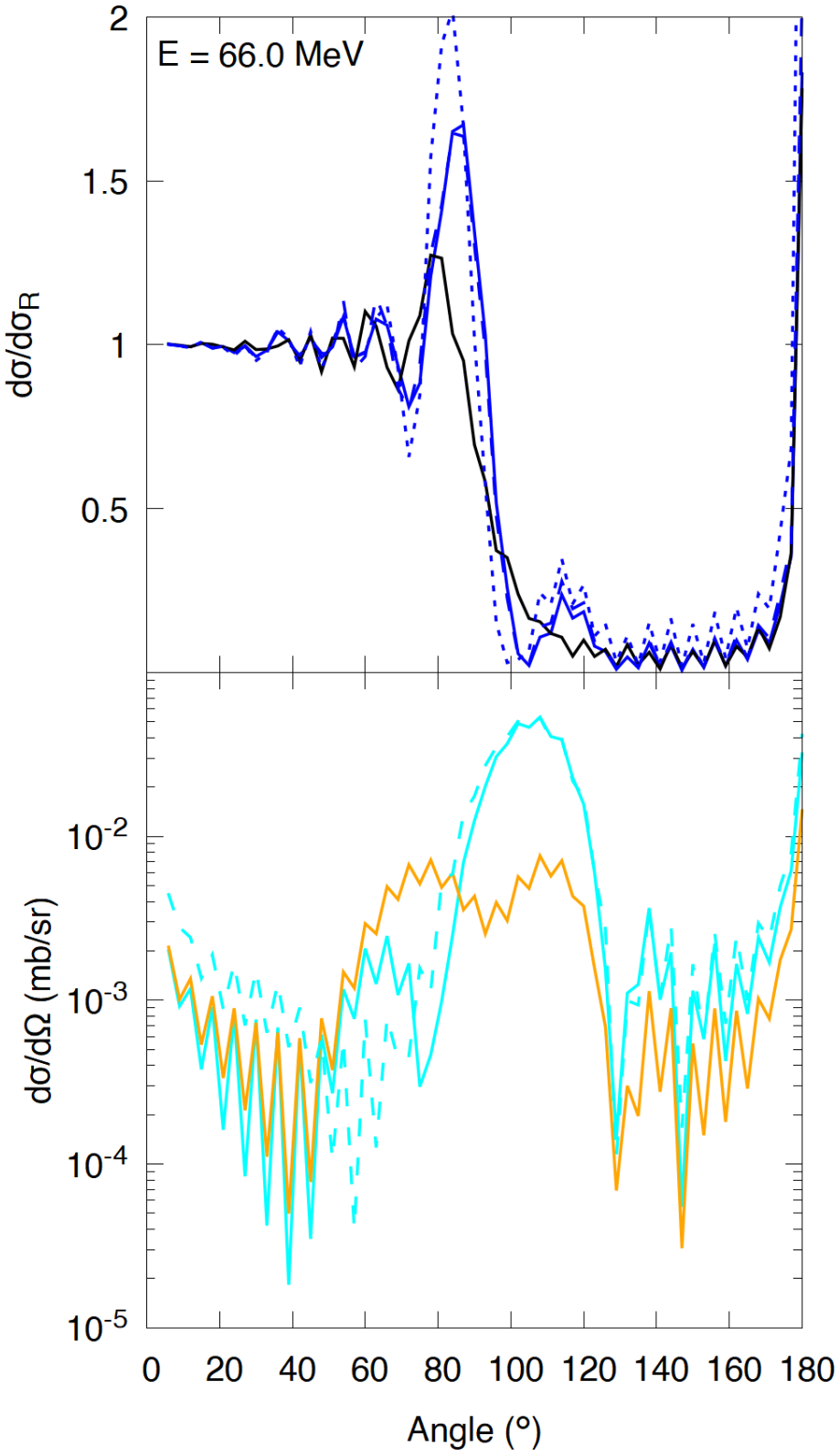

Figure 7.6: Same as Fig. 7.5, but for $E = 66$ MeV.

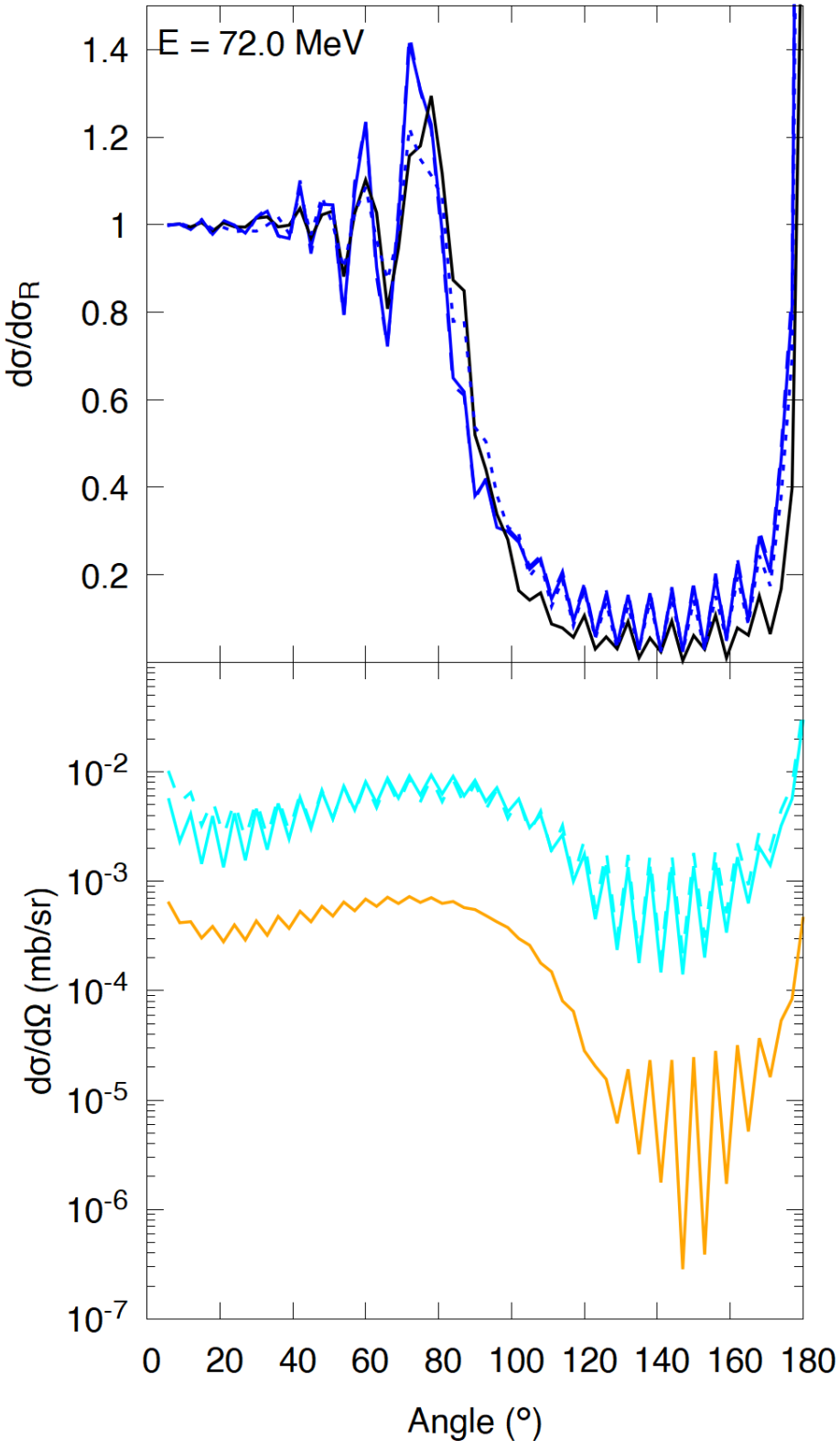

Figure 7.7: Same as Fig. 7.5, but for $E = 72$ MeV.

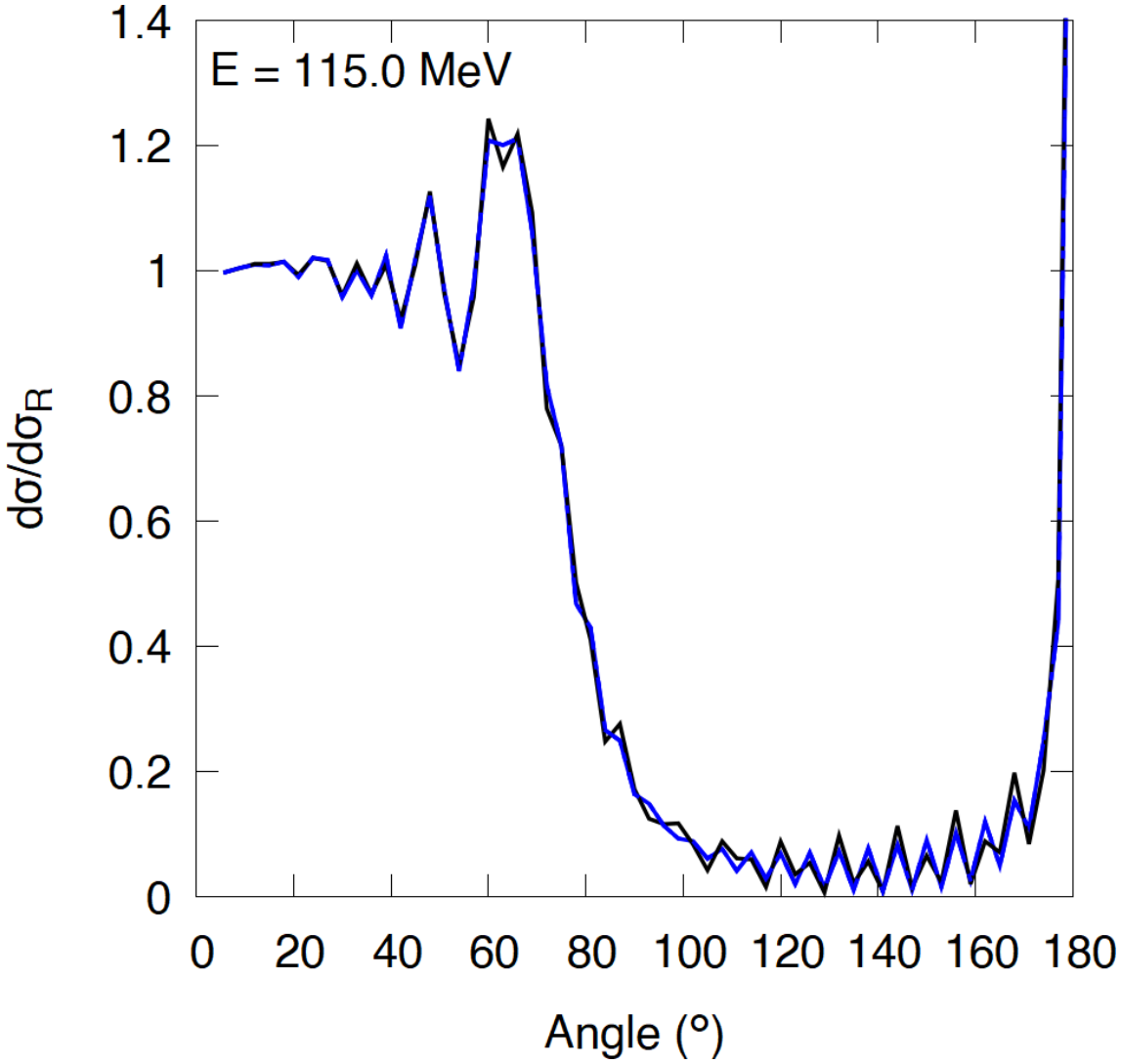

Figure 7.8: Same as the top half of Fig. 7.5, but for $E = 115$ MeV, the highest energy that we have used in our data-set. The elastic differential cross sections show a similar pattern to the high energy limit (i.e. equation (5.6)).

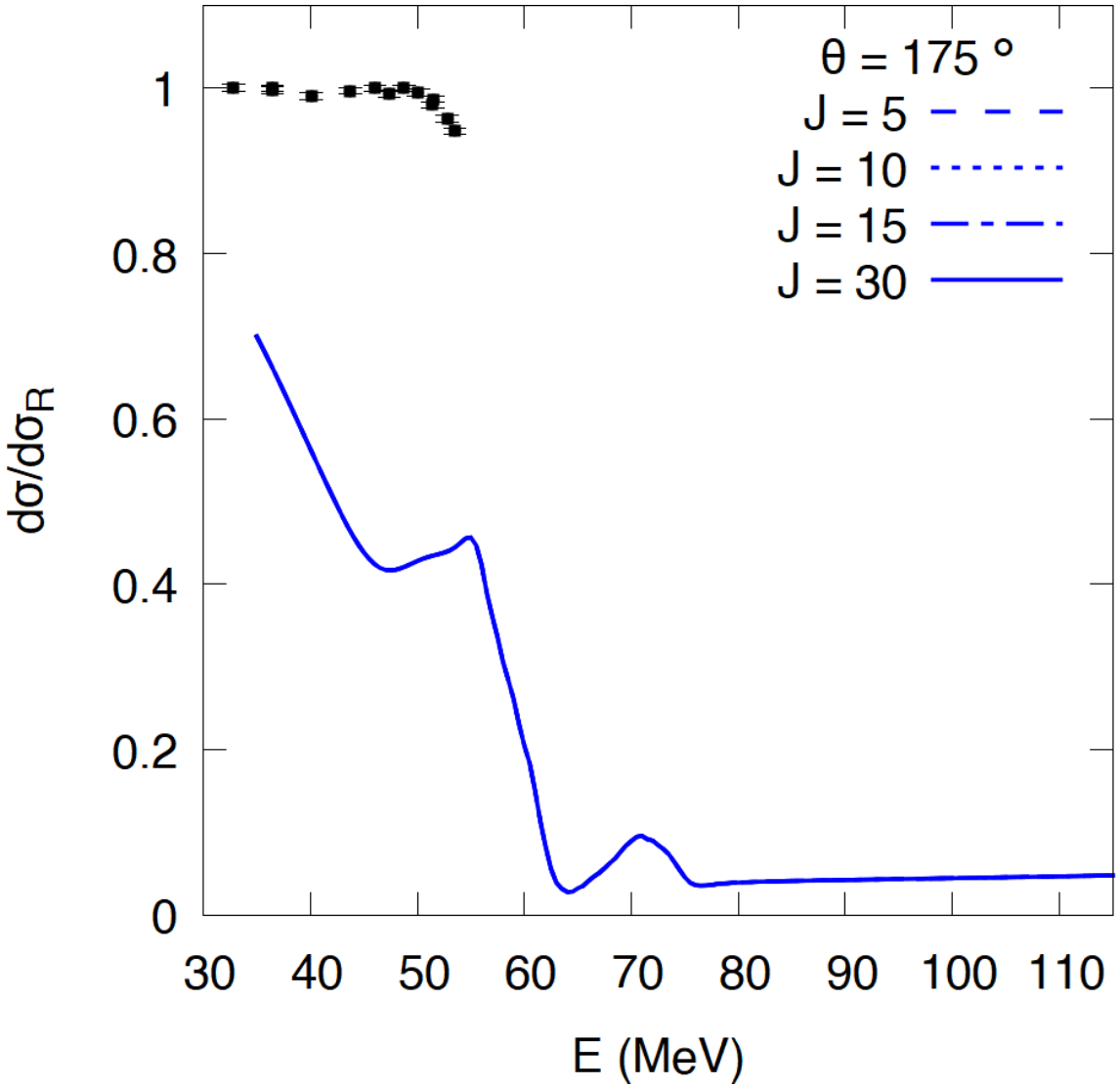

Figure 7.9: Comparison to experimental data of the elastic scattering for $\theta = 175°$ for up to a varying number of partial waves. Results are converged for very low J values, and thus all four data-sets are the same. Experimental data from reference [60].

Table 7.1: Model parameters pertaining to the coupled-channels Hamiltonian for the ^{16}O and ^{152}Sm collision. The Woods-Saxon well depth was chosen to produce the barrier height of 59.53 MeV (the barrier height is from reference [60]). The other Woods-Saxon, imaginary potential, β_4 and coupling radius parameters are from reference [61]. The β_2 and ϵ_2 parameters are from the nuclear data tables in reference [62].

Variable	Value	Description
V_{WS}/MeV	69.5	Woods-Saxon well depth
r_{WS0}/fm	1.20	Woods-Saxon well centre
a_{WS}/fm	0.65	Woods-Saxon well range
ϵ_2/keV	121.7817	Second excited state energy (2^+)
β_2	0.3064	Quadrupole deformation parameter
β_4	0.037	Hexadecapole deformation parameter
r_{coup}/fm	1.1	Rotational coupling radius

7.2 ^{16}O + ^{152}Sm collisions

This section is dedicated to the results from ^{16}O + ^{152}Sm collisions. This will include a comparison of the differential cross sections with both the FRESCO method and experimental data. Table 7.1 contains the coupled-channel parameters for these collisions.

7.2.1 Differential cross sections

Whilst summing partial waves to $J = 30$ gives a good idea of the fusion process, it is not sufficient to explain scattering processes. Therefore we calculate the S-matrix for $J > 30$ to see what effect it has on the differential cross sections. However, the computations are extremely time consuming for $J > 30$, so calculations only up to $J = 45$ have been calculated in the allotted project time. Therefore, whilst experimental data exists for several energies, we only compare our TDCCWP data to the experimental data for $E = 59$ MeV. This is because the results for the inelastic S-matrix elements are closer to convergence, since the reflection probabilities at this energy are approaching zero, which makes the summand in equation (5.2) go to zero.

A comparison between FRESCO, TDCCWP and the experimental differential cross sections is shown in Fig. 7.10. There is a striking resemblance between the differential cross sections for both of the theoretical methods. In fact, from the figure we can see the inelastic differential cross section results for up to $J = 45$ partial waves approximately differ by a multiplicative constant for many angles. This is sensible because the FRESCO calculations do include multiplicative form factors, which can account for the difference. Also, the TDCCWP method produces differential cross

sections several orders of magnitude lower than both FRESCO and the experimental data. This is expected since, without the iso-centrifugal approximation, we expect that at least initially that the spin-orbit interaction will 'pump' the initial 0^+ ground state into the excited states. Whilst the FRESCO results were generated with some parts of the iso-centrifugal approximation, it is not a true iso-centrifugal approximation due to the inclusion of the spin-orbit coupling form factors we discussed before. Overall, the TDCCWP differential cross sections at this level behave qualitatively similar to the FRESCO calculations, and are quantitatively smaller in size which is what we expect without spin-orbit coupling.

7.2.2 Can converged FRESCO calculations explain the experimental data?

Since the two theoretical methods produce similar results, we would like to know if the FRESCO calculations, when they eventually converge, can explain the experimental data. Using FRESCO, we made a calculation including up to $J = 700$ partial waves, shown in Fig. 7.11. Granted, since the FRESCO calculations involved some of the iso-centrifugal approximation, it is not expected to reproduce these results. Nevertheless, Fig. 7.11 shows a reasonable agreement with the experimental data, particularly in determining the inelastic differential cross sections. However, since the iso-centrifugal approximation is meant to perform well when explaining high J values, it is interesting to see that the forward angles are not completely explained when we expect them to be. On the other hand, the FRESCO calculations we have used do not include higher rotational states than the 4^+ in the ground state rotational band, so coupling to higher states such as the 6^+ and 8^+ states may be necessary for better agreement.

7.3 Summary

We observed that our differential cross section results were consistent with results from the TISE and the analytical limits of our differential cross section expression. We used the S-matrix elements to generate the inelastic transition probabilities, which are both a novel result for time-dependent nuclear physics and were able to identify a crossing of the 2^+ and 4^+ levels at $E = 66$ MeV, which was reflected in the differential cross sections. Overall, more partial waves are needed to investigate the differential cross sections, but they are difficult to obtain using our method due to heavily time consuming calculations from the time-dependent method. Upon comparing a fully converged FRESCO calculation to the experimental data, we can see a very good agreement between them. Since the TDCCWP method performs similarly to FRESCO, this gives us hope that the TDCCWP method can perform well in calculating these differential cross sections, subject to using a proper Hamiltonian, and a high number of partial waves to ensure convergence.

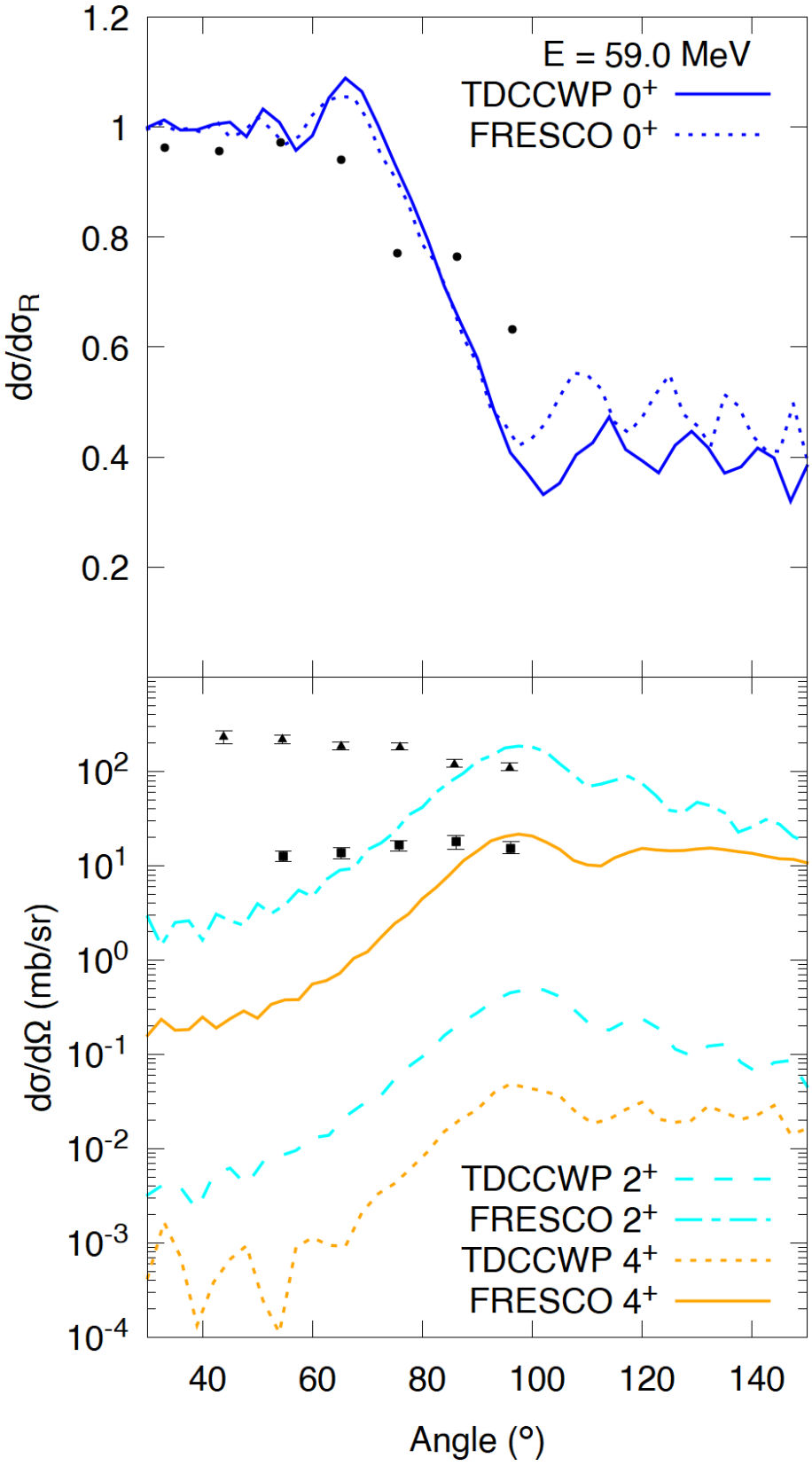

Figure 7.10: TDCCWP and FRESCO differential cross section calculations compared to the experimental data. The results were generated by summing partial waves up to $J = 45$. Experimental 0^+ data are from reference [63], and the 2^+ and 4^+ results are from reference [64].

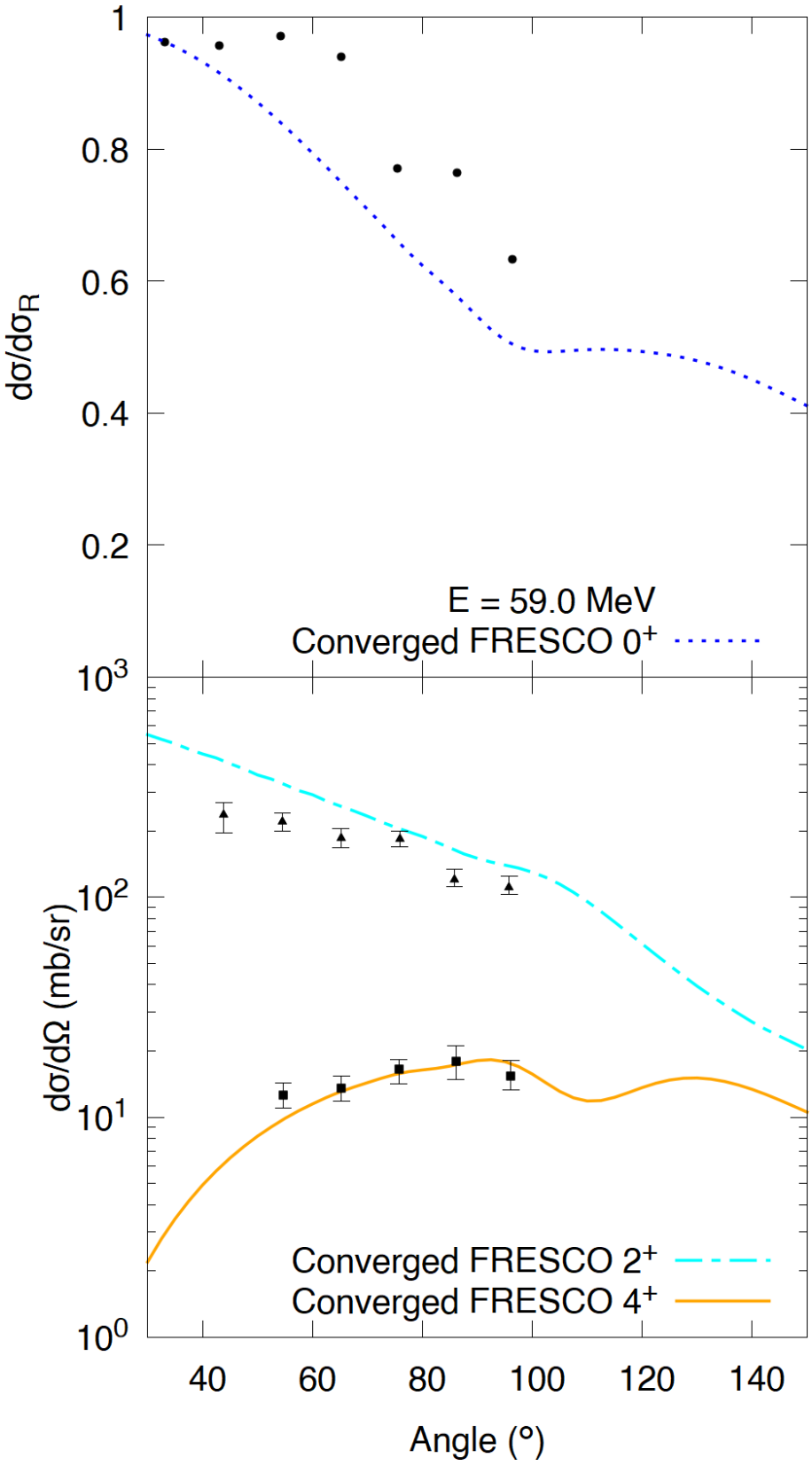

Figure 7.11: Converged FRESCO differential cross section calculations and the experimental data. The results were generated by summing partial waves up to $J = 700$. Experimental 0^+ data are from reference [63], and the 2^+ and 4^+ results are from reference [64].

Chapter 8

Conclusions and future work

The time propagation of the wave-function in chapter 4 successfully reproduced the correct wave-function normalisation and energy conservation before the absorption potential was introduced, indicating that the error in the time propagation was negligible. We began by using the window operator in order to calculate energy resolved quantities, but opted to switch to an S-matrix method, since the S-matrix was needed to calculate the differential cross sections that we wanted to reproduce, and there was concern that the window operator parameters would not allow for accurate energy resolution in every circumstance we wish to simulate.

The TDCCWP method with both the window operator and S-matrix method is able to reproduce transmission coefficients to the similar level as the TISE for a wide range of energies and angular momenta, up to several MeV below the Coulomb barrier. The results for the differential cross sections produced at $E = 59$ MeV for ^{16}O + ^{152}Sm and at $\theta = 175^{\circ}$ for ^{16}O + ^{154}Sm did not reproduce the experimental data. The near converged inelastic differential cross sections for ^{16}O + ^{152}Sm were off by several orders of magnitude. We predict that both of these results will improve with the introduction of spin-orbit coupling, which can provide an increased flux of the inelastic 2^+ and 4^+ states by decreasing the orbital angular momentum L. Decreasing the orbital angular momentum affects the position of the barrier, which can in turn influence the inelastic excitations.

However, there are also other technical issues unrelated to the choice of Hamiltonian that need addressing for the most accurate results. There are two main technical problems that the TDCCWP method faces when trying to reproduce the scattering differential cross sections. The first is the inability to propagate sequentially lower and lower energy wave-packets for accurate low energy S-matrix element generation. These low energy S-matrix elements are needed for all J value terms in equation (5.2). Inaccurate below-barrier calculations are an ongoing problem in nuclear physics and more concentrated effort is needed there. In this work, we attempted an extrapolation method that was justified using the qualitative nature of low incident energy wave-packets, which performs reasonably well compared to the

data from FRESCO. The second problem is that partial waves up to $J = 45$ are insufficient to reproduce the scattering data for ^{16}O + ^{152,154}Sm. Whilst expanding up to this angular momenta is sufficient to describe fusion, we will need to go to higher J values to reproduce scattering data, which is important in giving us a more complete picture of the reaction.

These two problems, if addressed satisfactorily, can provide us with a very powerful time-dependent method to address nuclear reactions. This is because the physical behaviour of the nuclei enter solely through the Hamiltonian, and not through the propagator. Specifically, the calculation of the S-matrix elements can still be performed in the body-fixed frame, and in theory reproduce the space-fixed S-matrix elements for the inert projectile and excitable target; after accounting for Coriolis/tidal effects in both the Hamiltonian and differential cross sections. These are discussed in the future work section below. From this work, we have seen that the TDCCWP method for nuclear physics can reliably expand the complexity of the Hamiltonian without compromising the dynamics, for a range angular momenta that are sufficient to describe the fusion process. This was demonstrated when the number of channels was increased, and the results from the time propagation remained as accurate as the single channel case. The major bottlenecks for this method are in the calculation of observables such as the differential cross sections.

In the future work section below, we will explore ideas that help find the S-matrix elements for higher J values, the theory behind body-fixed spin-orbit coupled dynamics, some of the concepts used in finding potentials to describe MNT in the DNS framework, and finally a powerful dynamical method that can include dissipation into the Hamiltonian, without having to model a density matrix system. With these implementations to the method, we will be able to begin describing more involved fusion scenarios between heavy nuclei that can go on to make SHE. Overall, this is a promising step in the direction towards an accurate few body reaction theory, that can describe a wide range of nuclear physics phenomena in the context of heavy-ion fusion.

8.1 Future work

8.1.1 Artificial neural networks

As we described in Chapter 7, it becomes very difficult to produce results for $J > 45$, which are vital to describe the scattering cross sections fully. This can be addressed by using artificial neural networks (ANN) to learn the pattern between the S-matrix elements and how it varies with changing J [65]. The motivation behind using an ANN is the observation that the S-matrix elements for differing J all share common characteristics, namely - local minima and maxima, as well as the asymptotic behaviour at high and low energies. The extent of similarity can be seen in Fig. 6.21, for instance. The features (inputs) that should be given to the

ANN are properties of the barrier such as barrier height, width and position, as well as the ratios of the energies to the barrier height. For the output layer, the ANN should try and learn the S-matrix elements.

In the case we have considered in this work, semi-classical methods can be useful to check the results of our calculation, since we wish to use the ANN to extrapolate to high angular momenta where semi-classical methods are applicable. We do not suggest using semi-classical methods instead of these methods, because for more involved calculations such as for MNT the TDCCWP codes may break down at a lower angular momenta, which requires a quantum treatment in order to explain.

8.1.2 Spin-orbit coupling Hamiltonian and scattering amplitudes

We introduce the spin-orbit/tidal coupling into the Hamiltonian of equation (2.9) by expressing the orbital angular momentum operator $\hat{L} = \hat{J} - \hat{I}$. The Hamiltonian with this tidal interaction is

$$\hat{H} = \frac{-\hbar^2}{2\mu}\frac{1}{\hat{r}^2}\frac{\partial}{\partial r}\hat{r}^2\frac{\partial}{\partial r} + \frac{(\hat{J}-\hat{I})^2}{2\mu\hat{r}^2} + \frac{\hat{I}^2}{2\mathcal{I}} + \hat{V} + \hat{V}_{\text{coup}}. \tag{8.1}$$

In the space-fixed reference frame, one solves the Schrödinger equation by finding the eigenstate of equation (8.1), which involve a coupling of the spin and orbital angular momentum states via the Clebsch-Gordan coefficients [48]. These calculations can be fairly involved, since one has to consider both the magnetic projections as well as the momentum quantum numbers, for both the spin and the orbital momentum. To describe scattering phenomena in nuclear physics, which requires a high amount of partial waves, these calculations would be very involved even in the time-independent frame-work. Fortunately, serious efforts in the field of quantum chemistry have been made that can reduce this time, using a clever trick to describe the space-fixed states.

The body-fixed states can be described as space-fixed states that have been rotated onto the body-fixed axis, which is equivalent to the axis of the inter-nuclear distance [48]. This leads to an expression of the space fixed states [56]

$$\begin{aligned}\langle \vec{r}_L, \vec{r}_I | \Psi_{\alpha i, m_{I\alpha i}}(t)\rangle = &\sum_{J,I,K} (2J+1) D^J_{K m_{I\alpha i}}(\alpha,\beta,\gamma) \\ &\times Y_{I,K}(\theta, 0)\, \langle r, I, K | \psi_{\alpha i, J}(t)\rangle\,,\end{aligned} \tag{8.2}$$

where $\vec{r}_I$ are the internal coordinates of the target nuclei, D is the Wigner D-matrix, α, β, γ are the Euler angles, $m_{I\alpha i}$ is the initial spin projection number and K is the

projection of I on the body-fixed axis, also known as the tidal spin eigenvalue [66] or simply as the projection number [56]. The tidal spin K ranges from $-\min(J, I)$ to $+\min(J, I)$ [56]. The wave-function $\langle r, I, K|\psi_{\alpha i,J}(t)\rangle$ is like our body-fixed wave-function that we have found in this thesis, except that it depends on this additional tidal projection K. After substituting equation (8.2) in the TDSE, and integrating over the Euler angles, we get an expression for the time dependence of the body-fixed states [56]

$$-i\hbar\frac{\mathrm{d}}{\mathrm{d}t}\langle r, I, K|\psi_{\alpha i,J}(t)\rangle = \sum_{r,I',K'} H^{BF}(r, I, K, I', K', J)\langle r, I', K'|\psi_{\alpha i,J}(t)\rangle \tag{8.3}$$

where

$$\begin{aligned} H^{BF}(r, I, K, I', K', J) = (&\frac{-\hbar^2}{2\mu}\frac{1}{r}\frac{\partial^2}{\partial r^2}r + \frac{\hbar^2(J(J+1) - 2K^2 + I(I+1))}{2\mu r^2} \\ &+ V(r) + \epsilon_I)\delta_{II'}\delta_{KK'} \\ &+ V_{II'}(r)\delta_{KK'} \\ &+ \frac{-\hbar^2}{2\mu r^2}(\lambda_+(J, K)\lambda_+(I, K)\delta_{II'}\delta_{K+1K'} \\ &+ \lambda_-(J, K)\lambda_-(I, K)\delta_{II'}\delta_{K-1K'}), \end{aligned} \tag{8.4}$$

and

$$\lambda_\pm(J, K) = \sqrt{(J \pm K + 1)(J \mp K)}. \tag{8.5}$$

We can solve equation (8.3) using the same numerical recipes used in this thesis, by including an extra basis in K. The space-fixed S-matrix is given by [56]

$$\begin{aligned} S^{SF}_{\beta\alpha}(E, J, L) = &\sum_{m_{I_{\alpha i}},K} \sqrt{2L+1}\sqrt{2L_{\alpha i}+1} \times (-1)^{K+m_{I_{\alpha i}}} \\ &\times \begin{pmatrix} L_{\alpha i} & I_{\alpha i} & J \\ 0 & m_{I_{\alpha i}} & -m_{I_{\alpha i}} \end{pmatrix} \begin{pmatrix} L & I_{\beta f} & J \\ 0 & K & -K \end{pmatrix} S^{BF}_{\beta\alpha}(E, J, K), \end{aligned} \tag{8.6}$$

which is the general form of the expression we used to calculate the space-fixed matrix elements in equation (5.7). For the inert projectile and for no change in mass of the target and projectile after the reaction, the differential cross sections are given by [59]

$$\frac{\mathrm{d}\sigma_{\beta\alpha}(E,\theta)}{\mathrm{d}\Omega} = \frac{1}{(2I_{\beta f}+1)} \sum_{M_\beta, M_\alpha} \left| f_{M_\beta : M_\alpha}(E,\theta) \right|^2, \tag{8.7}$$

where

$$f_{M_\beta : M_\alpha}(E,\theta) = \delta_{I_{\alpha i} I_{\beta f}} f_c(\theta) + \sum_{L_{\beta f}} A^{L_{\beta f}}_{M_\beta : M_\alpha} P^{M_\beta - M_\alpha}_{L_{\beta f}}(\cos(\theta)), \tag{8.8}$$

and

$$\begin{aligned} A^{L_{\beta f}}_{M_\beta : M_\alpha} = - \sum_{L_{\alpha i}, J, M_{L_{\beta f}}} & \langle L_{\alpha i} 0 I_{\alpha i} M_\alpha | J M_\alpha \rangle \left\langle L_{\beta f} M_{L_{\beta f}} I_{\beta f} M_\beta \middle| J M_\alpha \right\rangle \\ & \frac{2\pi}{\mathrm{i} k_{\alpha i}} \sqrt{\frac{k_{\beta f}}{k_{\alpha i}}} \exp(\mathrm{i}(\sigma_{\alpha, L_{\alpha i}} - \sigma_{\alpha,0})) \exp\big(\mathrm{i}(\sigma_{\beta, L_{\beta f}} - \sigma_{\beta,0})\big) \\ & (\delta_{\alpha\beta} - S^{SF}_{\beta\alpha}(E, J, L_{\beta f})) \sqrt{\frac{2L_{\alpha i}+1}{4\pi}} Y_c(L_{\beta f}, M_{L_{\beta f}}). \end{aligned} \tag{8.9}$$

where

$$Y^M_L(\theta,\phi) = Y_c(L,M) P^{|M|}_L(\cos(\theta)) \exp(\mathrm{i} M \phi). \tag{8.10}$$

If $I_{\alpha i} = 0$ like in our calculations, then $M_\alpha = 0$, and therefore $\langle L_{\alpha i} 0 I_{\alpha i} M_\alpha | J M_\alpha \rangle = \langle L_{\alpha i} 000 | J 0 \rangle = \delta_{L_{\alpha i} J}$, which allows us to eliminate the sums over both M_α and $L_{\alpha i}$. This yields the expression for the differential cross section

$$\frac{\mathrm{d}\sigma_{\beta\alpha}(E,\theta)}{\mathrm{d}\Omega} = \frac{1}{(2I_{\beta f}+1)} \sum_{M_\beta} \left| f_{M_\beta ; \alpha}(E,\theta) \right|^2, \tag{8.11}$$

where

$$f_{M_\beta ; \alpha}(E,\theta) = \delta_{\alpha\beta} f_c(\theta) + \sum_{L_{\beta f}} A^{L_{\beta f}}_{M_\beta ; \alpha} P^{M_\beta}_{L_{\beta f}}(\cos(\theta)), \tag{8.12}$$

and

$$A^{L_{\beta f}}_{M_\beta;\alpha} = -\sum_{J,M_{L_{\beta f}}} \left\langle L_{\beta f} M_{L_{\beta f}} I_{\beta f} M_\beta \middle| J M_\alpha \right\rangle \frac{2\pi}{\mathrm{i}k_{\alpha i}} \sqrt{\frac{k_{\beta f}}{k_{\alpha i}}} \exp(\mathrm{i}(\sigma_{\alpha,J} - \sigma_{\alpha,0})) \exp\big(\mathrm{i}(\sigma_{\beta,L_{\beta f}} - \sigma_{\beta,0})\big) (\delta_{\alpha\beta} - S^{SF}_{\beta\alpha}(E, J, L_{\beta f})) \sqrt{\frac{2J+1}{4\pi}} Y_c(L_{\beta f}, M_{L_{\beta f}}). \tag{8.13}$$

Although equation (8.13) assumes that the projectile is inert and the target starts in a spin 0 state, it can be generalised for any initial state and for a rotationally excitable projectile too [59]. However, we are not currently aware of a published extension to the body-fixed Hamiltonian method that incorporates the excitable projectile. Nor are we currently aware of the form of the coupled-channel potentials for target-projectile-orbit spin coupling in the nuclear physics context. This will need to be studied in further detail in order to fully generalise the model.

8.1.3 DNS and MNT

A potential that is dependent on the inter-nuclear distance r, the excitation levels and the mass asymmetry coordinate can be generated by re-normalising the sum of single particle energies from the asymmetric TCSM [67]. These potentials have a vanishing r dependence as $r \to \infty$, and for $r \to 0$ the mass asymmetry varies without changing r or the excitation levels (at least in general) [67].

In order to calculate the mass asymmetry, the two nuclei are divided into two regions - the projectile region and the target region. The mass asymmetry is then calculated by integrating over the many-body wave-function in each region [67], i.e.

$$\eta = \langle \psi | \, \hat{\epsilon} \, | \psi \rangle \,, \tag{8.14}$$

where

$$\hat{\epsilon} = \frac{1}{A_P + A_T} \left(\int_{\mathrm{Region}P} \hat{\rho}(\vec{r}) \mathrm{d}^3 x - \int_{\mathrm{Region}T} \hat{\rho}(\vec{r}) \mathrm{d}^3 x \right), \tag{8.15}$$

where regions P and T are the projectile and target regions respectively, and $\hat{\rho}(\vec{r})$ is the many-body density operator. This potential can then be used in our time-dependent method to model MNT reactions.

More modern advances have been made in the TCSM, which are based on using two spherical Woods-Saxon potentials, instead of two harmonic oscillator potentials

[68, 69]. For example, the TCSM potential experienced by neutrons can be written as [68, 69]

$$\hat{V}_{\rm TCSM}^{\rm neutrons} = \sum_{{\rm N}\in\{T,P\}} \exp\Big(-{\rm i}\hat{r}_{\rm N}\hat{k}\Big)\hat{V}_{\rm N}\exp\Big({\rm i}\hat{r}_{\rm N}\hat{k}\Big), \tag{8.16}$$

where N is either the target or projectile, $\hat{r}_{\rm N}$ is the location of the centre of nuclei N, $\hat{k}$ is the single particle reciprocal distance operator, and $\hat{V}_{\rm N}$ is a Woods-Saxon potential including single particle spin-orbit coupling, i.e.

$$\hat{V}_{\rm N}(r) = -V_0^{\rm N}\left(f^{\rm N}(r) - \frac{\kappa_{\rm N}}{r}\frac{{\rm d}f_{\rm SO}^{\rm N}(r)}{{\rm d}r}\left(\vec{l}_{\rm N}\cdot\vec{s}_{\rm N}\right)\right), \tag{8.17}$$

where $-V_0^{\rm N}$ is the Woods-Saxon well strength, $\kappa_{\rm N}$ is the strength of the spin-orbit coupling, and $f^{\rm N}(r)$ is a dimensionless Woods-Saxon potential given by

$$f^{\rm N}(r) = \frac{1}{1+\exp\left((r-r_0^{\rm N}A_{\rm N}^{1/3})/a_0^{\rm N}\right)}, \tag{8.18}$$

and similarly for $f_{\rm SO}^{\rm N}(r)$. The single particle potential operators $\hat{V}_{\rm N}$ are expanded in a truncated single particle oscillator basis [68,69], which has the radial wave-functions $\langle r|nl\rangle = h_{\rm osc}^{3/2}\Phi_{nl}(x)$, where $x = r/h_{\rm osc}$, $h_{\rm osc} = 0.84r_0^{\rm N}A_{\rm N}^{1/6}$ fm [69], and

$$\Phi_{nl}(x) = \sqrt{\frac{2n!}{\Gamma(n+l+3/2)}}x^l\exp\left(\frac{-x^2}{2}\right){\rm L}_n^{l+1/2}(x^2), \tag{8.19}$$

where ${\rm L}_n^{l+1/2}(x^2)$ is a Laguerre polynomial. The momentum wave-functions are given by $\langle k|nl\rangle = (-1)^n({\rm i})^l h_{\rm osc}^{3/2}\Phi_{nl}(\xi)$, where $\xi = h_{\rm osc}k$. Using this basis, the operator $\hat{V}_{\rm N}$ can be approximated as [68, 69]

$$\hat{V}_{\rm N} \approx \sum_{\mu,\nu\in\{nljm\}} |{\rm N},\mu\rangle\, V_{\mu\nu}^{\rm N}\,\langle {\rm N},\nu|\,, \tag{8.20}$$

where $V_{\mu\nu}^{\rm N} = \langle {\rm N},\mu|\,\hat{V}_{\rm N}\,|{\rm N},\nu\rangle$. The solution to the TCSM problem is the solution to [68, 69]

$$\sum_{\mu'\in\{nljm\}}\sum_{{\rm N}'\in\{T,P\}}\left[\delta_{{\rm N}{\rm N}'}\delta_{\mu\mu'} - \sum_{\nu\in\{nljm\}}\langle {\rm N},\mu|\,G_0(E)\exp\Big({\rm i}(\hat{r}_{\rm N}-\hat{r}_{{\rm N}'})\hat{k}\Big)\Big|{\rm N}',\nu\Big\rangle\, V_{\nu\mu'}^{{\rm N}'}\right]A_{{\rm N}'\mu'} = 0, \tag{8.21}$$

where $G_0(E)$ is the free Green's propagator for single particles, given by

$$G_0(E) = \left(E - \frac{\hbar^2 \hat{k}^2}{2m_0} \right)^{-1} \tag{8.22}$$

where m_0 is the single particle mass, and

$$A_{\mathrm{N}\mu} = \langle \mathrm{N}, \mu | \exp\left(\mathrm{i}\hat{r}_{\mathrm{N}} \hat{k} \right) | \varphi \rangle \,, \tag{8.23}$$

where

$$|\varphi\rangle = G_0(E) \sum_{\mu,\nu \in \{nljm\}} \sum_{\mathrm{N} \in \{T,P\}} V^{\mathrm{N}}_{\mu\nu} A_{\mathrm{N}\nu} \exp\left(-\mathrm{i}\hat{r}_{\mathrm{N}} \hat{k} \right) |\mathrm{N}, \mu\rangle \,. \tag{8.24}$$

These states are used to generate the TCSM potentials for varying A_T and A_P, which can be linked to the mass asymmetry coordinate. The OWL code in reference [69] is available for this purpose.

8.1.4 Stochastic surrogate Hamiltonian (dynamical dissipation)

The absorption potential quickly dissipates and destroys all of the quantum information inside the fusion region for the sake of preventing the penetrated flux from escaping and affecting the scattering data. If we are interested in looking at the fusion mechanism for times after barrier penetration, we can circumvent this limitation by replacing the absorption potential with dynamical dissipation. In this case, the dissipators/oscillator bath and their interaction with the environment are intended to simulate the interaction between the collective degrees of freedom of our Hamiltonian with the non-collective, such as single particle motion. The process should be Markovian (i.e. no fluctuations into the collective degrees of freedom from non-collective [39]), since for heavy ion collisions the number of non-collective degrees of freedom vastly outnumbers the collective, so it is statistically unlikely that fluctuations of this type can occur. As discussed before in section 1.5.3, dynamical dissipation is often included in time-dependent density matrix methods, which are computationally expensive due to the increased dimensions of the density matrix relative to a wave-function.

One method that can be used to model dynamical friction using a wave-function is the stochastic surrogate Hamiltonian method [70]. Instead of coupling the collective system to the entirety of the non-collective/bath degrees of freedom, the collective system can interact with a subset of said bath. This subset is known as the primary

bath, which is typically a set of two level systems with some frequency ω_j [70]. The primary bath may then interact further with a secondary bath, which does not interact with the collective system. The computational efficiency is gained by modelling the interaction of only the system and primary bath, and effectively modelling the primary-secondary bath interaction by swapping the primary and secondary bath states at random times [70, 71]. This is commonly achieved by replacing the phase of a swapped primary bath oscillator with a random phase [70, 71]. A swap occurs when [71]

$$\exp(-\Gamma_j \Delta t_j) < \mathbb{P}_j^{\text{swap}}, \tag{8.25}$$

where $\mathbb{P}_j^{\text{swap}}$ is the stochastic probability of swapping for the j^{th} oscillator, Δt_j is the amount of time since the last swap, and Γ_j is the swap rate. In order to stochastically swap the primary and secondary bath states, $\mathbb{P}_j^{\text{swap}}$ is set to a random number on initialisation and after a swap occurs [71]. The swap rate is expressed as [71]

$$\Gamma_j = \tau_j J(\omega_j), \tag{8.26}$$

where τ_j is the life-time of the j^{th} bath mode and $J(\omega)$ is the spectral density. The value of τ_j controls the extent of Markovianity of the propagation, with high life-times leading to non-Markovian dynamics, and low life-times to Markovian [71].

Using a time propagator with the stochastic surrogate Hamiltonian leads to the generation of a stochastic state $\left|\psi^{(n)}(t)\right\rangle$. The density matrix of the collective system is then given by [70]

$$\hat{\rho}(t) = \text{Tr}_B \left(\frac{1}{N_s} \sum_{n=1}^{N_s} \left|\psi^{(n)}(t)\right\rangle \left\langle\psi^{(n)}(t)\right| \right), \tag{8.27}$$

where Tr_B denotes the partial trace over the primary bath and N_s is the total number of stochastic states. In the limit $N_s \to \infty$, the density matrix produced equation (8.27) for a Markovian system is equivalent to that from Lindblad dynamics.

Appendix A

Chebyshev polynomial propagator

This appendix is dedicated to a mathematical derivation and motivation of the Chebyshev polynomial series for the curious reader, followed by the application of the polynomial series to the problem of quantum dynamics. For those who are solely interested in the form of the time propagator that we are using, see sections A.3 and beyond.

A.1 Derivation of the Chebyshev polynomial series

This derivation follows the work in reference [72]. Suppose you have a analytical function $f(x)$ with a domain $x \in \mathbb{I} = [-1, 1]$ (this domain is known as the unit interval). We would like to use a series expansion of $f(x)$. A very general series expansion we may consider is the Laurent series. However, we cannot directly use a Laurent series expansion of $f(x)$, because the domain of the Laurent series is the unit circle in the complex plane $\mathbb{U}$.

A.1.1 Joukowsky map

Consider the map $M_{\mathrm{J}} : \mathbb{U} \mapsto \mathbb{I}$ that maps the unit circle in the complex plane $\mathbb{U}$ to the unit interval $\mathbb{I}$, which is defined as [72]

$$M_{\mathrm{J}}(z) = \frac{1}{2}\left(z + \frac{1}{z}\right), \tag{A.1}$$

for $z \in \mathbb{U} \subset \mathbb{C}$. This is known as the Joukowsky map. We note that for $z \in \mathbb{U}, z^* = \frac{1}{z}$, and

$$M_{\mathrm{J}}(z^*) = \frac{1}{2}\left(\frac{1}{z} + z\right) = M_{\mathrm{J}}(z). \tag{A.2}$$

We are interested in looking at the inverse map $M_{\mathrm{J}}^{-1} : \mathbb{I} \mapsto \mathbb{U}$, which will allow us to map values of x to values of z, which can then be used in a Laurent series expansion. Since $M_{\mathrm{J}}(z)$ has exactly two elements in $\mathbb{U}$ mapping to one in $\mathbb{I}$ (from equation (A.2)), it will have two inverse maps. By setting $M_{\mathrm{J}}(z) = x$, we rearrange to find

$$z^2 - 2xz + 1 = 0, \tag{A.3}$$

$$\Rightarrow z_{\pm} = x \pm \sqrt{x^2 - 1} = M_{\mathrm{J}\pm}^{-1}(x). \tag{A.4}$$

For the remainder of this derivation, we will carry out the expansion using the inverse map $M_{\mathrm{J}-}^{-1}(x)$.

A.1.2 Constructing the polynomial series

Consider the analytical function $f(x)$ that has a domain $x \in \mathbb{I}$, which has the same values as the function $g(z)$ that has a domain $z \in \mathbb{U}$. To re-iterate, we wish to map the values of x to values of z, and then use these values of z in a Laurent series. We define [72]

$$f(x) \equiv g(z) = \sum_{m=-\infty}^{\infty} g_m z^m, \tag{A.5}$$

where we have expanded $g(z)$ using the Laurent series, and g_m are the Laurent series coefficients given by [72]

$$g_m = \frac{1}{2\pi \mathrm{i}} \oint g(z) z^{-m-1} \mathrm{d}z. \tag{A.6}$$

Note that since the Joukowsky map is analytical, the analyticity of $g(z)$ originates from $f(x)$ in general, so in our case since $f(x)$ is analytical, $g(z)$ is analytical as well. Substituting $z = M_{\mathrm{J}-}^{-1}(x)$ into equation (A.5) yields

$$g(M_{\mathrm{J}-}^{-1}(x)) = \sum_{m=-\infty}^{\infty} g_m \left(M_{\mathrm{J}-}^{-1}(x)\right)^m. \tag{A.7}$$

Equation (A.7) is the expression we will expand to yield the Chebyshev expression. Firstly, we can simplify the sum via g_m by noting

$$g(z) = f(M_{\mathrm{J}}(z)) = f(M_{\mathrm{J}}(\frac{1}{z})) = g(\frac{1}{z}), \tag{A.8}$$

using the property from equation (A.2). If we define $\xi = \frac{1}{z}$, we can see that

$$\begin{aligned} g_m &= \frac{1}{2\pi \mathrm{i}} \oint g(z) z^{-m-1} \mathrm{d}z \\ &= \frac{-1}{2\pi \mathrm{i}} \oint g(\frac{1}{\xi})(\frac{1}{\xi})^{-m-1} \frac{\mathrm{d}\xi}{\xi^2} \\ &= \frac{1}{2\pi \mathrm{i}} \oint g(\xi)(\xi)^{m+1-2} \mathrm{d}\xi \\ &= \frac{1}{2\pi \mathrm{i}} \oint g(\xi)(\xi)^{m-1} \mathrm{d}\xi \\ &= g_{-m}. \end{aligned} \tag{A.9}$$

Here we have absorbed the minus sign since the contour integration is closed. Using the result of (A.9) in (A.7) yields

$$g(M_{\mathrm{J}-}^{-1}(x)) = g_0 + \sum_{m=1}^{\infty} g_m \left(\left(M_{\mathrm{J}-}^{-1}(x)\right)^m + \left(M_{\mathrm{J}-}^{-1}(x)\right)^{-m} \right). \tag{A.10}$$

By using $M_{\mathrm{J}\pm}^{-1}(x) = x \pm \sqrt{x^2 - 1} = x \pm i\sqrt{1 - x^2}$, we can show that $\left(M_{\mathrm{J}-}^{-1}(x)\right)^m + \left(M_{\mathrm{J}-}^{-1}(x)\right)^{-m}$ is a polynomial of order m for $m > 0$

$$\begin{aligned} \left(M_{\mathrm{J}-}^{-1}(x)\right)^m &= \left(x - i\sqrt{1-x^2}\right)^m = \sum_{j=0}^{m} (-i)^j \binom{m}{j} x^{m-j} (\sqrt{1-x^2})^j, \\ \left(M_{\mathrm{J}-}^{-1}(x)\right)^{-m} &\equiv \left(M_{J+}^{-1}(x)\right)^m = \sum_{j=0}^{m} (i)^j \binom{m}{j} x^{m-j} (\sqrt{1-x^2})^j, \\ \Rightarrow \left(M_{\mathrm{J}-}^{-1}(x)\right)^m + \left(M_{\mathrm{J}-}^{-1}(x)\right)^{-m} &= 2x^m + 2 \sum_{j=1}^{\lfloor m/2 \rfloor} (-1)^j \binom{m}{j} x^{m-2j} (1-x^2)^j, \end{aligned} \tag{A.11}$$

since the odd j terms in the $\left(M_{\mathrm{J}\pm}^{-1}(x)\right)^m$ sums cancel out during the addition. Note that the middle equation of (A.11) used the property $M_{\mathrm{J}-}^{-1}(x) M_{\mathrm{J}+}^{-1}(x) = 1$. Now, we define these polynomials as

$$T_m(x) \equiv \frac{\left(M_{\mathrm{J}-}^{-1}(x)\right)^m + \left(M_{\mathrm{J}-}^{-1}(x)\right)^{-m}}{2}, \tag{A.12}$$

$$\Rightarrow f(x) = g_0 + \sum_{m=1}^{\infty} 2g_m T_m(x) = \sum_{m=0}^{\infty} f_m T_m(x), \tag{A.13}$$

where $f_m = (2 - \delta_{m0})g_m$ and δ_{m0} is the Kronecker delta. The polynomials $T_m(x)$ are known as the Chebyshev polynomials. The first two polynomials and their recurrence relation are given by

$$T_0(x) = 1, \tag{A.14}$$
$$T_1(x) = x, \tag{A.15}$$
$$T_m(x) = 2xT_{m-1}(x) - T_{m-2}(x). \tag{A.16}$$

With this simple recurrence relation, the remaining work to approximate the function $f(x)$ is calculating the contour integrals in the coefficients f_m.

A.2 Chebyshev series of a complex exponential

Consider the complex number function $f(x) = \exp(\mathrm{i}\alpha x)$, where $\alpha \in \mathbb{R}$. We would like to know the coefficients of the expansion f_m, which involve the g_m integral from equation (A.6). Using the Joukowsky map $M_{\mathrm{J}}(z) = x$, we can express $g(z)$ as [72]

$$g(z) = f(x) = f(M_{\mathrm{J}}(z)) = \exp\left(\frac{\mathrm{i}\alpha}{2}(z + \frac{1}{z})\right) \tag{A.17}$$

Now consider

$$\begin{aligned} \frac{\mathrm{i}\alpha}{2}(z + \frac{1}{z}) &= \frac{\alpha}{2}(\mathrm{i}z + \frac{\mathrm{i}}{z}) \\ &= \frac{\alpha}{2}(\mathrm{i}z - \frac{1}{\mathrm{i}z}) \\ &= \frac{\alpha}{2}(z' - \frac{1}{z'}), \end{aligned} \tag{A.18}$$

where $z' = \mathrm{i}z$. Changing variables from z to z' leads to the following integral for g_m

$$
\begin{aligned}
g_m &= (-\mathrm{i})^{-m} \frac{1}{2\pi \mathrm{i}} \oint \exp\left(\frac{\alpha}{2}(z' - \frac{1}{z'})\right) z'^{-m-1} \mathrm{d}z' \\
&= \mathrm{i}^m J_m(\alpha),
\end{aligned}
\tag{A.19}
$$

where J_m are the Bessel functions of the first kind, a prominent and well studied set of mathematical equations. Thus, $f_m = (2 - \delta_{m0}) i^m J_m(\alpha)$ and from (A.13) we have the result

$$
\exp(\mathrm{i}\alpha x) = \sum_{m=0}^{\infty} (2 - \delta_{m0}) i^m J_m(\alpha) T_m(x). \tag{A.20}
$$

The power behind this choice of polynomial basis for complex number functions is realised once one considers the coefficients f_m. For $m > \alpha$, the Bessel functions exponentially decay, so f_m decays too and thus the series converges. The series can be effectively truncated, provided that the final value of the summation index m is some amount greater than α.

We can replace the variable x with an operator $\hat{x}$, provided that the eigenvalues of the operator $\hat{x}$ lie in the domain $\mathbb{I}$. This allows us to express functions of operators with a Chebyshev series, such as the quantum mechanical time propagator.

A.3 Quantum mechanical time propagator

Consider a time independent Hamiltonian $\hat{H}$. The time propagator that takes a state from a time t to $t + \Delta t$ is given by [73]

$$
\hat{U}(t + \Delta t, t) = \exp\left(\frac{-i\hat{H}\Delta t}{\hbar}\right), \tag{A.21}
$$

In this form, we cannot use the Chebyshev expansion. This is because, in general, the Hamiltonian has eigenvalues that lie outside of the domain of the Chebyshev series. We can scale the Hamiltonian using the normalised Hamiltonian $\hat{H}_{\mathrm{norm}}$ [74]

$$
\hat{H}_{\mathrm{norm}} = \frac{H_+ \hat{I} - \hat{H}}{H_-}, \tag{A.22}
$$

where

$$
H_\pm = \frac{\lambda_{\max} \pm \lambda_{\min}}{2} \tag{A.23}
$$

and $\lambda_{\max}, \lambda_{\min}$ are the maximum and minumum eigenvalues of $\hat{H}$ respectively. This ensures the eigenspectra of $\hat{H}_{\text{norm}}$ is within the domain of the Chebyshev polynomials. After some rearrangement we find

$$\begin{aligned}\hat{U}(t+\Delta t,t) &= \exp\left(\frac{-\mathrm{i}(H_+\hat{I}-H_-\hat{H}_{\text{norm}})\Delta t}{\hbar}\right)\\ &= \exp\left(\frac{-\mathrm{i}H_+\hat{I}\Delta t}{\hbar}\right)\exp\left(\frac{\mathrm{i}H_-\hat{H}_{\text{norm}}\Delta t}{\hbar}\right)\\ &= \exp\left(\frac{-\mathrm{i}H_+\Delta t}{\hbar}\right)\exp\Big(\mathrm{i}\alpha\hat{H}_{\text{norm}}\Big),\end{aligned} \tag{A.24}$$

where $\alpha = \frac{H_-\Delta t}{\hbar}$, and we have simplified the first exponential. Using the result derived in (A.20) we can express the second exponential in equation (A.24) as

$$\exp\Big(\mathrm{i}\alpha\hat{H}_{\text{norm}}\Big) = \sum_{m=0}^{\infty}(2-\delta_{m0})\mathrm{i}^m J_m(\alpha)T_m(\hat{H}_{\text{norm}}). \tag{A.25}$$

Putting it all together, we have

$$\hat{U}(t+\Delta t,t) = \exp\left(\frac{-\mathrm{i}H_+\Delta t}{\hbar}\right)\sum_{m=0}^{\infty}(2-\delta_{m0})\mathrm{i}^m J_m(\frac{H_-\Delta t}{\hbar})T_m(\hat{H}_{\text{norm}}). \tag{A.26}$$

A.4 Absorbative quantum propagator - modified Chebyshev method

The propagator in equation (A.26) is a unitary operator, and should conserve the wave-function norm for all times to a high degree of accuracy. When we change the closed system to an open one, the propagator for the relevant degrees of freedom is no longer unitary in general. With an open system Hamiltonian like this, we no longer conserve the norm of the wave-function, and thus we cannot use the propagator we have derived above to describe its dynamics. For example, in this work we focus on including an absorption potential in order to explain the phenomenon of nuclear fusion, and thus our Hamiltonian has the form $\hat{H}_{\text{CRM}} = \hat{H}_{\text{CRM0}} + \hat{H}_{\text{op}} = \hat{H}_{\text{CRM0}} + \mathrm{i}\hat{W}$, where $\hat{H}_{\text{CRM0}}$ is our baseline nuclear collective radial motion Hamiltonian and $\hat{H}_{\text{op}}$ is an optical potential.

Following the work of V. A. Mandelshtam and H. S. Taylor [75], we find that we can build the effect of an absorption potential into the Chebyshev propagator by using

damping factors. These take into account the effect of the optical potential exactly, and uses only the baseline Hamiltonian $\hat{H}_{\mathrm{CRM0}}$ in the Chebyshev expansion, which ensures the domains match. We introduce a family of polynomials $\{Q_m\}$ with the following recurrence relation

$$Q_0(\hat{x}) = \hat{I}, \tag{A.27}$$
$$Q_1(\hat{x}) = \mathrm{e}^{-\hat{\gamma}}\hat{x}, \tag{A.28}$$
$$Q_m(\hat{x}) = \mathrm{e}^{-\hat{\gamma}}(2\hat{x}Q_{m-1}(\hat{x}) - \mathrm{e}^{-\hat{\gamma}}Q_{m-2}), \tag{A.29}$$

where $\hat{\gamma}$ is the damping operator that is related to the optical potential. When using these damping factors, a calculation of the Green's function of the absorbative system using the modified Chebyshev polynomials yields the relationship between $\hat{\gamma}$ and $\hat{H}_{\mathrm{op}}$ [75]

$$\hat{H}_{\mathrm{op}} = H_- \left(\cos(\Theta)(1 - \cosh(\hat{\gamma})) - \mathrm{i}\sin(\Theta)\sinh(\hat{\gamma})\right), \tag{A.30}$$

where

$$\Theta = \arccos\left(\frac{E_i - H_+}{H_-}\right), \tag{A.31}$$

and E_i is the energy of the initial state being propagated. For our choice of $\hat{H}_{\mathrm{op}} = \mathrm{i}\hat{W}$, we can ignore the real part and solve the imaginary part of (A.30) to obtain $\hat{\gamma}$. The absorbative time propagator is given by

$$\hat{U}(t + \Delta t, t) = \exp\left(\frac{-\mathrm{i}H_+\Delta t}{\hbar}\right)\sum_{m=0}^{\infty}(2 - \delta_{m0})\mathrm{i}^m J_m(\frac{H_-\Delta t}{\hbar})Q_m(\hat{H}_{\mathrm{norm}}). \tag{A.32}$$

where

$$\hat{H}_{\mathrm{norm}} = \frac{H_+\hat{I} - \hat{H}_{\mathrm{CRM0}}}{H_-}, \tag{A.33}$$

and

$$H_\pm = \frac{\lambda_{\max} \pm \lambda_{\min}}{2}, \tag{A.34}$$

where $\lambda_{\max}, \lambda_{\min}$ are the maximum and minimum eigenvalues of $\hat{H}_{\text{CRM0}}$ respectively. If the optical potential is not present, then from equation (A.30) we can see that the operator $\hat{\gamma}$ becomes null, and then the time propagator in equation (A.32) becomes identical to that of equation (A.26).

Appendix B

Derivation of the body-fixed Hamiltonian (extra details)

This appendix includes the remainder of the derivation of the body-fixed Hamiltonian from chapter 2.2. We begin by repeating equation (2.7), and replace the orbital angular momentum L with the total angular momentum J as per the iso-centrifugal approximation, which yields

$$\Psi_{n,J}^{m_J}(r,\theta,\phi) = R_{n,J}(r)Y_J^{m_J}(\theta,\phi). \tag{B.1}$$

Now we can expand and simplify the expression for $\langle\vec{r}|\,\hat{H}\,\left|\Psi_{n,J}^{m_J}\right\rangle$, in order to remove the angular dependence

$$\begin{aligned}\langle\vec{r}|\,\hat{H}\,\left|\Psi_{n,J}^{m_J}\right\rangle =& \frac{-\hbar^2}{2\mu}\frac{1}{r^2}\frac{\partial}{\partial r}\left(r^2\frac{\partial R_{n,J}(r)}{\partial r}\right)Y_J^{m_J}(\theta,\phi)\\ &+\left(\frac{J(J+1)\hbar^2}{2\mu r^2}+V(r)+\epsilon_n\right)R_{n,J}(r)Y_J^{m_J}(\theta,\phi)\\ &+\sum_{n'}V_{nn'}(r)R_{n',J}(r)Y_J^{m_J}(\theta,\phi)\\ &=E_\Psi\left\langle\vec{r}\middle|\Psi_{n,J}^{m_J}\right\rangle,\end{aligned} \tag{B.2}$$

where $V_{nn'}(r) = \langle r, I_n|\,\hat{V}_{\text{coup}}\,|r, I_{n'}\rangle$ and $\epsilon_n = \frac{I_n(I_n+1)\hbar^2}{2\mathcal{I}}$ from the rigid rotor model [3]. We can divide out the angular dependent part $Y_J^{m_J}(\theta,\phi)$ out of equation (B.2) which yields

$$\begin{aligned}\frac{\langle \vec{r}| \hat{H} \left|\Psi_{n,J}^{m_J}\right\rangle}{Y_J^{m_J}(\theta,\phi)} =& \frac{-\hbar^2}{2\mu}\frac{1}{r^2}\frac{\partial}{\partial r}\left(r^2\frac{\partial R_{n,J}(r)}{\partial r}\right) + \left(\frac{J(J+1)\hbar^2}{2\mu r^2} + V(r) + \epsilon_n\right) R_{n,J}(r) \\ &+ \sum_{n'} V_{nn'}(r) R_{n',J}(r) \\ &= E_\Psi R_{n,J}(r),\end{aligned} \tag{B.3}$$

Substituting $\psi_{n,J}(r) = rR_{n,J}(r)$ into equation (B.3) and multiplying by r, we find that

$$\begin{aligned}E_\Psi \psi_{n,J}(r) = & \frac{-\hbar^2}{2\mu}\frac{1}{r}\frac{\partial}{\partial r}\left(r^2\frac{\partial}{\partial r}\left(\frac{\psi_{n,J}(r)}{r}\right)\right) \\ &+ \left(\frac{J(J+1)\hbar^2}{2\mu r^2} + V(r) + \epsilon_n\right)\psi_{n,J}(r) \\ &+ \sum_{n'} V_{nn'}(r)\psi_{n',J}(r).\end{aligned} \tag{B.4}$$

Now consider

$$\begin{aligned}\frac{1}{r}\frac{\partial}{\partial r}\left(r^2\frac{\partial}{\partial r}\left(\frac{\psi_{n,J}(r)}{r}\right)\right) &= \frac{1}{r}\frac{\partial}{\partial r}\left(r\frac{\partial}{\partial r}\left(\psi_{n,J}(r)\right) - \psi_{n,J}(r)\right) \\ &= \frac{r}{r}\frac{\partial^2}{\partial r^2}\left(\psi_{n,J}(r)\right) = \frac{\partial^2}{\partial r^2}\left(\psi_{n,J}(r)\right).\end{aligned} \tag{B.5}$$

Substituting equation (B.5) into (B.4) yields the result

$$\begin{aligned}E_\Psi \psi_{n,J}(r) = & \frac{-\hbar^2}{2\mu}\frac{\partial^2}{\partial r^2}\left(\psi_{n,J}(r)\right) \\ &+ \left(\frac{J(J+1)\hbar^2}{2\mu r^2} + V(r) + \epsilon_n\right)\psi_{n,J}(r) \\ &+ \sum_{n'} V_{nn'}(r)\psi_{n',J}(r) \\ &\equiv \langle r| \hat{H}_{\mathrm{CRM}} |\psi_{n,J}\rangle,\end{aligned} \tag{B.6}$$

where $\hat{H}_{\mathrm{CRM}}$ is the Hamiltonian operator for the coupled channels radial (or collective radial motion) states, given by

$$\hat{H}_{\mathrm{CRM}} = \frac{\hbar^2 \hat{k}_{\mathrm{CRM}}^2}{2\mu} + \frac{J(J+1)\hbar^2}{2\mu\hat{r}^2} + \frac{\hat{I}^2}{2\mathcal{I}} + \hat{V} + \hat{V}_{\mathrm{coup}}, \tag{B.7}$$

where $\hat{k}_{\mathrm{CRM}} = \mathrm{i}\frac{\partial}{\partial r}$.

Appendix C

Fourier grid method

This appendix details the Fourier grid method, which is used to numerically compute the action of the Hamiltonian $\hat{H}_{\mathrm{CRM}}$ on a numerical state. This involves splitting the Hamiltonian into two parts. Consider the Hamiltonian in equation (2.8). We can express this Hamiltonian as

$$\hat{H}_{\mathrm{CRM}} = \hat{H}_{\mathrm{CRM0}} + \mathrm{i}\hat{W}, \tag{C.1}$$

where

$$\hat{H}_{\mathrm{CRM0}} = \hat{K}_{\mathrm{CRM}} + \hat{V}_{\mathrm{CRM0}}, \tag{C.2}$$

and

$$\hat{K}_{\mathrm{CRM}} = \frac{\hbar^2 \hat{k}^2_{\mathrm{CRM}}}{2\mu}, \tag{C.3}$$

where $\hat{k}_{\mathrm{CRM}} = \mathrm{i}\frac{\partial}{\partial r}$ and $\hat{V}_{\mathrm{CRM0}}$ are the remaining real potentials. This is a useful splitting of $\hat{H}_{\mathrm{CRM0}}$ because all the potentials in $\hat{V}_{\mathrm{CRM0}}$ are diagonal in radial position (i.e.: $\left\langle r^{'}, I_n \right| \hat{V}_{\mathrm{CRM0}} \left| r, I_n \right\rangle = V_{\mathrm{CRM0}}(r, n)$ if $r = r^{'}$ and zero otherwise), where-as the kinetic operator $\hat{K}_{\mathrm{CRM}}$ is not.

Suppose we know the wave-function of the collective radial motion at time t, and we would like to find the wave-function at time $t + \Delta t$. Using the results derived in appendix A.4, we can express the time propagated wave-function as

$$\langle r|\psi_{n,J}(t+\Delta t)\rangle = \exp\left(\frac{-iH_+\Delta t}{\hbar}\right)\sum_{m=0}^{\infty}(2-\delta_{m0})i^m J_m(\frac{H_-\Delta t}{\hbar})\,\langle r|\,Q_m(\hat{H}_{\rm norm})\,|\psi_{n,J}(t)\rangle\,, \tag{C.4}$$

where

$$\hat{H}_{\rm norm} = \frac{H_+\hat{I} - \hat{H}_{\rm CRM0}}{H_-}. \tag{C.5}$$

We must find the matrix elements $\langle r|\,Q_m(\hat{H}_{\rm norm})\,|\psi_{n,J}(t)\rangle$ for every m in the Chebyshev summation in equation (C.4). Using the modified Chebyshev recurrence relation in equation (A.29), these elements can be expressed as

$$\begin{aligned}\langle r|\,Q_m(\hat{H}_{\rm norm})\,|\psi_{n,J}(t)\rangle = {\rm e}^{-\gamma(r)}(2\,\langle r|\,\hat{H}_{\rm norm}Q_{m-1}(\hat{H}_{\rm norm})\,|\psi_{n,J}(t)\rangle \\ -\,{\rm e}^{-\gamma(r)}\,\langle r|\,Q_{m-2}\,|\psi_{n,J}(t)\rangle),\end{aligned} \tag{C.6}$$

where we have used the fact that the operators $\hat{\gamma}$ in equation (A.29) are diagonalised in the radial coordinate. The states $Q_{m-2}\,|\psi_{n,J}(t)\rangle$ and $Q_{m-1}\,|\psi_{n,J}(t)\rangle$ are known prior to the calculation of $\langle r|\,Q_m(\hat{H}_{\rm norm})\,|\psi_{n,J}(t)\rangle$, and thus the only involved calculation is that of $\langle r|\,\hat{H}_{\rm norm}Q_{m-1}(\hat{H}_{\rm norm})\,|\psi_{n,J}(t)\rangle$. Ultimately, from equation (C.5), we need to calculate matrix elements

$$\begin{aligned}\langle r|\,\hat{H}_{\rm CRM0}Q_{m-1}(\hat{H}_{\rm norm})\,|\psi_{n,J}(t)\rangle = \langle r|\,\hat{K}_{\rm CRM}Q_{m-1}(\hat{H}_{\rm norm})\,|\psi_{n,J}(t)\rangle \\ +\,\langle r|\,\hat{V}_{\rm CRM0}Q_{m-1}(\hat{H}_{\rm norm})\,|\psi_{n,J}(t)\rangle\,.\end{aligned} \tag{C.7}$$

For brevity, we will refer to the state $Q_{m-1}(\hat{H}_{\rm norm})\,|\psi_{n,J}(t)\rangle$ as $\left|\psi^{m-1}_{n,J}(t)\right\rangle$. The potential matrix elements are relatively trivial to calculate, and have the form

$$\begin{aligned}\langle r|\,\hat{V}_{\rm CRM0}\left|\psi^{m-1}_{n,J}(t)\right\rangle &= \langle r|\left(\frac{J(J+1)\hbar^2}{2\mu\hat{r}^2}+\frac{\hat{I}^2}{2\mathcal{I}}+\hat{U}\right)\left|\psi^{m-1}_{n,J}(t)\right\rangle \\ &+\sum_{n'}\langle r,I_n|\,\hat{V}_{\rm coup}\,|r,I_{n'}\rangle\left\langle r\middle|\psi^{m-1}_{n',J}(t)\right\rangle \\ &=\left(\frac{J(J+1)\hbar^2}{2\mu r^2}+\epsilon_n+U(r)\right)\psi^{m-1}_{n,J}(r,t) \\ &+\sum_{n'}V_{nn'}(r)\psi^{m-1}_{n',J}(r,t),\end{aligned} \tag{C.8}$$

where $\hat{V}_{\text{CRM0}} = \frac{J(J+1)\hbar^2}{2\mu\hat{r}^2} + \frac{\hat{l}^2}{2\mathcal{I}} + \hat{U} + \hat{V}_{\text{coup}}$ from equation (2.8). The kinetic matrix elements are more involved.

C.1 Kinetic matrix elements

In order to calculate the action of the kinetic operator, we need to transform into momentum space. The eigenstates of this momentum operator are the same as the eigenstates of the free-particle Hamiltonian, which have the relation

$$\langle r|k\rangle = \frac{1}{\sqrt{2\pi}} \exp(\mathrm{i}kr), \tag{C.9}$$

Performing a spectral decomposition of $\hat{K}_{\text{CRM}}$ on the kinetic matrix element yields

$$\begin{aligned} \langle r|\, \hat{K}_{\text{CRM}} \left|\psi_{n,J}^{m-1}(t)\right\rangle &= \int_{-\infty}^{\infty} \mathrm{d}k\, \langle r|\, \hat{K}_{\text{CRM}}\, |k\rangle \left\langle k\middle|\psi_{n,J}^{m-1}(t)\right\rangle \\ &= \frac{\hbar^2}{2\mu} \int_{-\infty}^{\infty} \mathrm{d}k\; k^2\, \langle r|k\rangle \left\langle k\middle|\psi_{n,J}^{m-1}(t)\right\rangle . \end{aligned} \tag{C.10}$$

Equation (C.10) requires us to know the momentum wave-functions $\left\langle k\middle|\psi_{n,J}^{m-1}(t)\right\rangle$, which can be found using a radial identity operator

$$\left\langle k\middle|\psi_{n,J}^{m-1}(t)\right\rangle = \int_0^{\infty} \mathrm{d}r'\;\; \langle k|r'\rangle\; \langle r'|\psi_{n,J}^{m-1}(t)\rangle\, . \tag{C.11}$$

Using equation (C.9), we can express equation (C.11) as

$$\left\langle k\middle|\psi_{n,J}^{m-1}(t)\right\rangle = \frac{1}{\sqrt{2\pi}} \int_0^{\infty} \mathrm{d}r'\;\; \exp(-\mathrm{i}kr')\, \langle r'|\psi_{n,J}^{m-1}(t)\rangle\, , \tag{C.12}$$

which is known as a forward Fourier transform. Performing a similar substitution into equation (C.10) we find

$$\begin{aligned} \langle r, I_n|\, \hat{K}_{\text{CRM}} \left|\psi_{J}^{m-1}(t)\right\rangle &= \frac{\hbar^2}{2\sqrt{2\pi}\mu} \int_{-\infty}^{\infty} \mathrm{d}k\; k^2 \exp(\mathrm{i}kr) \left\langle k\middle|\psi_{n,J}^{m-1}(t)\right\rangle \\ &= \frac{\hbar^2}{4\pi\mu} \int_{-\infty}^{\infty} \mathrm{d}k\;\; \int_0^{\infty} \mathrm{d}r'\;\; k^2 \exp(\mathrm{i}kr) \exp(-\mathrm{i}kr')\, \langle r'|\psi_{n,J}^{m-1}(t)\rangle\, , \end{aligned} \tag{C.13}$$

which is known as a backwards Fourier transform. Collectively, equations (C.12) and (C.13) outline a simple procedure in order to calculate the matrix elements $\langle r, I_n | \hat{K}_{\mathrm{CRM}} | \psi_J^{m-1}(t) \rangle$ from the wave-function $\langle r | \psi_{n,J}^{m-1}(t) \rangle$. Firstly, generate the momentum wave-function $\langle k | \psi_{n,J}^{m-1}(t) \rangle$ by performing a forward Fourier transform from radial to momentum space. Then, multiply each element of $\langle k | \psi_{n,J}^{m-1}(t) \rangle$ by k^2, and perform a backwards Fourier transform back into radial space.

C.2 Discrete Fourier transform

A powerful method to treat these Fourier transforms is to discretise the radial and momentum spaces, so one can employ discrete Fourier transform methods. The physical consequences of this is that now instead of the state $|\psi_{n,J}^{m-1}(t)\rangle$ being able to occupy all momentum states k for $k \in [-\infty, \infty]$, it can only occupy states up to a finite limit. As a consequence of this momentum cut-off, state $|\psi_{n,J}^{m-1}(t)\rangle$ cannot occupy radial states above a maximum radius r_{max}, and below a minimum radius r_{min}. This constriction of radius and momentum presents no problem for our method, since the wave-packets can be both localised in radial and momentum space specifically so that these conditions are met.

C.2.1 The Fourier grid method

The Fourier grid method consists of representing the radial and momentum coordinates as grids of equidistant points [76]. Consider a discrete radial grid of points separated equidistantly from one another, with the first point at $r = r_{\mathrm{min}}$ and the last at $r = r_{\mathrm{max}}$. The separation between adjacent points is given by

$$\Delta r = \frac{r_{\mathrm{max}} - r_{\mathrm{min}}}{N}, \tag{C.14}$$

where N is known as the number of sampling points, which is equal to the number of collocation points minus one [77]. The collocation points are another name for the physical points in the grid. For example, if one physically draws 9 dots equally spaced apart for their grid, the number of collocation points is equal to 9, and the number of sampling points is equal to 8. Using our grid, we define the sampling points r_j as

$$r_j = r_{\mathrm{min}} + j\Delta r, \tag{C.15}$$

where $j \in [0 \,..\, N-1]$. For a discrete radial grid, the momentum space of the grid is also a set of equidistant points [73, 76, 77]. These momentum grid points have the form [77]

$$k_l = l\Delta k, \tag{C.16}$$

where Δk is the momentum separation and $l \in [-(N/2-1) \,..\, N/2]$. The two separations Δr and Δk have a relation [73]

$$\Delta k \Delta r = \frac{2\pi}{N}. \tag{C.17}$$

With this discretisation in mind, equation (C.13) now becomes

$$\begin{aligned}\langle r_j, I_n | \hat{K}_{\mathrm{CRM}} \left|\psi_J^{m-1}(t)\right\rangle &= \frac{\hbar^2 \Delta k \Delta r}{4\pi\mu} \sum_{l=-(N/2-1)}^{N/2} \sum_{j'=0}^{N-1} k_l^2 \exp(\mathrm{i}k_l r_j) \exp\big(-\mathrm{i}k_l r_{j'}\big) \langle r_{j'} | \psi_{n,J}^{m-1}(t)\rangle \\ &= \frac{\hbar^2}{2\mu N} \sum_{l=-(N/2-1)}^{N/2} \sum_{j=0}^{N-1} k_l^2 \exp(\mathrm{i}k_l r_j) \exp\big(-\mathrm{i}k_l r_{j'}\big) \langle r_{j'} | \psi_{n,J}^{m-1}(t)\rangle \,.\end{aligned} \tag{C.18}$$

Here we have substituted in equation (C.17) in order to simplify the pre-factor. Now consider

$$\begin{aligned}\exp(\mathrm{i}k_l r_j) \exp\big(-\mathrm{i}k_l r_{j'}\big) &= \exp\big(\mathrm{i}k_l (r_j - r_{j'})\big) \\ &= \exp\Big(\mathrm{i}k_l \Delta r (j - j^{'})\Big) \\ &= \exp(\mathrm{i}k_l \Delta r j) \exp\Big(-\mathrm{i}k_l \Delta r j^{'}\Big) \\ &= \exp(\mathrm{i}\Delta k \Delta r j l) \exp\Big(-\mathrm{i}\Delta k \Delta r j^{'} l\Big).\end{aligned} \tag{C.19}$$

Substituting equation (C.17) into the rhs of equation (C.19) yields

$$\exp(\mathrm{i}\Delta k \Delta r j l) \exp\Big(-\mathrm{i}\Delta k \Delta r j^{'} l\Big) = \exp\left(\mathrm{i}\frac{2\pi}{N} j l\right) \exp\left(-\mathrm{i}\frac{2\pi}{N} j^{'} l\right), \tag{C.20}$$

which is the form of the exponentials needed to perform discrete Fourier transforms. Finally, we have the discrete kinetic matrix elements of equation (C.18)

$$\langle r_j, I_n | \hat{K}_{\mathrm{CRM}} \left|\psi_J^{m-1}(t)\right\rangle = \frac{\hbar^2}{2\mu N} \sum_{l=-(N/2-1)}^{N/2} \sum_{j=0}^{N-1} k_l^2 \exp\left(\mathrm{i}\frac{2\pi j l}{N}\right) \exp\left(-\mathrm{i}\frac{2\pi j^{'} l}{N}\right) \langle r_{j'} | \psi_{n,J}^{m-1}(t)\rangle \,. \tag{C.21}$$

In our codes, these discrete Fourier transforms are provided by the FFTW library, which features fast calculation times and accurate results.

Bibliography

[1] S. Hofmann, "Eighty years of research on super-heavy nuclei," *EPJ Web of Conferences*, vol. 182, p. 02054, 2018.

[2] A. Sobiczewski, F. Gareev, and B. Kalinkin, "Closed shells for Z $>$ 82 and N $>$ 126 in a diffuse potential well," *Physics Letters*, vol. 22, p. 500, 1966.

[3] W. Greiner and J. A. Maruhn, *Nuclear Models*. Springer-Verlag Berlin Heidelberg, Germany, 1997.

[4] G. R. Satchler, *Introduction to Nuclear Reactions*. Palgrave Macmillan, United Kingdom, 1990.

[5] G. Adamian, N. Antonenko, A. Diaz-Torres, and S. Heinz, "How to extend the chart of nuclides?," *European Physical Journal A*, vol. 56, pp. 47–1, 2020.

[6] S. A. Giuliani, Z. Matheson, W. Nazarewicz, E. Olsen, P.-G. Reinhard, J. Sadhukhan, B. Schuetrumpf, N. Schunck, and P. Schwerdtfeger, "Colloquium: Superheavy elements: Oganesson and beyond," *Rev. Mod. Phys.*, vol. 91, p. 011001, 2019.

[7] E. B. Norman and D. N. Schramm, "On the Conditions Required for the r-PROCESS," , vol. 228, p. 881, 1979.

[8] "It's official! Element 113 was discovered at RIKEN." Online: available at https://www.riken.jp/en/news_pubs/research_news/pr/2015/20151231_1/ (accessed 22/10/2020).

[9] "Schedule of RIBF operation." Online: available at https://www.nishina.riken.jp/rarfmt/pc.html (accessed 22/10/2020).

[10] "Flerov laboratory of nuclear reactions." Online: available at http://flerovlab.jinr.ru/she-factory/ (accessed 22/10/2020).

[11] V. I. Zagrebaev, Y. Aritomo, M. G. Itkis, Y. T. Oganessian, and M. Ohta, "Synthesis of superheavy nuclei: How accurately can we describe it and calculate the cross sections?," *Phys. Rev. C*, vol. 65, p. 014607, 2001.

[12] P. Fröbrich and R. Lipperheide, *Theory of Nuclear Reactions*. Clarendon Press, United Kingdom, 1996.

[13] H. Feshbach, *Theoretical nuclear physics: Nuclear reactions*. Wiley, United States, 1992.

[14] J. R. Birkelund and J. R. Huizenga, "Fusion reactions between heavy nuclei," *Annual Review of Nuclear and Particle Science*, vol. 33, p. 265, 1983.

[15] M. Morjean, D. Jacquet, M. Laget, and J. F. Berger, "Discrimination between fission and quasi-fission from reaction time measurements," *Journal of Physics: Conference Series*, vol. 282, p. 012009, 2011.

[16] G. G. Adamian, N. Antonenko, S. Ivanova, V. Volkov, A. Diaz-Torres, and W. Scheid, "Ways for fusion of heavy nuclei," in *International Symposium Advances in Nuclear Physics*, p. 65, Eds. D.N. Poenaru and S. Stoica, World Scientific, Singapore, 2000.

[17] A. Diaz-Torres, G. G. Adamian, N. V. Antonenko, and W. Scheid, "Melting or nucleon transfer in fusion of heavy nuclei?," *Physics Letters B*, vol. 481, p. 228, 2000.

[18] A. Diaz-Torres, "Competition between fusion and quasi-fission in a heavy fusing system within a quantum-statistical theory," 2006. Online: available at http://www.lnl.infn.it/∼fusion06/talks/Tuesday/diaz-torres.pdf (accessed 29/08/2018).

[19] W. J. Świątecki, "The Dynamics of Nuclear Coalescence or Reseparation," *Physica Scripta*, vol. 24, p. 113, 1981.

[20] W. J. Świątecki, K. Siwek-Wilczyńska, and J. Wilczyński, "Fusion by diffusion. II. Synthesis of transfermium elements in cold fusion reactions," *Phys. Rev. C*, vol. 71, p. 014602, 2005.

[21] Y. Abe, Y. Aritomo, T. Wada, and M. Ohta, "A new mechanism for synthesis of superheavy elements," *Journal of Physics G: Nuclear and Particle Physics*, vol. 23, p. 1275, 1997.

[22] Denisov, V. Yu., and S. Hofmann, "Formation of superheavy elements in cold fusion reactions," *Phys. Rev. C*, vol. 61, p. 034606, 2000.

[23] V. I. Zagrebaev, "Synthesis of superheavy nuclei: Nucleon collectivization as a mechanism for compound nucleus formation," *Phys. Rev. C*, vol. 64, p. 034606, 2001.

[24] R. W. Hasse, "Approaches to nuclear friction," *Reports on Progress in Physics*, vol. 41, p. 1027, 1978.

[25] Y. Abe, C. Shen, D. Boilley, and B. G. Giraud, "Compound nucleus reaction theory for synthesis of super-heavy elements," *EPJ Web of Conferences*, vol. 2, p. 10002, 2010.

[26] P. Fröbrich and I. Gontchar, "Langevin description of fusion, deep-inelastic collisions and heavy-ion-induced fission," *Physics Reports*, vol. 292, p. 131, 1998.

[27] A. Fukushima, A. Nasirov, Y. Aritomo, T. Wada, and M. Ohta, "A reassessment of surface friction model for maximum cold fusion reactions in superheavy mass region," *AIP Conference Proceedings*, vol. 891, p. 443, 2007.

[28] Y. Abe, A. Marchix, C. Shen, B. Yilmaz, G. Kosenko, D. Boilley, and B. G. Giraud, "Dynamics of massive systems and synthesis of superheavy elements," *International Journal of Modern Physics E*, vol. 16, 2007.

[29] Y. Aritomo, "Fusion-fission process of superheavy elements with fluctuation-dissipation model," *Progress of Theoretical Physics Supplement*, vol. 146, p. 503, 2002.

[30] K. Hagino and N. Takigawa, "Subbarrier Fusion Reactions and Many-Particle Quantum Tunneling," *Progress of Theoretical Physics*, vol. 128, p. 1061, 2012.

[31] B. B. Back, H. Esbensen, C. L. Jiang, and K. E. Rehm, "Recent developments in heavy-ion fusion reactions," *Rev. Mod. Phys.*, vol. 86, p. 317, 2014.

[32] K. Hagino, N. Rowley, and A. T. Kruppa, "A program for coupled-channel calculations with all order couplings for heavy-ion fusion reactions," *Computer Physics Communications*, vol. 123, p. 143, 1999.

[33] P. Stevenson and M. Barton, "Low-energy heavy-ion reactions and the Skyrme effective interaction," *Progress in Particle and Nuclear Physics*, vol. 104, p. 142, 2019.

[34] C. Simenel and A. Umar, "Heavy-ion collisions and fission dynamics with the time-dependent Hartree–Fock theory and its extensions," *Progress in Particle and Nuclear Physics*, vol. 103, p. 19, 2018.

[35] A. Szabo and N. Ostlund, *Modern Quantum Chemistry: Introduction to Advanced Electronic Structure Theory*. Dover Publications, United States, 1996.

[36] M. Genkin and W. Scheid, "A two-dimensional inverse parabolic potential within the Lindblad theory for application in nuclear reactions," *Journal of Physics G: Nuclear and Particle Physics*, vol. 34, p. 441, 2007.

[37] A. Diaz-Torres, D. J. Hinde, M. Dasgupta, G. J. Milburn, and J. A. Tostevin, "Dissipative quantum dynamics in low-energy collisions of complex nuclei," *Phys. Rev. C*, vol. 78, p. 064604, 2008.

[38] A. Diaz-Torres, "Coupled-channels density-matrix approach to low-energy nuclear collision dynamics: A technique for quantifying quantum decoherence effects on reaction observables," *Phys. Rev. C*, vol. 82, p. 054617, 2010.

[39] H. Breuer and F. Petruccione, *The Theory of Open Quantum Systems*. Oxford University Press, United Kingdom, 2002.

[40] M. Tokieda and K. Hagino, "Quantum tunneling with friction," *Physical Review C*, vol. 95, p. 054604, 2017.

[41] M. Tokieda and K. Hagino, "Quantum surface friction model for fusion reactions around the coulomb barrier," *Proceedings of 13th International Conference on Nucleus-Nucleus Collisions*, vol. 32, p. 010008, 2020.

[42] M. Tokieda and K. Hagino, "Time-dependent approaches to open quantum systems," *Frontiers in Physics*, vol. 8, p. 8, 2020.

[43] M. Formanek, M. Váňa, and K. Houfek, "Comparison of the Chebyshev Method and the Generalized Crank-Nicholson Method for time Propagation in Quantum Mechanics," *AIP Conference Proceedings*, vol. 1281, 2010.

[44] "Extreme light infrastructure - nuclear physics." Online: available at https://eli-laser.eu/ (accessed: 29/04/2020).

[45] M. Ismail, W. Seif, and H. El-Gebaly, "On the Coulomb interaction between spherical and deformed nuclei," *Physics Letters B*, vol. 563, p. 53, 2003.

[46] A. Diaz-Torres and M. Wiescher, "Characterizing the astrophysical S-factor for 12C + 12C with wave-packet dynamics," *Phys. Rev. C*, vol. 95, p. 055802, 2018.

[47] Y. Eisen and Z. Vager, "The incoming wave boundary condition for elastic scattering of heavy particles at incident energies near the Coulomb barrier," *Nuclear Physics A*, vol. 187, p. 219, 1972.

[48] R. T. Pack, "Space-fixed vs body-fixed axes in atom-diatomic molecule scattering. sudden approximations," *The Journal of Chemical Physics*, vol. 60, p. 633, 1974.

[49] K. Schafer, "The energy analysis of time-dependent numerical wave functions," *Computer Physics Communications*, vol. 63, p. 427, 1991.

[50] K. J. Schafer and K. C. Kulander, "Energy analysis of time-dependent wave functions: Application to above-threshold ionization," *Phys. Rev. A*, vol. 42, p. 5794, 1990.

[51] M. Boselli and A. Diaz-Torres, "Quantifying low-energy fusion dynamics of weakly bound nuclei from a time-dependent quantum perspective," *Phys. Rev. C*, vol. 92, p. 044610, 2015.

[52] D. T. Colbert and W. H. Miller, "A novel discrete variable representation for quantum mechanical reactive scattering via the S-matrix Kohn method," *The Journal of Chemical Physics*, vol. 96, p. 1982, 1992.

[53] T. Vockerodt and A. Diaz-Torres, "Describing heavy-ion fusion with quantum coupled-channels wave-packet dynamics," *Phys. Rev. C*, vol. 100, p. 034606, 2019.

[54] A. Diaz-Torres, G. G. Adamian, V. V. Sargsyan, and N.V.Antonenko, "Energy-shifting formulae yield reliable reaction and capture probabilities," *Physics Letters B*, vol. 739, p. 348, 2014.

[55] M. Thomson, *Modern Particle Physics*. Cambridge University Press, United Kingdom, 2013.

[56] Y. Sun, R. S. Judson, and D. J. Kouri, "Body frame close coupling wave packet approach to gas phase atom–rigid rotor inelastic collisions," *The Journal of Chemical Physics*, vol. 90, p. 241, 1989.

[57] J. Dai and J. Z. H. Zhang, "Time-dependent wave packet approach to state-to-state reactive scattering and application to H + O_2 reaction," *The Journal of Physical Chemistry*, vol. 100, p. 6898, 1996.

[58] D. J. Tannor and D. E. Weeks, "Wave packet correlation function formulation of scattering theory: The quantum analog of classical s-matrix theory," *The Journal of Chemical Physics*, vol. 98, pp. 3884–3893, 1993.

[59] I. J. Thompson, "Coupled reaction channels calculations in nuclear physics," *Computer Physics Reports*, vol. 7, p. 167, 1988.

[60] H. M. Jia, C. J. Lin, H. Q. Zhang, F. Yang, Z. H. Liu, F. Jia, X. X. Xua, S. T. Zhang, and K. Hagino, "Systematic study of the surface diffuseness of nuclear potential with high precision large-angle quasi-elastic scattering," *Nuclear Physics A*, vol. 834, p. 189c, 2010.

[61] H. Zhang, C. J. Lin, H. M. Jia, L. Yang, X. X. Xu, F. Yang, Z. D. Wu, Z. H. Liu, N. R. Ma, L. J. Sun, and D. X. Wang, "Sub-barrier backward quasielastic scattering: A probe of the hexadecapole deformation," *EPJ Web of Conferences*, vol. 117, p. 04010, 2016.

[62] S. Raman, J. C. W. Nestor, and P. Tikkanen, "Transition probability from the ground to the first-excited 2+ state of even–even nuclides," *Atomic Data and Nuclear Data Tables*, vol. 78, p. 1, 2001.

[63] P. Talon, N. Alamanos, M. Lamehi-Rachti, C. Levi, and L. Papineau, "Coulomb and nuclear excitation effects on 16O scattering from samarium isotopes," *Nuclear Physics A*, vol. 359, p. 493, 1981.

[64] T. Izumoto, T. Udagawa, and B. T. Kim, "Coupled-channels analyses of scattering and fusion cross sections of ^{16}O + ^{152,154}Sm, ^{186}W systems at sub- and near-coulomb barrier energies," *Phys. Rev. C*, vol. 51, p. 761, 1995.

[65] I. Nunes and H. S. da Silva, *Artificial Neural Networks: A Practical Course*. Springer, Switzerland, 2018.

[66] J. Gomez-Camacho and R. C. Johnson, "Tidal symmetry in nuclear reactions: application to the scattering of polarised projectiles," *Journal of Physics G: Nuclear Physics*, vol. 12, p. 609, 1986.

[67] H. J. Fink, J. Maruhn, W. Scheid, and W. Greiner, "Theory of fragmentation dynamics in nucleus-nucleus collisions," *Zeitschrift für Physik*, vol. 268, p. 321, 1974.

[68] A. Diaz-Torres and W. Scheid, "Two center shell model with Woods–Saxon potentials: Adiabatic and diabatic states in fusion," *Nuclear Physics A*, vol. 757, p. 373, 2005.

[69] A. Diaz-Torres, "OWL: A code for the two-center shell model with spherical Woods-Saxon potentials," *Computer Physics Communications*, vol. 224, p. 381, 2018.

[70] G. Katz, D. Gelman, M. A. Ratner, and R. Kosloff, "Stochastic surrogate hamiltonian," *The Journal of chemical physics*, vol. 129, p. 034108, 2008.

[71] N. Renaud, M. A. Ratner, and V. Mujica, "A stochastic surrogate Hamiltonian approach of coherent and incoherent exciton transport in the Fenna-Matthews-Olson complex," *The Journal of Chemical Physics*, vol. 135, p. 075102, 2011.

[72] "Lesson 10: Chebyshev series." Online: available at http://www.maths.usyd.edu.au/u/olver/teaching/NCA/10.pdf (accessed 09/12/2018).

[73] D. J. Tannor, *Introduction to Quantum Mechanics: A Time-Dependent Perspective*. University Science Books, United States, 2007.

[74] H. Tal-Ezer and R. Kosloff, "An accurate and efficient scheme for propagating the time dependent Schrödinger equation," *The Journal of Chemical Physics*, vol. 81, p. 3967, 1984.

[75] V. A. Mandelshtam and H. S. Taylor, "A simple recursion polynomial expansion of the Green's function with absorbing boundary conditions. Application to the reactive scattering," *The Journal of Chemical Physics*, vol. 103, p. 2903, 1995.

[76] R. Kosloff, *The Fourier Method*, p. 175. Springer, Netherlands, 1993.

[77] M. Berman and R. Kosloff, "Time-dependent solution of the liouville-von neumann equation: non-dissipative evolution," *Computer Physics Communications*, vol. 63, p. 1, 1991.